



저작자표시-비영리-변경금지 2.0 대한민국

이용자는 아래의 조건을 따르는 경우에 한하여 자유롭게

- 이 저작물을 복제, 배포, 전송, 전시, 공연 및 방송할 수 있습니다.

다음과 같은 조건을 따라야 합니다:



저작자표시. 귀하는 원저작자를 표시하여야 합니다.



비영리. 귀하는 이 저작물을 영리 목적으로 이용할 수 없습니다.



변경금지. 귀하는 이 저작물을 개작, 변형 또는 가공할 수 없습니다.

- 귀하는, 이 저작물의 재이용이나 배포의 경우, 이 저작물에 적용된 이용허락조건을 명확하게 나타내어야 합니다.
- 저작권자로부터 별도의 허가를 받으면 이러한 조건들은 적용되지 않습니다.

저작권법에 따른 이용자의 권리는 위의 내용에 의하여 영향을 받지 않습니다.

이것은 [이용허락규약\(Legal Code\)](#)을 이해하기 쉽게 요약한 것입니다.

[Disclaimer](#)

Doctoral Thesis

Design of Electrode Architecture for Deformable
Energy Storage Devices

Woo-Jin Song

Department of Energy Engineering
(Energy Engineering)

Graduate School of UNIST

2018

Design of Electrode Architecture for Deformable Energy Storage Devices

Woo-Jin Song

Department of Energy Engineering
(Energy Engineering)

Graduate School of UNIST

Design of Electrode Architecture for Deformable Energy Storage Devices

A thesis/dissertation
submitted to the Graduate School of UNIST
in partial fulfillment of the
requirements for the degree of
Doctor of Philosophy

Woo-Jin Song

06/12/2018

Approved by



Advisor

Soojin Park

Design of Electrode Architecture for Deformable Energy Storage Devices

Woo-Jin Song

This certifies that the thesis/dissertation of Woo-Jin Song is
approved.

06/12/2018

Signature



Advisor: Soojin Park

signature



Prof. SangYoung Lee

signature



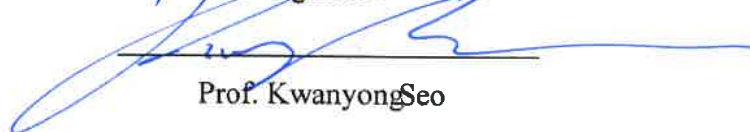
Prof. Hyun-Kon Song

signature



Prof. Unyong Jeong

signature



Prof. Kwanyong Seo

Abstract

With the emergence of deformable electronics, there is growing interest in wearable devices such as implantable medical devices, healthcare devices, artificial skins, and robotics with arbitrarily shaped surfaces. While there has been tremendous progress in the development of wearable devices, the research on deformable energy-storage devices that are able to maintain a large physical strain without sacrificing battery performance is still in an infant state. Thus, to fulfill the demand for reliable wearable devices, a key challenge is the development in shape of deformable energy-storage devices, which can foldable and crumple and even stretchable for supplying power to them. A formidable hurdle to the development of deformable energy devices is how to develop a deformable electrode owing to a trade-off relationship between mechanical deformability and electrical conductivity under a physical deformation.

In this thesis, we propose the design of deformable electrode architecture and demonstrate their mechanical robustness and electrical properties at large deformation. In addition, we examine *in-situ* small-angle X-ray scattering measurement to substantiate the percolation behaviors of conductive fillers in an elastomer. Using the proposed deformable electrode, we fabricate various deformable energy devices such as foldable lithium-ion batteries (LIBs), stretchable aqueous rechargeable lithium-ion batteries (ARLBs), and stretchable rechargeable zinc-silver batteries.

In chapter I, we briefly introduce research background of stretchable electronics and wearable devices. Furthermore, we discuss various fabrication methods of the deformable electrode and its application to stretchable energy devices.

In chapter II, we propose the fabrication of crumple and super-flexible electrode based on the nanowire-wound micro-fiber substrate which consists of conductive nanowires as a binder and conducting agents, porous nonwoven substrate, and active materials. The proposed electrode design can be effectively utilized for superior mechanical durability (1000 folding cycles) with a high areal energy density through stacking electrode. Based on the electrodes, we demonstrate a highly flexible LIBs with a high energy density which can be repeatedly crumpled, folded, and even hammered without structural failure and performance loss.

In chapter III, we present a bio-inspired Jaboticaba-like multidimensional conductive fillers/elastomer composite as a stretchable electrode for stretchable batteries. *In-situ* small-angle X-ray scattering is a powerful tool for monitoring the structural evolution of nanofillers in a polymer matrix. As a result, multidimensional carbon fillers in polymer matrix retain the excellent percolation network under high strain, based on the analysis of Herman's orientation parameter and 2D Porod length calculation. Using the polymer composite, we fabricate, for the first time,

stretchable ARLBs as a stretchable power source for wearable devices. Our stretchable batteries show outstanding rate performance and exceptional cycle retention. Furthermore, the batteries can deliver constant power to a device at 100% strain.

In chapter IV, we propose stretchable zinc-silver rechargeable batteries based on a Janus-faced electrode, comprising of a cathode and an anode on one electrode, are presented. In the Janus-faced electrode based on Ag/poly(styrene-*b*-butadiene-*b*-styrene) (SBS) polymer nanocomposite, a metallic zinc serves anode materials while silver nanoparticles exhibit bifunctional roles as cathode materials and conducting fillers as a current collector. Furthermore, the proposed stretchable energy device can tolerate a large strain and can deliver a stable electrochemical performance even under 200% strain while keeping its functional performance.

In chapter V, we report a gradient assembled polyurethane (GAP)-based stretchable conductor with fine controlled internal architecture assembled with gold nanoparticles (Au NPs) as a conductive filler in order to develop a universally applicable method for fabricating the geometrically designed nanocomposite conductor. In the present study, we demonstrate a novel assembly protocol, composite-by-composite (CbC) assembly, which integrates the advantages of both conventional vacuum-assisted filtration and layer-by-layer (LbL) assembly. Conversely, LbL assembly can manufacture with highly ordered architectures, allowing the fine nanoscale control over the thickness and composition of hybrid multi-components through the sequential assembly. Most uniquely, this GAP stretchable multilayer conductor demonstrates not only top-surface conductive structure with superior mechanical stretchability even above 300% strain. Using the GAP stretchable conductor, we demonstrate the highly stretchable energy storage device such as lithium-ion battery retaining stable electrochemical performance under strain.

Blank page

Contents

I. INTRODUCTION	1
1.1 BACKGROUND	1
1.2 DEFORMABLE BATTERIES	5
1.3 DEFORMABLE ELECTRODES.....	8
1.3 REFERENCE.....	10
II. FOLDABLE ELECTRODE ARCHITECTURES BASED ON SILVER-NANOWIRE- WOUND OR CARBON-NANOTUBE-WEBBED MICROMETER-SCALE FIBERS OF POLYETHYLENE TEREPHTHALATE MATS FOR FLEXIBLE LITHIUM ION BATTERIES	13
2.1 INTRODUCTION	13
2.2 EXPERIMENTAL.....	15
2.3 RESULTS AND DISCUSSION	17
2.4 CONCLUSION	27
2.5 REFERENCE.....	28
III. JABUTICABA-INSPIRED HYBRID CARBON FILLER/POLYMER ELECTRODE FOR USE IN HIGHLY STRETCHABLE AQUEOUS LI-ION BATTERIES	32
3.1 INTRODUCTION	32
3.2 EXPERIMENTAL.....	34
3.3 RESULTS AND DISCUSSION	37
3.4 CONCLUSION	49
3.5 REFERENCE.....	50
IV. DESIGN OF JANUS-FACED ELECTRODE FOR HIGHLY STRETCHABLE ZINC- SILVER RECHARGEABLE BATTERIES	53
4.1 INTRODUCTION	53
4.2 EXPERIMENTAL.....	55
4.3 RESULTS AND DISCUSSION	57
4.4 CONCLUSION	63

4.5 REFERENCE.....	64
--------------------	----

**V. GRADIENT ASSEMBLED POLYURETHANE-BASED STRETCHABLE
MULTILAYER ELECTRODE..... 66**

5.1 INTRODUCTION	66
------------------------	----

5.2 EXPERIMENTAL.....	68
-----------------------	----

5.3 RESULTS AND DISCUSSION	70
----------------------------------	----

5.4 CONCLUSION	80
----------------------	----

5.5 REFERENCE	81
---------------------	----

List of figures

[Chapter 1]

Figure 1-1. The development of stretchable electronics

Figure 1-2. Technology roadmap of wearable devices.

Figure 1-3. Various energy storage devices.

Figure 1-4. A time line of stretchable energy and conversion devices.

Figure 1-5. Various fabrication methods of stretchable electrode such as wave structure, island structure, and textile structure.

[Chapter 2]

Figure 2-1. LTO-loaded AgNW\$MF. AgNW : MF : LTO = 1 : 1.1 : 5 in weight. Loading density of LTO = 5 mg_{LTO} cm⁻². a) Fabrication. b) SEM images at three different spray times. c) Visual inspection after twisting and folding. d) Electrical conductivities of LTO-containing electrodes measured by four-point probe methods. Macroscopic thicknesses of electrodes were measured by a vernier caliper. The active layer of LTO|Al consisted of carbon black : binder : LTO = 0.5 : 0.5 : 5 in weight. The CNT#MF containing LTO consisted of CNT : MF : LTO at 1 : 1.1 : 5 in weight. Loading densities of LTO = 4.3 mg_{LTO} cm⁻² for LTO|Al and 5 mg_{LTO} cm⁻² for CNT#MF. e) Mass savings by the use of the current-collector-free and binder-free AgNW\$MF. m/m_0 = relative electrode mass with respect to conventional LTO-loaded Al (LTO|Al). Electrode mass is the sum of mass of all components of electrodes including conducting agents, binders and current collectors for LTO|Al and AgNWs and PET MF mats for AgNW\$MF as well as active materials. 2L (L = layer) and 4L AgNW\$MF's were obtained by folding unfolded AgNW\$MF (1L) in half once and twice, respectively. Scales were indicated in cm on the top.

Figure 2-2. Effects of folding deformation on the mass, microstructure, and electrical property of LTO-loaded AgNW\$MF and CNT#MF electrodes. LTO loading = 5 mg_{LTO} cm⁻² unless indicated otherwise. ~5 μm-thick LTO/AgNW (or CNT) layers were loaded above the 16 μm-thick PET MF mats within which LTO and AgNW (or CNT) were incorporated on the surface of MFs and to the inter-MF voids. a) Relative mass change of electrodes after 1000 folding cycles. b) Electrical resistance change along folding cycles. Three different LTO loadings were used for CNT#MF. R_0 and R indicate electrical resistances before and after folding, respectively. c) Positions at which the following SEM images were taken. d to f) Top-view images of LTO-loaded AgNW\$MF: d) before folding, e) after 500 folding cycles and f) after 1000 folding

cycles. g to j) Top-view images of LTO-loaded CNT#MF: g) in $5 \text{ mg}_{\text{LTO}} \text{ cm}^{-2}$ before folding, h) in $5 \text{ mg}_{\text{LTO}} \text{ cm}^{-2}$ after 250 folding cycles, i) in $1 \text{ mg}_{\text{LTO}} \text{ cm}^{-2}$ after 600 folding cycles and j) in $0.5 \text{ mg}_{\text{LTO}} \text{ cm}^{-2}$ after 1000 folding cycles.

Figure 2-3. Lithiation electrochemistry of LTO loaded on AgNW\$MF, CNT#MF and aluminum foil. Electrode compositions were indicated in Figure 1. Half cell configuration including lithium metal was used for **a** to **c** with a potential range between 1 V and 3 V. Pouch cells were designed in 5 cm x 3 cm to have energy densities at 3 mAh cm^{-2} from **d** to **f**. a) Capacity retention along repeated charges and discharges at 1C. Capacities were normalized by LTO mass in g_{LTO} (upper position) or total mass (g_{ED}) including an electrode and current collector (lower position). b) Rate capabilities. c) Differential capacities (dQ/dV) curves at 1C. d) Capacity retention of folded AgNW\$MFs (2L and 4L) versus unfolded one (1L) along repeated charges and discharges at 1C. Capacities were normalized by LTO mass in g_{LTO} or geometric electrode area (cm^2). e) Rate capabilities of folded AgNW\$MFs. f) Capacity retention of folded cells at different angles at 1C.

Figure 2-4. Crumple Superflexible batteries consisting of LTO-loaded AgNW\$MF and LFP-loaded CNT#MF (AgNW\$MF|LTO||LFP|CNT#MF). a) The superflexible battery. b) Open circuit voltages of LTO||LFP cells before and after crumpling. c) Red light emitting diodes (LEDs) powered by the NW@MF-based LTO||LFP under folding, crumpling and hammering. d) Voltage profiles of 1L- and 4L-based LTO||LFP at 1C. e) Capacity retention at 1C. The cells were folded 20 times every 20 charge/discharge cycle. f) Comparison of the 4L-NW@MF-based batteries with reported flexible batteries in terms of areal capacities and bending radii.

[Chapter 3]

Figure 3-1. Steps for the fabrication and morphological characterization of the carbon/polymer composite. a) Schematic showing the sequences in the overall fabrication process. b) SEM image showing the surface morphology of the HCP composite. The inset shows a cross-sectional SEM image. c) High-magnification SEM image of the HCP composite showing hybrid carbon in the polymer matrix. d) Variation of the surface pore size of ecoflex as a function of humidity in the breath figure method. The inset shows the relative surface area as a function of humidity. e) Photograph of a Jaboticaba tree, which has a similar shape to that of the percolating network of the hybrid carbon. TEM images of the HCP composite with different weight ratios of f) CB:CNT = 1:2 and g) CB:CNT = 1:1.

Figure 3-2. Characterization of the carbon/polymer composite. a) Photograph showing the three proposed composite films under stretching. b) Sheet resistance of the CNT/polymer, CB/polymer, and HCP composites, each of which has carbon contents of 20 wt% relative to polymer. c) Normalized sheet resistance (R/R_0) of each composite film for different amounts of strain. d) Normalized resistance of the HCP composite under strain of 100%, 150%, and 200% that were repeated for 1000 cycles. e) Fatigue test of the stretchable electrode containing the HCP composite under a strain of 200% that was repeated for 1000 cycles. The inset shows the tensile strength of the electrode as a function of the number of strain cycles, with the maximum value being 1000 cycles. f) Comparison of the normalized resistance (R/R_0) and strain performance of the HCP-containing stretchable conductor with other stretchable conductors.

Figure 3-3. Structural orientation of carbon fillers. a) 2D SAXS data of the CNT/polymer composite at 200% strain. θ is the azimuthal angle from the strain direction. b) Integrated intensity from $q = 0.00565\text{--}0.1 \text{ \AA}^{-1}$ at each azimuth angle. c) Calculated Hermans orientation factor, S .

Figure 3-4. Interconnections within the carbon framework. a) 1D SAXS data and b) those fitted with q^{-4} from $q = 0.06\text{--}0.12 \text{ \AA}^{-1}$. The overlaid plots were distinguished by multiplying the plots of CB by 10 and the plots of the HCP by 0.1. c) Plot of relative changes in the surface area per volume, as determined by the Porod analysis. d) Plot of the calculated Porod length, L_p , for anisotropic systems, as determined by the 2D Porod analysis. e) Schematic showing the comprehensive structural development of the CB/polymer, CNT/polymer, and HCP composites under strain.

Figure 3-5. Stretchable aqueous batteries in which the HCP composite was used as a current collector. Galvanostatic charge–discharge curves at various C-rates for the a) PI@AC anode (–1.0–0 V) and b) LMO@CNT cathode (0–1.2 V). c) Cycling performance of the anode and cathode at a rate of 30 C over 200 cycles. d) Schematic showing a stretchable aqueous full cell configuration. e) Rate capability of the full cell (PI@AC//LMO@CNT) for 20–60 C. The inset shows the galvanostatic charge–discharge profiles of the full cell at a rate of 20 C. f) Long-term cycle performance and coulombic efficiency of the full cell at a rate of 20 C over 500 cycles. g) The relative discharge capacity of the stretchable ARLB under various amounts of strain. h) Photograph of a LED bulb operated by the stretchable ARLB in both its unstretched state and when 100% strain is applied.

[Chapter 4]

Figure 4-1. Fabrication and characterization. a, Schematic illustration showing the fabrication process of Janus-faced electrode. b, Optical image of Janus-faced electrode. SEM images of (c) Ag/SBS composite electrodeposited with zinc (Zn, as anode) and (d) silver nanoparticles on surface of Ag/SBS composite (Ag, as cathode). e-g, EDS mapping and SEM images of cross-sectional SEM images showing Ag, C, and Zn element. f, cross-sectional SEM of Janus electrode. g, enlarged SEM view of Ag/SBS composite showing e-AgNPs and SBS polymer matrices

Figure 4-2. Characterization of electrical conductivity and mechanical properties. a, Tensile strength measurement of the Janus electrode under various strain states. (inset) tensile strength at 200% strain as a function of stretching cycles. b, Change in resistance under strain of normal electrode and the Janus electrode. c, Recorded relative resistance of the Janus electrode during 500 cycles at a strain of 100%, 150% and 200%, respectively

Figure 4-3. Measurement of in-situ SAXS and dynamic simulation. a, 2D SAXS patterns of bare SBS film and Ag/SBS composite under 200% strain. Surface AgNP of Ag/SBS composite was removed by pressing type. b, Azimuthal angle of the Ag/SBS composite at 200% strain during 100 cycles.

Figure 4-4. Electrochemical performance of stretchable zinc-silver batteries. a) schematic of configuration of stretchable zinc-silver batteries. b) voltage profile of the full batteries under various current density. c) Cycle performance of the full batteries at a 1 mA h cm^{-2} for 200 cycles. (d) Voltage profiles of the batteries under strain of 0%, 100% and 200%. (e) Cycle performance of the batteries as a function of strain.

[Chapter 5]

Figure 5-1. Schematic illustration of GAP multilayer conductors. Composite-by-composite (CbC) assembly of polyurethane (PU)-based stretchable multilayer of high and low gradient conductors with different concentration of Au NPs in stretchable layer. Photograph showing the resulting GAP multilayer conductor under 100% strain.

Figure 5-2. Architecture controlled GAP multilayer conductors. Schematic illustrations and representative cross-sectional SEM images with composed elemental mapping images of carbon and Au of a), high and b), low gradient multilayer conductors as increasing the number of layers. The scale bar in all SEM images is $20 \mu\text{m}$.

Figure 5-3. Mechanical and electrical properties of GAP multilayer conductors. a), Stress-strain curves for all GAP multilayer conductors. b), c), Young's modulus and rupture point

of low and high GAP multilayer conductors. d, Normalized resistance on top-surface of high and low GAP multilayer conductors of 3 L and 9 L under different strain conditions. e, Change of resistance on top-surface of high GAP multilayer conductors of 9 L under different strains during 1000 cycles.

Figure 5-4. SAXS and simulation analysis for percolation network of Au NPs in PU matrix under strain. a), Schematic illustration showing experimental setup of in situ SAXS measurement. b), 2D SAXS patterns at selected uniaxial strains of 0%, 50%, and 100% for the pure PU and 50 wt% AuPU nanocomposite films. We summarized the behavior of the Au NPs in the matrix and change in electrical pathway under strain with corresponding schematic illustrations of the behaviour of Au NPs (yellow sphere) and electrical pathway (red line) under strain through SAXS analysis. c, Calculated Hermans orientation factor, f , under strain.

Figure 5-5. Electrochemical performance of stretchable aqueous rechargeable lithium-ion battery based on GAP multilayer conductor as a current collector. a), Cyclic voltammetry profiles of GAP anode (PI/CNT) and GAP cathode (LMO/CNT) at various C-rates in three electrode systems with 1 M Li_2SO_4 electrolyte. b) and c), Galvanostatic charge-discharge curves of GAP cathode and GAP anode, respectively. d), Cycling performance of full battery at a rate of 15 C between 0.0 and 2.0 V in 1 M Li_2SO_4 for 1000 cycles. e), Schematic illustration of the stretchable aqueous rechargeable lithium-ion battery that was fabricated by using the GAP anode and cathode with coplanar layout. f), Cycle performance of the stretchable full cell at a rate of 15 C under various strains from 0% to 30% for 100 cycles.

Nomenclature

PVdF	poly(vinylidene fluoride)
PVdF-TFP	poly(vinylidene fluoride-tetrafluoroethylene-propylene)
Ag NPs	silver nanoparticles
SBS	poly(styrene- <i>b</i> -butadiene- <i>b</i> -styrene) polymer
Au NPs	gold nanoparticles
SEM	scanning electron microscopy
XRD	X-ray diffraction
CE	coulombic efficiency
PC	polycarbonate
Li₂SO₄	Lithium sulfate
NMP	N-methyl Pyrrolinone
DI water	deionized water
EC	ethylene carbonate
EDX	energy-dispersive X-ray spectroscopy
EIS	electrochemical impedance spectroscopy
CV	cyclic voltammetry
PET	polyethylene terephthalate
EtOH	ethanol
SAXS	small angle X-ray scattering
EIS	electrochemical impedance spectroscopy
FEC	fluoroethylene carbonate
FT-IR	fourier transform infrared
GPE	gel polymer electrolytes
HCl	hydrochloric acid
HMIM	2-Methylimidazole
TEM	transmission electron microscopy
ICE	initial coulombic efficiency
PI	poly imide
LFP	lithium iron phosphate
LIB	lithium-ion battery
CB	carbon black
LiPF₆	lithium hexafluorophosphate
CNT	carbon nanotube

LTO	lithium titanate
PDMS	poly(dimethylsiloxane)
LbL	layer by layer
CbC	composite by composite
ARLBs	aqueous rechargeable lithium ion batteries
CMC	carboxymethylcellulose
PU	polyurethane
GAP	gradient assembled polyurethane based electrode
AgNW	silver nanowire
MF	micro fiber
Al	aluminum
Cu	copper
LEDs	light emitting diodes
HCP	hybrid carbon composite
LMO	lithium manganese oxide
AC	activated carbon
Zn	zinc

1. Introduction

1.1 Background

Conventional electronics based on brittle and rigid materials, including single-crystal silicon, metal oxide films, and polycrystalline metal, are not appropriate for applications where a huge deformability is essential^[1,2]. Unlike traditional hard predecessors in the last decades, flexible electronics has received research interests for their promising potential applications such as a flexible display^[3], flexible solar cells, flexible energy storage devices^[4], and flexible nanogenerators^[5]. Furthermore, manufacturability of flexible electronics was improved by developing various processing approaches including 3D printing^[6] and stencil printing^[7,8]. However, flexible electronics confront a limitation for advanced applications such as wearable devices which endure complex physical stress of human body and cloth (> 30% and > 100% strain at skins and joints, respectively)^[9-11].

Stretchable electronics as an alternative to flexible electronics are attracting intensive attention as the next-generation electronics for use in potential applications in wearable devices^[12,13]. After introducing stretchable concept, many scientists and engineers have widely studied a rich variety of fabrication processes to impart stretchable characteristics to brittle materials. In general, main approaches have been proposed to make stretchable electronics such as (i) buckled configuration and (ii) island-bridge layout.

Buckled structure, which called by wave configuration or pre-strain system, was firstly reported by Whitesides and Bowden^[14]. This geometry configuration can accommodate a large physical stretching by changing the wave amplitudes and wavelength to avoid destroying the materials. The fabrication of buckled structure was conducted by the following steps. First, we prepared rigid materials (*i.e.*, metals and semiconductors) and elastomeric supports (*i.e.*, poly(dimethylsiloxane) (PDMS) and poly urethane). Second, metal electrode was transferred to a pre-strain elastic polymer by using chemical bonds and last, relaxing the strain in the elastomeric substrate. Another strategy of stretchable electronics is island-bridge configuration comprised of the rigid active part connected with conductive metal interconnects onto the elastomeric substrate such as PDMS^[15]. Next version of interconnected-island mesh configuration has been studied as non-coplanar mesh design^[16].

As direct applications of stretchable electronics, wearable devices have led the paradigm shift

in the consumer electronics such as implantable medical devices^[17], healthcare devices^[18], artificial skins^[19], and robotics with arbitrarily shaped surfaces^[20]. Thus, there has been growing interest in the development of wearable devices that can keep their stable function under various deformation states such as bending, crumpling, folding, and even stretching^[21,22].

Stretchable electronics

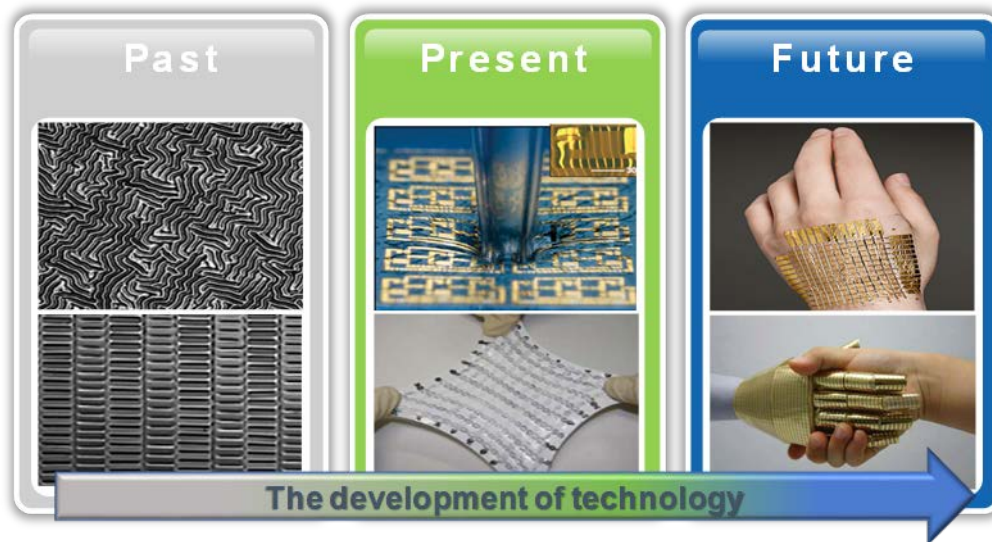


Figure 1-1. The development of stretchable electronics.

❖ **Technology roadmap of wearable devices**

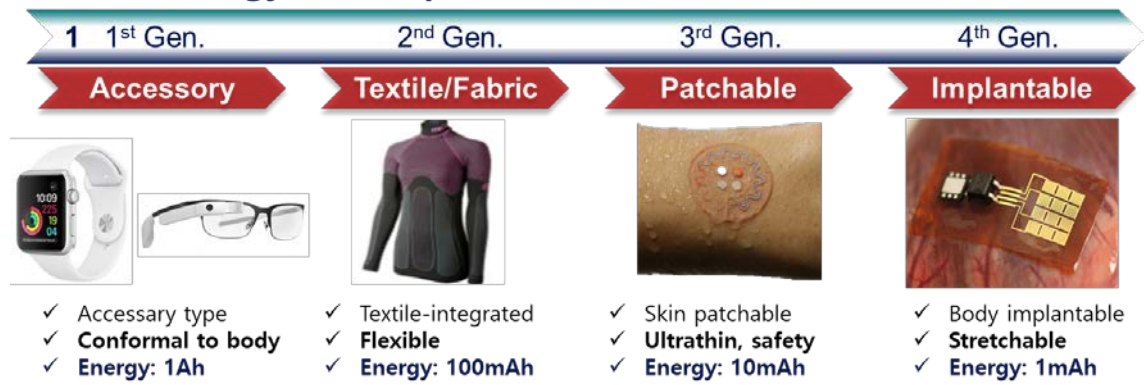


Figure 1-2. Technology roadmap of wearable devices^[23, 24].

1.2 Deformable batteries

For highly reliable wearable electronics such as implantable devices and electronics skins to be developed, their components must be stretched^[23]. The development of deformable energy devices for powering a wearable device is a key challenge for designing complete and independent wearable devices. Thus, stretchable power accessory should accommodate a huge physical deformation. Up to date, various studies have successfully achieved the deformable energy devices^[2] such as supercapacitor^[26], aqueous metal-ion batteries^[27], zinc-based batteries^[28], and lithium-ion batteries (LIBs)^[29]. Despite tremendous promising results, much efforts are required to be used in stretchable battery fields to keep pace with rapidly growing wearable devices^[30]. Thus, the development of deformable batteries, which can be incorporated with wearable devices to power such devices, is highly desired.

From the viewpoint of battery system, one of the key issues of stretchable energy storage devices for wearable devices (on-body and implantable devices) is safety^[31]. Although LIBs have been frequently used to portable electronics owing to their many advantages such as their wide operating voltage range, no memory effect, long-term cyclability and high-energy density, they are predominantly based on flammable and toxic organic electrolytes^[32]. The high hazard of explosion results in internal-short and thermal runaway problems due to the reactivity of active materials with the organic electrolyte during repeated stretching-releasing processes. This safety issue demonstrates the limitations of LIBs as a power accessory for wearable devices^[33].

Batteries based on water-based chemistry such as zinc-based batteries and aqueous metal-ion (Li or Na) batteries, are one of the most ideal candidates as deformable power source for wearable electronics because aqueous electrolytes are naturally safe and high ionic conductivity (that is, fast charge/discharge) compared to organic electrolytes^[34]. Furthermore, the aqueous electrolytes are inexpensive to manufacture and environment-friendly^[35]. For these reasons, the aqueous electrolyte-based batteries are a plausible answer to the deformable power sources.

Among them, zinc-based alkaline batteries, including zinc-air, zinc-manganese dioxide (MnO_2), zinc-nickel and zinc-silver, have aroused extensive interest in both batteries and electronics societies because Zn is globally available, inexpensive, and high energy energy-to-weight ratio. Zinc-based batteries have already been used in small devices and large-scale applications. Several approaches have been proposed for designing deformable zinc batteries, particularly using concepts of tattoo-based batteries, all-printed batteries, and cable-type batteries so far. These innovative approaches dedicated to fabricating wearable energy devices with high energy density,

long-term cyclability, and high deformability.

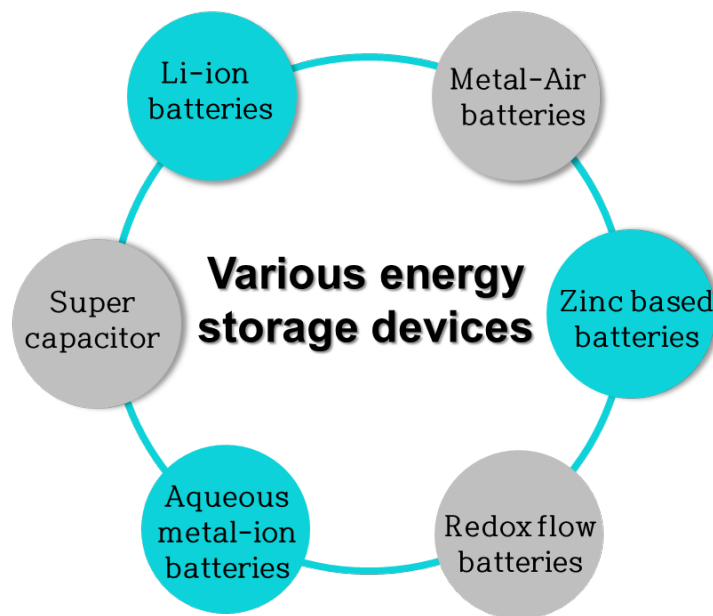


Figure 1-3. Various energy-storage devices.

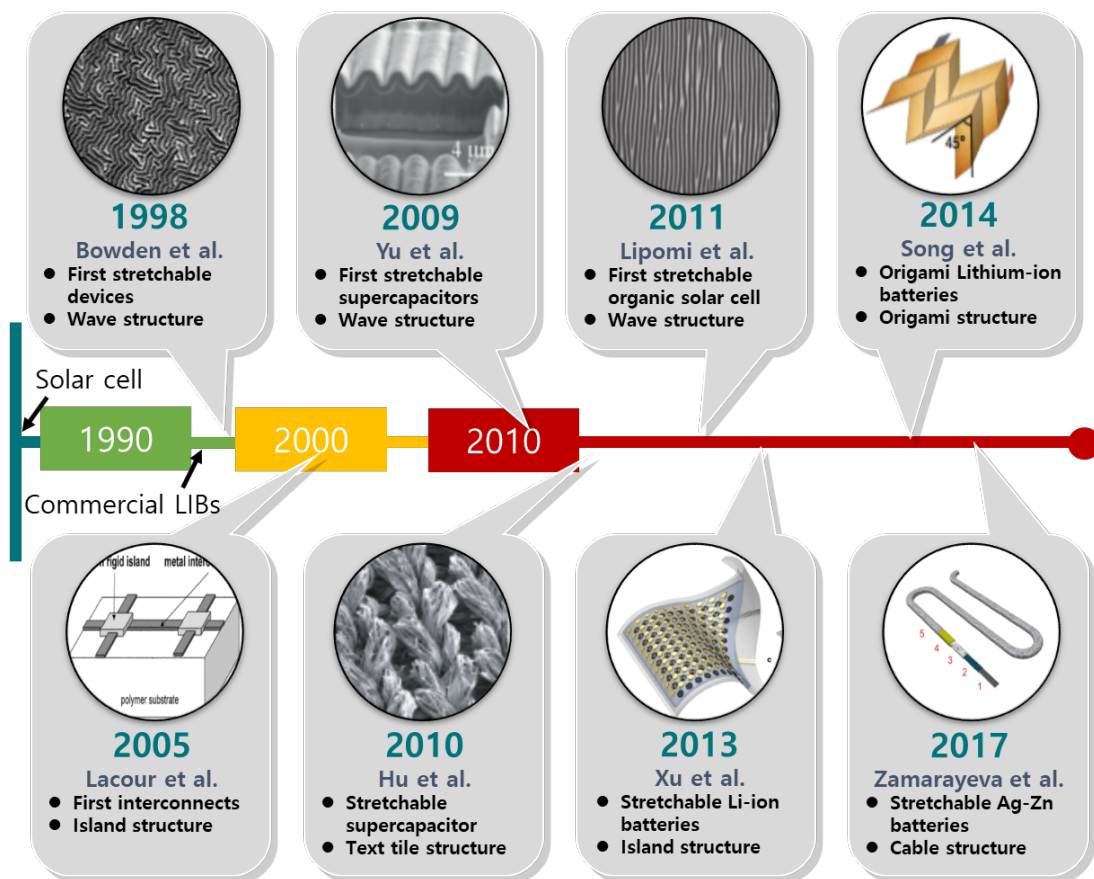


Figure 1-4. A time line of stretchable energy storage and conversion devices^[19, 26,31, 30-33, 34]

1.3 Deformable electrodes

In general, batteries consist of active materials (*i.e.*, anode and cathode materials), polymeric binder (*i.e.*, poly(vinylidene fluoride) and nafion), current collector (*i.e.*, aluminum, copper, and nickel), and packaging materials (*i.e.*, aluminum laminated film). As a core component of batteries, a conventional three-component-electrode currently used in practical batteries consists of micro- or nano-particles held by a polymeric binder on metal current collectors^[35-38]. The electrode is generally heavy and rigid because of the fabrication processes based on slurry-casting method^[39]. For this reason, the conventional electrodes are not enough to accommodate substantial physical stress. Active materials are obviously delaminated from current collector by repeated physical stress because the electrode is intrinsically non-deformable^[40].

A deformable electrode poses a critical hurdle to the innovative progress of the stretchable energy source due to the trade-off relation between electrical conductivity and stretchability^[41]. To realize stretchable energy-storage devices with high performance under mechanical stress, many researchers have developed various geometrical strategies including serpentine interconnects^[42], origami^[43], buckled structure^[44], and spring-like structure^[45].

Although many research efforts have been devoted, these strategies do not sufficiently meet the requirements of practical applications due to high-cost and complex manufacturing process^[46,47]. Alternatively, polymer nanocomposite, which a conductive filler is embedded into an insulating polymeric matrix, is a fascinating alternative for the fabrication method of stretchable current collectors to overcome the above issues owing to their advantage of a large-scalable and high-throughput process^[48,49]. From the viewpoint of methodology, *in situ* small-angle X-ray scattering experiment is a suitable analysis method for monitoring the structural evolution of conductive fillers with nanosize in elastomer^[50]. Electrical conductivity is strongly related to connectivity between conductive fillers. Understanding the percolation behavior of conductive polymer composites, therefore, is crucial for the prediction of the electrical properties of stretchable electrodes^[51]. These fabrication and measurement strategies offer opportunities to develop next-generation highly stretchable and mechanically durable electrode for future stretchable batteries and wearable devices.

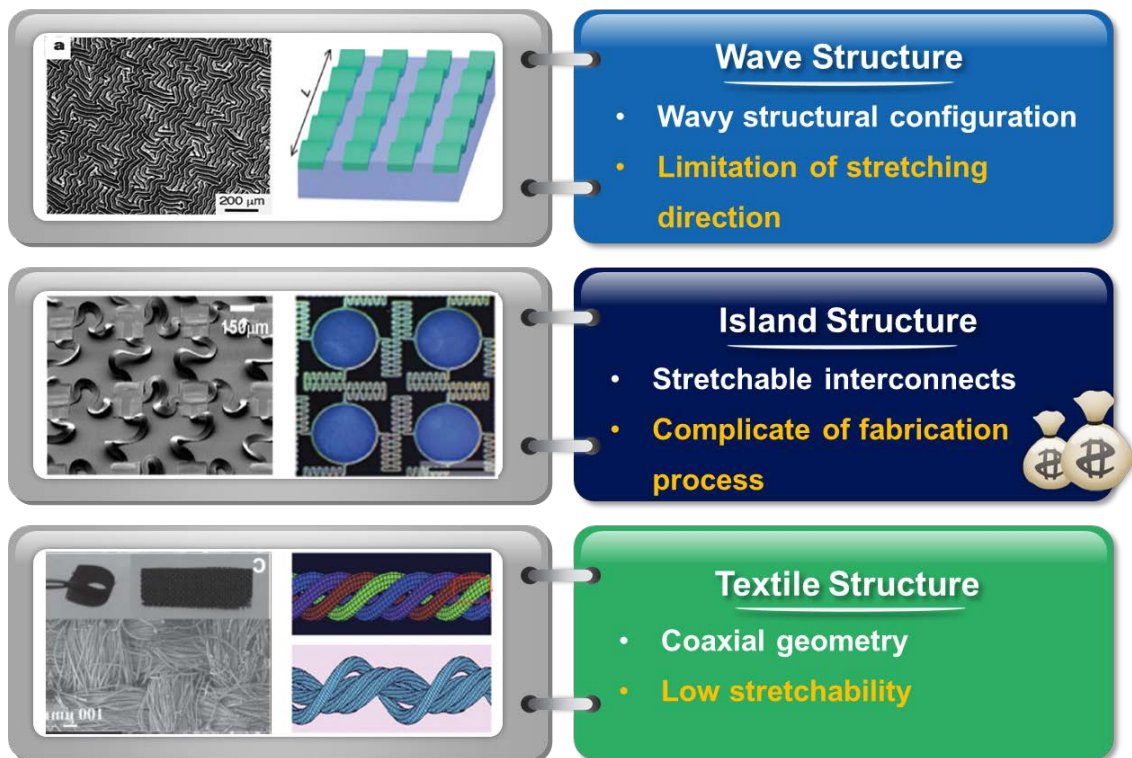


Figure 1-5. Various fabrication methods of stretchable electrode such as wave structure, island structure, and textile structure^[35, 36, 48].

1.4 Reference

- [1] K. H. Choi, S. J. Cho, S. H. Kim, Y. H. Kwon, J. Y. Kim, S. Y. Lee, *Adv. Funct. Mater.* **2014**, *24*, 44.
- [2] J. A. Rogers, Y. Huang, *Proc. Natl. Acad. Sci. USA* **2009**, *106*, 10875.
- [3] M. C. LeMieux, Z. Bao, *Nat. Nanotechnol.* **2008**, *3*, 585.
- [4] S. Hong, S. Myung, *Nat. Nanotechnol.* **2007**, *2*, 207.
- [5] A. Russo, B. Y. Ahn, J. J. Adams, E. B. Duoss, J. T. Bernhard, J. A. Lewis, *Adv. Mater.* **2011**, *23*, 3426.
- [6] S. Ju, A. Facchetti, Y. Xuan, J. Liu, F. Ishikawa, P. Ye, C. Zhou, T. J. Marks, D.B. Janes, *Nat. Nanotechnol.* **2007**, *2*, 378.
- [7] S. Park, M. Vosguerichian, Z. Bao, *Nanoscale* **2013**, *5*, 1727.
- [8] A. Manekkathodi, M. Y. Lu, C. W. Wang, L. J. Chen, *Adv. Mater.* **2010**, *22*, 4059.
- [9] H. Jinno, K. Kuribara, M. Kaltenbrunner, N. Matsuhisa, T. Someya, T. Yokota, T. Sekitani, *Nat. Commun.* **2015**, *6*, 7461.
- [10] M. A. Case, H. A. Burwick, K. G. Volpp, M. S. Patel, *Jama* **2015**, *313*, 625.
- [11] T. Sekitani, H. Nakajima, H. Maeda, T. Fukushima, T. Aida, K. Hata, T. Someya, *Nat. Mater.* **2009**, *8*, 494.
- [12] T. Sekitani, T. Someya, *Adv. Mater.* **2010**, *22*, 2228.
- [13] J. A. Rogers, T. Someya, Y. G. Huang, *Science* **2010**, *327*, 1603.
- [14] C. Pang, C. Lee, K. Y. Suh, *J. Appl. Polym. Sci.* **2013**, *130*, 1429.
- [15] S. Choi, H. Lee, R. Ghaffari, T. Hyeon, D. H. Kim, *Adv. Mater.* **2016**, *28*, 4203.
- [16] M. Ramuz, B. C. K. Tee, J. B. H. Tok, Z. Bao, *Adv. Mater.* **2012**, *24*, 3223.
- [17] J. C. Yeo, H. K. Yap, W. Xi, Z. Wang, C. H. Yeow, C. T. Lim, *Advanced Materials Technologies* **2016**, *1*, 3.
- [18] D. J. Lipomi, M. Vosgueritchian, B. C. Tee, S. L. Hellstrom, J. A. Lee, C. H. Fox, Z. Bao, *Nat. Nanotechnol.* **2011**, *6*, 788.
- [19] D. J. Lipomi, B. C. K. Tee, M. Vosgueritchian, Z. Bao, *Adv. Mater.* **2011**, *23*, 1771.
- [20] M. Amjadi, K. U. Kyung, I. Park, M. Sitti, *Adv. Funct. Mater.* **2016**, *26*, 1678.
- [21] W. Liu, M. S. Song, B. Kong, Y. Cui, *Adv. Mater.* **2017**, *29*, 1603436
- [22] D. Qi, Z. Liu, Y. Liu, W. R. Leow, B. Zhu, H. Yang, J. Yu, W. Wang, H. Wang, S. Yin, *Adv. Mater.* **2015**, *27*, 5559.
- [23] W. Liu, Z. Chen, G. Zhou, Y. Sun, H. R. Lee, C. Liu, H. Yao, Z. Bao, Y. Cui, *Adv. Mater.* **2016**, *28*, 3578.

- [24] R. Kumar, J. Shin, L. Yin, J. M. You, Y. S. Meng, J. Wang, *Adv. Energy Mater.* **2017**, 7.
- [25] W. J. Song, J. Park, D. H. Kim, S. Bae, M. J. Kwak, M. Shin, S. Kim, S. Choi, J. H. Jang, T. J. Shin, S. Y. Kim, K. Seo, S. Park, *Adv. Energy Mater.* **2018**, 8, 1702478
- [26] H. Li, Y. Ding, H. Ha, Y. Shi, L. Peng, X. Zhang, C. J. Ellison, G. Yu, *Adv. Mater.* **2017**, 29, 23.
- [27] Y. Sun, J. Lopez, H. W. Lee, N. Liu, G. Zheng, C. L. Wu, J. Sun, W. Liu, J. W. Chung, Z. Bao, *Adv. Mater.* **2016**, 28, 2455.
- [28] Y. Ma, X. Feng, J. A. Rogers, Y. Huang, Y. Zhang, *Lab on a Chip* **2017**, 17, 1689.
- [29] X. Ning, X. Wang, Y. Zhang, X. Yu, D. Choi, N. Zheng, D. S. Kim, Y. Huang, Y. Zhang, J. A. Rogers, *Adv. Mater. Interfaces* **2018**, 1800284.
- [30] D. H. Kim, J. A. Rogers, *Adv. Mater.* **2008**, 20, 4887.
- [31] K. Abraham, *Electrochim. Acta* **1993**, 38, 1233.
- [32] C. Hwang, W. J. Song, J. G. Han, S. Bae, G. Song, N. S. Choi, S. Park, H. K. Song, *Adv. Mater.* **2018**, 30, 1705445
- [33] H. Nishide, K. Oyaizu, *Science* **2008**, 319, 737.
- [34] A. M. Gaikwad, G. L. Whiting, D. A. Steingart, A. C. Arias, *Adv. Mater.* **2011**, 23, 3251.
- [35] L. Hu, M. Pasta, F. La Mantia, L. Cui, S. Jeong, H. D. Deshazer, J. W. Choi, S. M. Han, Y. Cui, *Nano Lett.* **2010**, 10, 708.
- [36] S. Xu, Y. Zhang, J. Cho, J. Lee, X. Huang, L. Jia, J. A. Fan, Y. Su, J. Su, H. Zhang, *Nat. Commun.* **2013**, 4, 1543.
- [37] Z. Song, T. Ma, R. Tang, Q. Cheng, X. Wang, D. Krishnaraju, R. Panat, C. K. Chan, H. Yu, H. Jiang, *Nat. Commun.* **2014**, 5, 3140.
- [38] C. Wang, W. Zheng, Z. Yue, C. O. Too, G. G. Wallace, *Adv. Mater.* **2011**, 23, 3580.
- [39] Y. Zhang, Y. Huang, J. A. Rogers, *Curr. Opin. Solid State Mater. Sci.* **2015**, 19, 190.
- [40] K. Xie, B. Wei, *Adv. Mater.* **2014**, 26, 3592.
- [41] H. Lee, J. K. Yoo, J. H. Park, J. H. Kim, K. Kang, Y. S. Jung, *Adv. Energy Mater.* **2012**, 2, 976.
- [42] A. M. Gaikwad, A. M. Zamarayeva, J. Rousseau, H. Chu, I. Derin, D. A. Steingart, *Adv. Mater.* **2012**, 24, 5071.
- [43] C. Yan, X. Wang, M. Cui, J. Wang, W. Kang, C. Y. Foo, P. S. Lee, *Adv. Energy Mater.* **2014**, 4, 5
- [44] S. Yoo, J.-H. Kim, M. Shin, H. Park, J.-H. Kim, S.-Y. Lee, S. Park, *Sci. Adv.* **2015**, 1, e1500101.
- [45] J. I. Kim, Y. Choi, K. Y. Chung, J. H. Park, *Adv. Funct. Mater.* **2017**, 27, 34
- [46] A. M. Zamarayeva, A. M. Gaikwad, I. Deckman, M. Wang, B. Khau, D. A. Steingart, A.

- C. Arias, *Adv. Electron. Mater.* **2016**, 2, 5
- [47] Z. Guo, L. Chen, Y. Wang, C. Wang, Y. Xia, *ACS Sustainable Chem. Eng.* **2017**, 5, 1503.
- [48] W. Zuo, W. Zhu, D. Zhao, Y. Sun, Y. Li, J. Liu, X. W. D. Lou, *Energy Environ. Sci.* **2016**, 9, 2881.
- [49] N. Bowden, S. Brittain, A. G. Evans, J. W. Hutchinson, G. M. Whitesides, *Nature* **1998**, 393, 146.
- [50] S. P. Lacour, J. Jones, S. Wagner, T. Li, Z. Suo, *Proc. IEEE* **2005**, 93, 1459.
- [51] C. Yu, C. Masarapu, J. Rong, B. Wei, H. Jiang, *Adv. Mater.* **2009**, 21, 4793.

Chapter II. Foldable Electrode Architectures Based on Silver-nanowire-wound or Carbon-nanotube-webbed Micrometer-scale fibers of Polyethylene Terephthalate Mats for Flexible Lithium Ion Batteries

2.1 Introduction

The development of flexible portable electronics, such as roll-up displays^[1], implantable medical devices^[2, 3] and wearable devices^[4], has been considered as the next-generation devices. To fulfill the demands for reliable flexible electronics, energy storage devices have been required to be mechanical flexible properties as well as high energy density^[5, 6]. Among various energy storage devices, lithium-ion batteries (LIBs) are a promising device owing to their high energy density, wide operating voltage and long-term stability^[7-9]. However, a conventional LIB is difficult to utilize for flexible battery due to its poor mechanical stability under external stress^[10, 11]. A conventional three-component-electrode currently used in LIBs consists of micro or nanoparticles held by a polymeric binder on metal current collectors^[12]. To realize high energy density, the electrode thickness should be dramatically increased^[13]. Unfortunately, the thick electrode provides non-uniform and sluggish Li-ion and electron transport due to the limitation of mass transport and poor electrical pathway^[14]. From the viewpoint of electrode architecture, physical interaction between substrate and electrode component or itself is considerably important in order to obtain stable and robust flexible LIBs^[15]. Furthermore, the conventional electrode is easily delaminated and broken under frequent mechanical stress, because materials constituting the electrode are intrinsically non-flexible and rigid^[5, 11]. Recently, to achieve advanced LIBs with high energy density and flexibility, numerous papers have been reported including self-standing carbon-based electrodes (e.g., graphene, carbon nanotube and carbon fiber)^[16-20], highly porous and flexible substrates (e.g., nickel mesh and carbon cloth)^[21-24] and thin films methods on flexible substrate by using evaporation or sputter tools^[25, 26]. Even though previous works showed good performance in terms of energy density and flexibility, the results are still struggling in flexibility, electrochemical kinetics and loading density of active materials.

Herein, we demonstrate a fabrication of crumpled and super-flexible electrode based on nanowire-wound micro-fiber substrate (NWFS), which consist of conductive nanowires (carbon nanotube (CNT), silver nanowire (AgNW)) as binder and conducting agents, porous nonwoven substrate (polyethylene terephthalate, PET), active materials and itself. The NWFS electrode is simply fabricated by ultrasonic-spray coating method without an additional polymeric binder,

conducting agents and metal current collectors. The conductive nanowires and micro-fiber of nonwoven substrate make three-dimensionally interconnected network structure. These novel architectures provide high mechanical durability and electron percolation network during the repeating extreme deformation. For these reasons, the described electrodes guarantee excellent physical winding and exceptional electrical conductivity even after 1000 folding cycles. The NWFS electrodes not only exhibit long-term cycling stability (150 mA h g^{-1} at a discharge/charge rate of 1C/1C after 1000 cycles) and high rate performance compared to commercial LIB architecture, but also provide an opportunity for increasing energy density through electrode stacking by folding. To further assert the relevance of our designed architecture as a reliable flexible power source, the full cell, which composed of with AWFS (AgNW-wounded micro-fiber substrate) as an anode and CWFS (CNT wound microfiber substrate) as a cathode, is fabricated. This flexible full cell batteries show exceptional electrochemical performance and eminent mechanical stability even at high mass loading (5 mg cm^{-2}) condition after repeatedly folding and crumpling process, opening up a new route to develop high performance deformable LIBs.

2.2 Experimental

Electrodes

Non-woven PET MF mats (Amotech) were coated with an aqueous mixture of nanowires and active materials by using ultrasonication spray (Sono-Tek) equipped with a 120 kHz nozzle. One of the coating solutions of nanowires and active materials was sprayed on the PET MF mats loaded on a hot stage at 150 °C at a flow rate up to 0.2 ml min⁻¹. The spray nozzle was moved at 0.2 cm s⁻¹ in the *x*-*y* plane to cover a large electrode area. The spraying process was repeated to obtain the desired loading. AgNW (Nanopyxis) or CNT (single wall; Meijo Nano Carbon) was used as the nanowires. Lithium titanate (LTO, Li₄Ti₅O₁₂; Ishihara Sangyo Kaisha) and lithium iron phosphate (LFP, LiFePO₄; Süd-Chemie) were used as active materials of anodes and cathodes, respectively. A rubber cylindrical roller (diameter = 30 mm) was rolled several times on the electrodes for pressing. The aqueous coating solutions were prepared by 30 min ultrasonication of a mixture of aqueous dispersions of nanowires and active materials in 2:8 by solid contents. 30 mg mL⁻¹ AgNW (aq) or 1 mg mL⁻¹ CNT (aq) was used for the aqueous nanowire dispersion while 30 mg mL⁻¹ LTO (aq) or 30 mg mL⁻¹ LFP (aq) was used for the aqueous active material dispersion. 10 mg mL⁻¹ sodium dodecylbenzenesulfonate (SDBS, Sigma Aldrich) was used for dispersing CNT in water. CNT-containing electrodes were washed several times by distilled water and ethanol to remove surfactants. AgNW and CNT-coated PET MF mat electrodes were denoted by AgNW\$MF and CNT#MF, respectively.

Cell

Half cells were tested in 2032 coin-type cells while full cells were assembled as a form of 5 cm x 3 cm pouch-type cells. All cells were assembled in an Ar-filled glove box. A porous polyethylene membrane (Asahi NH 716) was sandwiched by two electrodes. LTO-loaded CNT#MF or LTO-loaded AgNW\$MF was assembled with lithium metal in coin-type cells. LFP-loaded CNT#MF cathode and LTO-loaded AgNW\$MF anode were assembled in flexible pouches. Aluminum and nickel lead tabs were attached to cathode and anode respectively by a polyimide tape. 1 M LiPF₆ in ethylene carbonate/diethyl carbonate (EC:DEC in 3:7 by weight; Panax Etec) was used as electrolyte.

Characterization

Electrode morphology was investigated by a scanning electron microscope (SEM; FEI Verios 460). Electrical conductivities and sheet resistances of flat electrodes were measured by using the

four-point probe method (Dasol FPP-RS8). Resistances of electrodes experiencing folding followed by unfolding were recorded by a multimeter. The repeated folding/unfolding was conducted by a tensile strength machine (Petrol LAB DA-01). Sample electrodes were electrically connected via silver paste to gold-coated jigs to fix them in the machine. Resistances of electrodes bent along cylinders of various diameters were measured by a multi-meter. The coin-type and pouch-type half cells and the pouch-type full cells were lithiated and delithiated galvanostatically by a cycle tester (WonATech WBCS 300) and the capacities of lithiation and delithiation were measured. During the electrochemical measurements, the pouch-type cells were folded at a desired angle by using the tensile strength machine.

2.3 Results and discussion

The architectures, we present herein, showed ultra-flexibility that tolerate folding, bending, and crumpling. Even when the folded edges of the battery cells based on our electrode architectures were repeatedly hammered, the light-emitting diode (LED) did not flicker. The super-flexible electrodes were realized by using two types of NW-around-MF (NW@MF) architectures: (1) AgNW\$MF (AgNW-wound MF; \$ stands for *wound* with | = MF and S = NW) and (2) CNT#MF (CNT-webbed MF; # stands for *webbed* with vertical and horizontal lines = NWs). AgNW\$MF was obtained by winding the MFs of a porous nonwoven polyethylene terephthalate (PET) mat (**Figure S2a**) with conductive AgNWs. The AgNW\$MF-based electrodes were used for anodes in this study. On the other hand, CNTs were used as NWs for cathodes because AgNW was oxidized at the cathode potentials of LIBs. CNT#MF was obtained by webbing the MFs with CNTs. Active materials are trapped between the NWs and MFs without polymeric binders, carbon black, and metal current collectors. The conductive NWs were percolated to form a three-dimensionally interconnected network that provides high mechanical durability during repeated extreme deformation.

Both NW@MF architectures were fabricated using the ultrasonic spray method (**Figure 1a** for AgNW\$MF). Well-dispersed mixtures of active materials and conductive NWs (8:2, w/w) in water were introduced into a nozzle, ultrasonicated within the nozzle at 120 kHz and then sprayed onto PET nonwoven mats. The ultrasonication was required for homogeneous dispersion between active materials and NWs in a completely mixed way (**Figure S3**). The PET mats consisted of 2 to 3 layers of MFs with micrometer-scale macro-voids from the top views and sub-micrometer gaps between layers from the lateral views (**Figure S4**). Good wettability of water on the macro-void PET mats (contact angle of water < 5°; **Figure S5**) allowed aqueous droplets of spray ink to penetrate voids and inter-layer gaps and then contact whole surface of MFs. The solvent was dried at 150 °C immediately after the contact between the ink and the substrate. NWs and LTO particles were loaded on surface of both the front layer and the inner layers of MFs.

The importance of good wettability of spray ink on substrates in the NW@MF architectures should be emphasized because the physical interaction between NWs and MFs determines adhesion of active materials and layers to substrates. Macro-voids and not-too-hydrophobic surface properties of PET MF mats resulted in the wettability. On the contrary, we could not develop physical anchoring of above-layers to substrates when a nanoporous polyethylene (PE) membrane (pore size = several tens of nm; **Figure S2b**) was used. Ink droplets did not penetrate nanopores of the PE membrane due to nanopores (lotus effects) and hydrophobicity of PE (contact

angle = 114°; **Figure S5**).^[37] A dense film of NWs were built on the PE membrane without NWs implanted in the substrate, which was easily detached from the substrate (**Figure S6 and S8**). The similar macro-void-containing MF mats were used for a laminated architecture in a previously reported work.^[27] Different from our approach, the front surface of the MF mats was coated with hydrophobic materials and nanofiber layers to block penetration of spray ink into space of macro-voids.

In the initial period of spraying (1 s), the MFs of the PET mats were wound with AgNWs (diameters = ~20 nm, lengths = ~20 μm; **Figure 1b**). When NWs are sprayed onto MFs and then they collided with MFs, the collision force makes the shape of ductile AgNWs conformal to surface features of MFs so that a portion of collision force is consumed for the ductile deformation. The reduced collision forces allow AgNWs to wind the MFs (not to bounce from the MF surface). Also, the ductility of Ag drives the formation of interlocking joints between AgNWs at which one AgNW strand is deformed concave to fit to the convex surface of the other AgNW strand (**Figure S8**). When the AgNWs were sprayed for a longer period, larger amounts of AgNWs and active material particles (lithium titanate (LTO) for AgNW\$MF) were found along the curved surfaces of the MFs. After 10 s of spraying, the AgNWs formed an interconnected network, whereas the LTO particles were trapped between the AgNWs and the MFs. The voids between the MFs in the PET mats were filled with LTO particles trapped by the AgNW web. The spraying process where the spray nozzle was moved in the x - y plane to cover a large electrode area was repeated to obtain the desired loading. For example, the LTO loading at 5 mg_{LTO} cm⁻² was achieved by sweeping the nozzle 20 times at 0.2 cm s⁻¹ (Experimental in the supporting information). ~15 μm thick LTO/AgNW (or CNT) layers were loaded above the 16-μm-thick PET MF mats incorporating LTO and AgNW (or CNT) on the MF surfaces and in the inter-MF voids (cross-section image of **Figure 1b**).

Upon twisting and even folding the LTO-loaded AgNW\$MF electrodes, no significant deterioration in their integrity was observed (**Figure 1c**). When the AgNWs were replaced by CNTs (diameter = ~10 nm, length = ~25 μm), the MFs were *not wound* with CNTs but their surfaces were *webbed* with CNTs (CNT#MF in **Figure S9**). A minor portion of CNTs were agglomerated on the MFs, whereas the AgNWs were not. The AgNWs and PET MFs appeared to be more miscible than the CNTs and MFs because Ag is more ductile than carbon materials, and CNT–CNT interactions are stronger than CNT–PET interactions. Also, the interlocking joints developed between AgNWs were not observed between CNTs owing to the inductile properties of CNTs (**Figure S8**). When LTO-loaded NW@MF's were fractured to obtain their cross-sections, AgNWs were very well stuck to MFs (bottom of **Figure S4a**). However, a portion of CNTs were chipped off during fracturing (bottom of **Figure S4b**).

In the electrodes of currently available LIBs, metallic foils on which layers of active material are loaded are served as current collectors for efficient electron supply. In this work, the three-dimensionally interconnected networks guaranteed high electrical conduction without the need for current collectors and polymeric binders. The electrical conductivities of the LTO-loaded AgNW@MF and LTO-loaded CNT@MF electrodes were, respectively, four and two orders of magnitude higher than that of a practical slurry-coated active layer comprising LTO, carbon black, and binder (aluminum current collector excluded; **Figure 1d**). The superior conductivity of AgNW@MF, which was even higher than that of CNT@MF, is primarily attributed to (1) high electric conductivity of Ag (**Figure S10**) and (2) the interlocking joints (**Figure S8**) formed owing to the ductile properties of silver (**Figure S11**), which reduce the contact resistance between the NWs.^[39] Therefore, the LTO-containing AgNW@MF may be used as a stand-alone anode. The absence of current collectors reduces the volume and mass of the electrode, resulting in higher volumetric and gravimetric energy densities (**Figure 1e**). For example, replacing the conventional electrode comprising active layers on current collectors with the stand-alone AgNW@MF electrode containing active materials ($5 \text{ mg}_{\text{LTO}} \text{ cm}^{-2}$) results in a 53% reduction in thickness (from 58 to 31 μm) and a 70% reduction in mass.

For flexibility and foldability, both cohesion among electrode constituent materials and adhesion between active materials and substrates are pivotal factors in mechanical durability. First, the cohesion and/or adhesion were quantified by measuring the masses of the electrodes during folding cycles. The NW@MF architectures including AgNW@MF and CNT@MF did not show any decrease in electrode mass during 1,000 folding cycles in the absence of electrolyte (**Figure 2a**) and 200 folding cycles in the presence of electrolyte (**Figure S12**). It should be emphasized that the NWs (AgNW or CNT) successfully bound the LTO particles to the PET MFs even if no binders were used. In contrast, using the conventional architecture of the active layer on a current collector, 40% of the active layer mass (including LTO, carbon black, and binder polymer) was detached from the aluminum current collector after 100 folding cycles. Secondly, the cohesion/adhesion were estimated by peeling active layers from substrates. The electrodes based on one-dimensional nanowires' intertanglement were superior to the practical electrode based on cohesion/adhesion ability of binders. Active layers containing binders were easily peeled off from metal current collectors (**Figure S7**). However, it was difficult to peel off the active layers containing nanowires in AgNW@MF and CNT@MF.

The superior cohesion/adhesion properties of the NW@MF architecture also resulted in reduced loss of electrical conductivity during bending and folding. Using the conventional electrode architecture, a significant increase in resistance was observed when the bending radius was less than 20 mm (**Figure S13**).^[40] In contrast, the electrical conductivity of the NW@MF

architecture was not affected by bending. No difference in electrical conductivity was observed between AgNW\$MF and CNT#MF upon bending, even when the electrodes were sharply bent. However, a difference was noted after repeated folding (**Figure 2b**). The electrical resistance of LTO-loaded AgNW\$MF ($5 \text{ mg}_{\text{LTO}} \text{ cm}^{-2}$) did not change at all during 1,000 folding cycles even if the interconnected LTO/AgNW network structure was partially changed repeated folding cycles (**Figures 2d–f**). In contrast, at the same LTO loading, the resistance of CNT#MF increased sharply from the initial folding cycle (**Figure 2b**), and clear cracks formed at the 250th folding cycle (**Figure 2h**). CNT#MF was durable over 1,000 folding cycles only when the loading was reduced to one tenth of the above value ($0.5 \text{ mg}_{\text{LTO}} \text{ cm}^{-2}$; **Figures 2b** and **2j**).

It is interesting that the heavily LTO-loaded AgNW\$MF at 5 mg cm^{-2} showed insignificant increase in resistance along the repeated folding (**Figure 2b**) in spite of disappearance of the one-dimensional feature of AgNWs on electrode surface (**Figure 2d to f**). Ductile AgNWs were agglomerated on the surface of folding edges after 1000 folding cycles, losing the one-dimensional feature (**Figure S14a** and **b**). AgNW agglomerates stick to LTO particles were observed on the surface of LTO/AgNW layers on AgNW\$MF. It should be notified that the folding edges were pressed heavily by fingers whenever the electrodes were completely folded. This is supported by the experiment showing that two pieces of AgNW films were easily attached by pressing overlapped parts of the pieces (**Figure S11**). Different from the surface of the thick LTO/AgNW layers, however, AgNW network is expected to be still well developed through the body of LTO/AgNW layers and well stick to the MF surfaces. Lightly LTO-loaded AgNW\$MF containing thin LTO/AgNW layer at 3 mg cm^{-2} showed clear one-dimensional features of AgNWs after 1000 folding (**Figure S14c**). Also, the AgNW-wound MFs were observed in the inner layers of MFs far from the LTO/AgNW layer (**Figure S14d**). Loss of one-dimensional network feature of AgNWs on the surface of LTO/AgNW layers is responsible for the slight increase of resistance along repeated folding cycles.

Stress-strain curves of bare PET mat (MF), AgNW\$MF and CNT#MF were obtained by using a tensile strength machine (**Figure S15**). Young's modulus and yield strength defining elastic region were significantly increased by wrapping MFs with AgNW or CNT: Young's modulus from $\sim 2.6 \text{ MPa}$ (by averaging five runs) for MF to $\sim 4 \text{ MPa}$ for NW@MF; yield strength from $\sim 0.62 \text{ MPa}$ for MF to $\sim 1.7 \text{ MPa}$ for NW@MF. The increase in stiffness is easily understood because MFs were coupled with high-modulus materials (Young's modulus = 83 GPa for Ag bulk and several hundreds GPa for CNT) and the materials resist tensile elongation. However, there are insignificant differences observed for tensile strength at $\sim 4.8 \text{ MPa}$ and rupture strain at $\sim 11 \%$ in plastic region. Interconnected networks of AgNWs and CNTs would be relieved not to affect mechanical properties of MFs significantly in plastic region.

The lithiation/delithiation electrochemistry of LTO was compared between the NW@MF architectures and the conventional architecture comprising an active layer on the current collector (LTO|Al). There was no difference in gravimetric capacity per LTO mass ($\text{mAh g}_{\text{LTO}}^{-1}$) between the two NW@MF architectures and the reference architecture (upper part of **Figure 3a**), indicating that the capacities of LTO in the NW@MF architectures were efficiently utilized. On the other hand, the gravimetric electrode capacities of AgNW\$MF and CNT#MF (per electrode mass in $\text{mAh g}_{\text{ED}}^{-1}$, where ED = electrode) were experimentally estimated to be four times as high as that of the reference electrode (lower part of **Figure 3a**) because of the mass savings of the stand-alone configuration, which excludes current collectors. In addition, the high conductivity of AgNW\$MF (**Figure 1b**) improved the rate capability of LTO included in the electrode (**Figure 3b**). The fast electrochemical kinetics of the LTO-loaded AgNW\$MF electrodes are clearly demonstrated by the differential capacity (dQ/dV) curve (**Figure 3c**). The narrowest gap between the lithiation and delithiation peaks was observed for the highly conductive AgNW\$MF. In addition, overpotentials of both LTO-loaded AgNW\$MF and LTO-loaded CNT#MF were much smaller than those of conventional slurry-coated current collector architecture (Al) in potential profiles obtained during charge and discharge at 1C (**Figure S16**). The potential gaps between charge and discharge at 100 mAh g^{-1} were estimated to be 19 mV for NW@MF versus 46 mV for the slurry-coated architecture.

Based on the durability of AgNW\$MF during folding, folded LTO-loaded AgNW\$MFs were used as the electrodes of LIBs. The overall electrode capacities per geometric area were easily controllable by folding a strip of the extremely flexible AgNW\$MF (photos in **Figure 1e**). For example, the areal capacity of four-layered (4L) AgNW\$MF, which was obtained by folding AgNW\$MF in half two times, was four times as high as that of unfolded (1L) AgNW\$MF (**Figure 3d**). Folding did not reduce the gravimetric capacity per LTO mass so that the LTO capacities of 1L, 2L, and 4L AgNW\$MF along with the conventional slurry-coated LTO|Al were identical at $\sim 150 \text{ mAh g}_{\text{LTO}}^{-1}$. The interconnected network of AgNWs wound around MFs and the inter-fiber voids of the MF matrix are thought to guarantee electrical conduction and ion transport, respectively, even after folding.

Decrease in the mass savings of folded electrodes with increasing number of folds (or the number of layers) was inevitable because greater amounts of MF mats were included (**Figure 1e**). For example at $5 \text{ mg}_{\text{LTO}} \text{ cm}^{-2}$, the 4L AgNW\$MF saved 55% of the reference electrode mass, which is less than the mass saving at 70% of 1L AgNW\$MF. In addition, more stacked electrodes showed poorer rate capabilities because longer Li^+ mass transfer pathways were required to fully utilize the active materials in the more stacked electrodes (**Figure 3e**). Nevertheless, higher capacities of LIB cells at a fixed size were realized over all discharge rates by using the folded

electrodes (low panel of **Figure 3e**).

Pouch-type LTO half cells based on the NW@MF architectures showed good capacity retention under static bending conditions (**Figure 3f**). No capacity decay was observed in the AgNW\$MF and CNT#MF electrodes containing LTO when they were bent at any angle or completely folded. In contrast, the conventional LTO|Al electrode showed a serious capacity drop upon bending at 30°. The superiority of LTO-loaded NW@MF compared to LTO|Al in terms of electrochemical stability under static bending is attributed to the integrity and morphological stability of the NW@MF-based electrodes, which are imparted by the conductive NWs (AgNW and CNT; **Figure 2**).

Super-flexible pouch-type full cells were constructed by loading lithium iron phosphate (LFP) on CNT#MF as the cathode and loading LTO on AgNW\$MF as the anode (AgNW\$MF|LTO||LFP|CNT#MF; **Figure 4a** and **Figure S17**). The capacity ratio of anode to cathode (N/P ratio) was fixed at around 1.2. The mass ratio was identical to the N/P ratio because the capacity of LFP was close to that of LTO. CNTs were used for the cathodes because AgNW is oxidized at the cathode potentials of LIBs. The half cell performances of LFP|CNT#MF were confirmed before full cell experiments. Capacity did not decay at 1C/1C during 100 cycles while it was superior to LFP loaded on aluminum foil (LFP|Al) in terms of rate capability (**Figure S18**). There were no significant morphological changes in LTO-loaded AgNW\$MF and LFP-loaded CNT#MF observed after 100 cycles of charge and discharge at 1C (**Figure S19**). When the fully charged battery full cell was seriously crumpled, the open-circuit voltage (OCV) of the NW@MF-based LTO||LFP cell did not change at all (1.85 V). However, the OCV of the conventional cell based on the active-layer-on-foil architecture dropped seriously from 1.85 to 0.0335 V under the same conditions. The OCV of the conventional cell did not return to the initial value, even when the cell was uncrumpled. The super-flexible NW@MF-based batteries successfully supplied power continuously to LEDs without any intermittent interruption during repeated folding for up to 100 times, severe crumpling, and even the repeated hammering of a folded edge (**Figure 4c** and **Videos S1** and **S5**). Moreover, using the 4L electrodes in both the cathode and anode of the super-flexible NW@MF-based battery (4L-AgNW\$MF and 4L-CNT#MF) increased the capacity by a factor of four. The potential profiles of the 1L- and 4L-based LTO||LFP cells were not significantly different (**Figure 4d**), indicating that the 4L-based cell did not have serious problems related to charge transfer or mass transfer. The 4L-based LTO||LFP cells were as flexible as the unfolded 1L cells; the capacity retention during charge/discharge cycles with intermittent 20 folding and unfolding events every 20 charge/discharge cycles was not different between the 1L and 4L cells (**Figure 4e**). The NW@MF-based LTO||LFP cells presented in this study have the highest loading of active material (3.2 mAh cm⁻²) among reported foldable LIB cells and allow

successful LIB operation under extreme bending (bending radius = 1 mm; **Figure 4f**).^[17]

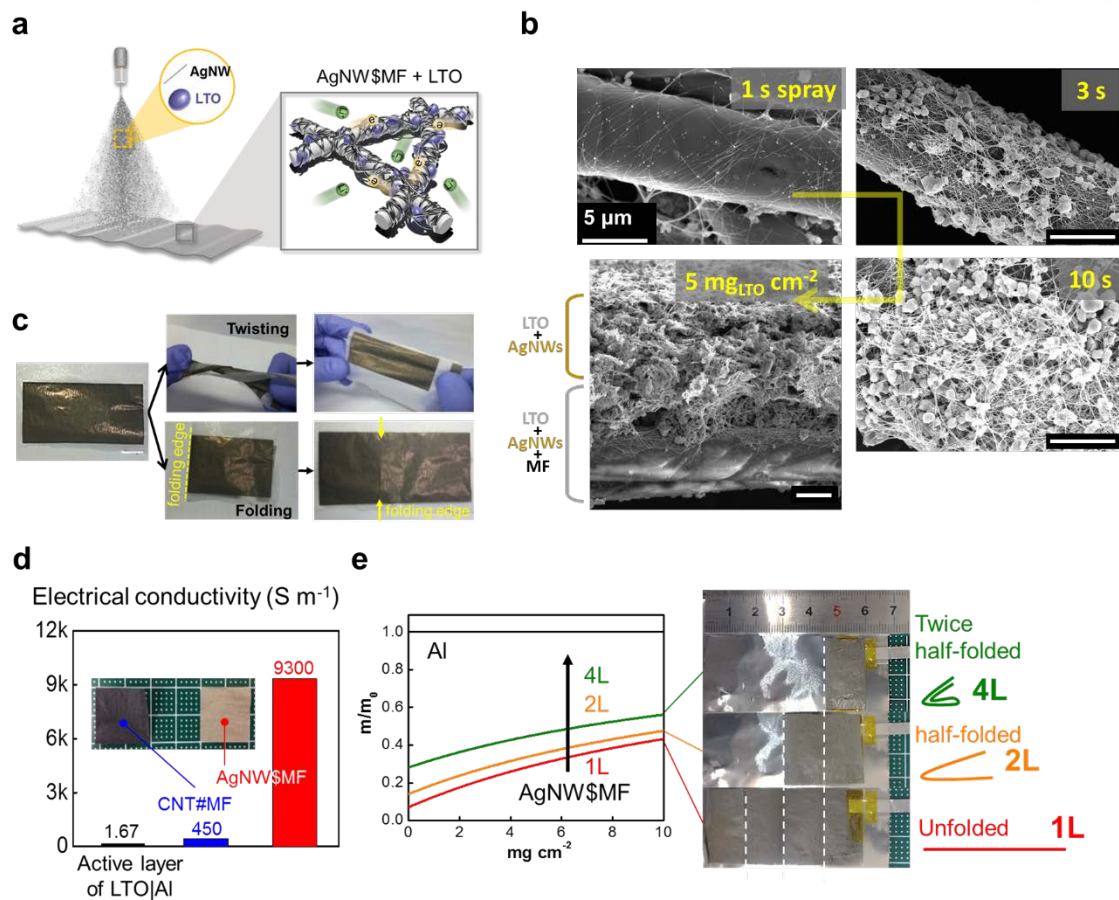


Figure 2-1. LTO-loaded AgNW\$MF. AgNW : MF : LTO = 1 : 1.1 : 5 in weight. Loading density of LTO = $5 \text{ mg}_{\text{LTO}} \text{cm}^{-2}$. a) Fabrication. b) SEM images at three different spray times. c) Visual inspection after twisting and folding. d) Electrical conductivities of LTO-containing electrodes measured by four-point probe methods. Macroscopic thicknesses of electrodes were measured by a vernier caliper. The active layer of LTO|Al consisted of carbon black : binder : LTO = 0.5 : 0.5 : 5 in weight. The CNT#MF containing LTO consisted of CNT : MF : LTO at 1 : 1.1 : 5 in weight. Loading densities of LTO = $4.3 \text{ mg}_{\text{LTO}} \text{cm}^{-2}$ for LTO|Al and $5 \text{ mg}_{\text{LTO}} \text{cm}^{-2}$ for CNT#MF. e) Mass savings by the use of the current-collector-free and binder-free AgNW\$MF. m/m_0 = relative electrode mass with respect to conventional LTO-loaded Al (LTO|Al). Electrode mass is the sum of mass of all components of electrodes including conducting agents, binders and current collectors for LTO|Al and AgNWs and PET MF mats for AgNW\$MF as well as active materials. 2L (L = layer) and 4L AgNW\$MF's were obtained by folding unfolded AgNW\$MF (1L) in half once and twice, respectively. Scales were indicated in cm on the top.

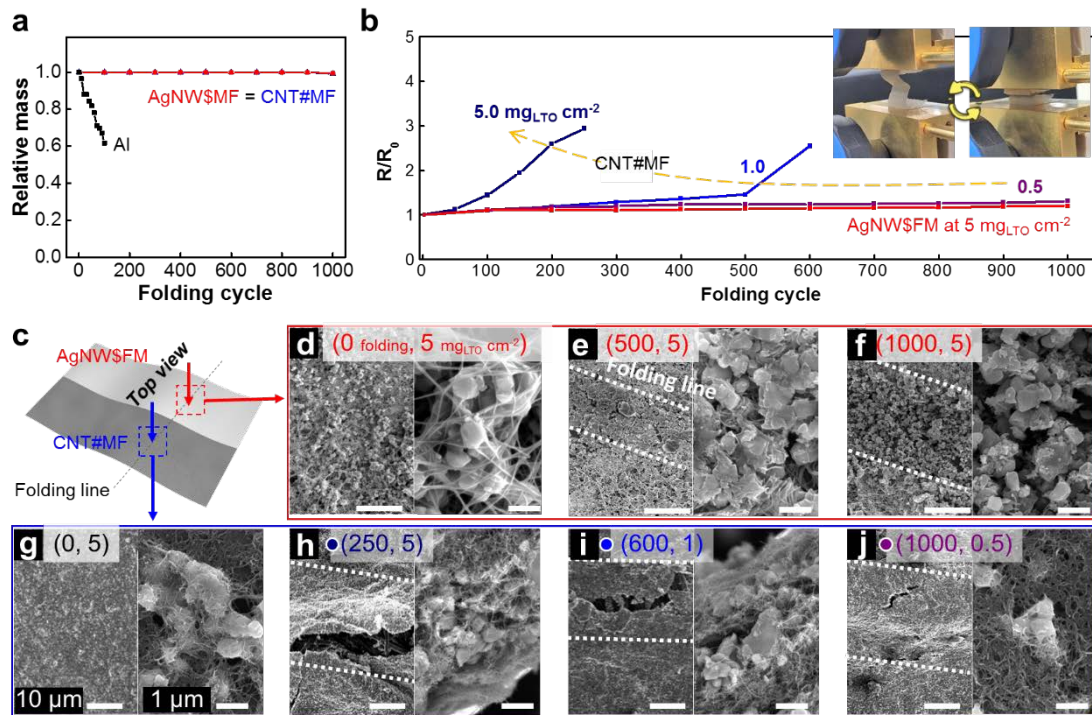


Figure 2-2. Effects of folding deformation on the mass, microstructure, and electrical property of LTO-loaded AgNW\$MF and CNT#MF electrodes. LTO loading = 5 mg_{LTO} cm⁻² unless indicated otherwise. ~5 μm-thick LTO/AgNW (or CNT) layers were loaded above the 16 μm-thick PET MF mats within which LTO and AgNW (or CNT) were incorporated on the surface of MFs and to the inter-MF voids. a) Relative mass change of electrodes after 1000 folding cycles. b) Electrical resistance change along folding cycles. Three different LTO loadings were used for CNT#MF. R₀ and R indicate electrical resistances before and after folding, respectively. c) Positions at which the following SEM images were taken. d to f) Top-view images of LTO-loaded AgNW\$MF: d) before folding, e) after 500 folding cycles and f) after 1000 folding cycles. g to j) Top-view images of LTO-loaded CNT#MF: g) in 5 mg_{LTO} cm⁻² before folding, h) in 5 mg_{LTO} cm⁻² after 250 folding cycles, i) in 1 mg_{LTO} cm⁻² after 600 folding cycles and j) in 0.5 mg_{LTO} cm⁻² after 1000 folding cycles.

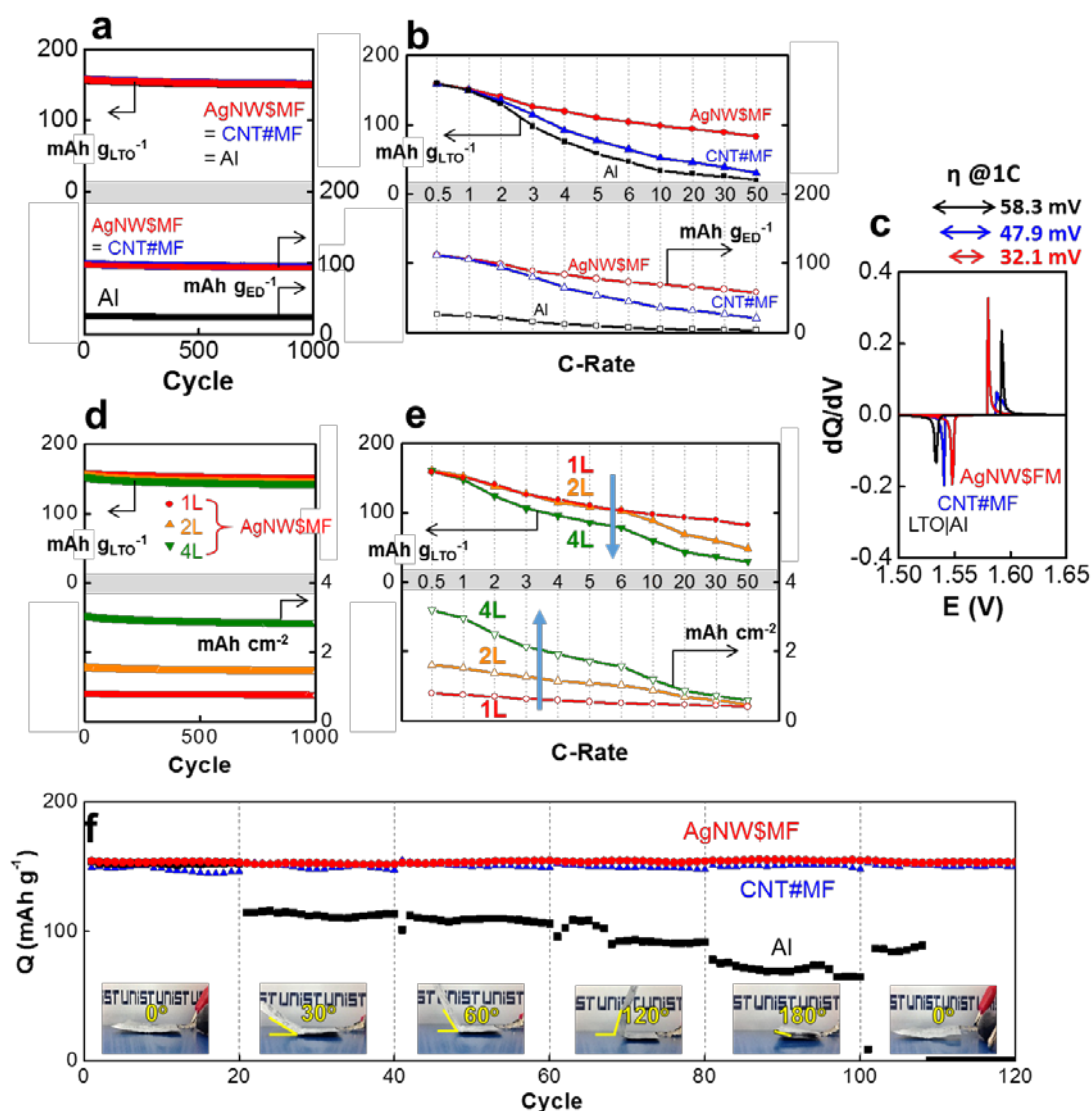


Figure 2-3. Lithiation electrochemistry of LTO loaded on AgNW\$MF, CNT#MF and aluminum foil. Electrode compositions were indicated in Figure 1. Half cell configuration including lithium metal was used for **a** to **c** with a potential range between 1 V and 3 V. Pouch cells were designed in 5 cm x 3 cm to have energy densities at 3 mAh cm⁻² for **d** to **f**. **a**) Capacity retention along repeated charges and discharges at 1C. Capacities were normalized by LTO mass in g_{LTO} (upper position) or total mass (g_{ED}) including an electrode and current collector (lower position). **b**) Rate capabilities. **c**) Differential capacities (dQ/dV) curves at 1C. **d**) Capacity retention of folded AgNW\$MFs (2L and 4L) versus unfolded one (1L) along repeated charges and discharges at 1C. Capacities were normalized by LTO mass in g_{LTO} or geometric electrode area (cm²). **e**) Rate capabilities of folded AgNW\$MFs. **f**) Capacity retention of folded cells at different angles at 1C.

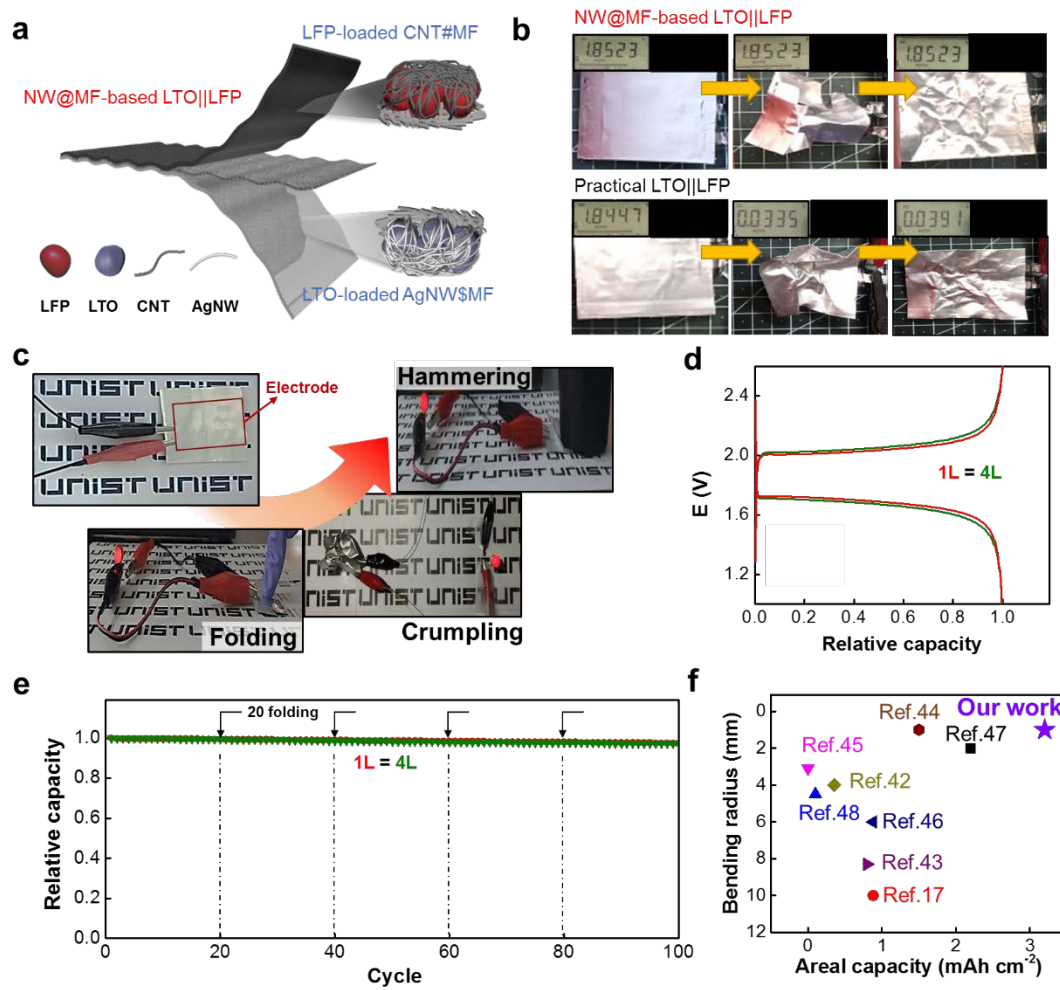


Figure 2-4. Crumple Superflexible batteries consisting of LTO-loaded AgNW\$MF and LFP-loaded CNT#MF (AgNW\$MF|LTO||LFP|CNT#MF). a) The superflexible battery. b) Open circuit voltages of LTO||LFP cells before and after crumpling. c) Red light emitting diodes (LEDs) powered by the NW@MF-based LTO||LFP under folding, crumpling and hammering. d) Voltage profiles of 1L- and 4L-based LTO||LFP at 1C. e) Capacity retention at 1C. The cells were folded 20 times every 20 charge/discharge cycle. f) Comparison of the 4L-NW@MF-based batteries with reported flexible batteries in terms of areal capacities and bending radii.

2.4 Conclusion

In summary, we demonstrated the fabrication of crumbled and super-flexible rechargeable LIBs with high energy density using NWFS-based electrodes. The nanowires of NWFS provided electrically conductive pathways to active materials and also securely maintained 3D interconnected structure under the strong mechanical stresses such as bending, folding and crumpling condition. The outstanding mechanical property of the NWFS electrodes facilitated the enhancement of energy density through stacking process of electrode by folding. In particular, the AWFS electrodes exhibited excellent mechanical durability at high mass loading of active materials, which resulted in outstanding capacity retention and improved rate capabilities at high loading density by stacking method compared to conventional electrode. The excellent electrochemical performance of the AWFS can be explained as follows: (i) The porous structure of electrode provides the large electrochemical active area during lithiation and delithiation, (ii) highly conductive AgNWs provides a percolation network by interlocking joints, (iii) exceptional flexibility by ductile property of AgNWs helps good mechanical durability at harsh conditions such as bending, folding, hammering, and crumpling. We believe that the NWFS-based electrode architecture presented here can be extended to other super-flexible electronic device applications.

2.5 Reference

- [1] Y. Sun, J. A. Rogers, *Adv. Mater.* **2007**, *19*, 1897.
- [2] D.-H. Kim, N. Lu, R. Ghaffari, J. A. Rogers, *Npg Asia Mater* **2012**, *4*, e15.
- [3] J. B. Goodenough, K.-S. Park, *J. Am. Chem. Soc.* **2013**, *135*, 1167.
- [4] S.-Y. Lee, K.-H. Choi, W.-S. Choi, Y. H. Kwon, H.-R. Jung, H.-C. Shin, J. Y. Kim, *Energy Environ. Sci.* **2013**, *6*, 2414.
- [5] S. J. Kim, J. H. We, B. J. Cho, *Energy Environ. Sci.* **2014**, *7*, 1959.
- [6] X. Wang, X. Lu, B. Liu, D. Chen, Y. Tong, G. Shen, *Adv. Mater.* **2014**, *26*, 4763.
- [7] W. Zeng, L. Shu, Q. Li, S. Chen, F. Wang, X.-M. Tao, *Adv. Mater.* **2014**, *26*, 5310.
- [8] H. Wu, Y. Huang, F. Xu, Y. Duan, Z. Yin, *Adv. Mater.* **2016**, *28*, 9881.
- [9] G. Zhou, F. Li, H.-M. Cheng, *Energy Environ. Sci.* **2014**, *7*, 1307.
- [10] L. Li, Z. Wu, S. Yuan, X.-B. Zhang, *Energy Environ. Sci.* **2014**, *7*, 2101.
- [11] H. Gwon, J. Hong, H. Kim, D.-H. Seo, S. Jeon, K. Kang, *Energy Environ. Sci.* **2014**, *7*, 538.
- [12] Y. Hu, X. Sun, *J. Mater. Chem. A* **2014**, *2*, 10712.
- [13] S.-J. Cho, K.-H. Choi, J.-T. Yoo, J.-H. Kim, Y.-H. Lee, S.-J. Chun, S.-B. Park, D.-H. Choi, Q. Wu, S.-Y. Lee, S.-Y. Lee, *Adv. Funct. Mater.* **2015**, *25*, 6029.
- [14] X. Jia, Y. Kan, X. Zhu, G. Ning, Y. Lu, F. Wei, *Nano Energy* **2014**, *10*, 344.
- [15] J.-M. Kim, C.-H. Park, Q. Wu, S.-Y. Lee, *Adv. Energy Mater.* **2016**, *6*, 1501594.
- [16] X. Xiao, X. Peng, H. Jin, T. Li, C. Zhang, B. Gao, B. Hu, K. Huo, J. Zhou, *Adv. Mater.* **2013**, *25*, 5091.
- [17] A. M. Gaikwad, B. V. Khau, G. Davies, B. Hertzberg, D. A. Steingart, A. C. Arias, *Adv. Energy Mater.* **2015**, *5*, 1401389.
- [18] G. Yu, L. Hu, N. Liu, H. Wang, M. Vosgueritchian, Y. Yang, Y. Cui, Z. Bao, *Nano Lett.* **2011**, *11*, 4438.
- [19] G. Yu, L. Hu, M. Vosgueritchian, H. Wang, X. Xie, J. R. McDonough, X. Cui, Y. Cui, Z.

- Bao, *Nano Lett.* **2011**, *11*, 2905.
- [20] J.-Y. Hwang, H. M. Kim, S.-K. Lee, J.-H. Lee, A. Abouimrane, M. A. Khaleel, I. Belharouak, A. Manthiram, Y.-K. Sun, *Adv. Energy Mater.* **2016**, *6*, 1501480.
- [21] Y. Z. Zhang, Y. Wang, T. Cheng, W. Y. Lai, H. Pang, W. Huang, *Chem. Soc. Rev.* **2015**, *44*, 5181.
- [22] H. Wu, Q. Meng, Q. Yang, M. Zhang, K. Lu, Z. Wei, *Adv. Mater.* **2015**, *27*, 6504.
- [23] H. Lu, J. Hagberg, G. Lindbergh, A. Cornell, *Nano Energy* **2017**, *39*, 140.
- [24] H. Gwon, H.-S. Kim, K. U. Lee, D.-H. Seo, Y. C. Park, Y.-S. Lee, B. T. Ahn, K. Kang, *Energy Environ. Sci.* **2011**, *4*, 1277.
- [25] L. Noerochim, J.-Z. Wang, D. Wexler, M. M. Rahman, J. Chen, H.-K. Liu, *J. Mater. Chem.* **2012**, *22*, 11159.
- [26] K.-H. Choi, S.-J. Cho, S.-J. Chun, J. T. Yoo, C. K. Lee, W. Kim, Q. Wu, S.-B. Park, D.-H. Choi, S.-Y. Lee, S.-Y. Lee, *Nano Lett.* **2014**, *14*, 5677.
- [27] K.-H. Choi, J. Yoo, C. K. Lee, S.-Y. Lee, *Energy Environ. Sci.* **2016**, *9*, 2812.
- [28] B. Liu, J. Zhang, X. Wang, G. Chen, D. Chen, C. Zhou, G. Shen, *Nano Lett.* **2012**, *12*, 3005.
- [29] S. Yuan, X.-l. Huang, D.-l. Ma, H.-g. Wang, F.-z. Meng, X.-b. Zhang, *Adv. Mater.* **2014**, *26*, 2273.
- [30] Y.-h. Zhu, S. Yuan, D. Bao, Y.-b. Yin, H.-x. Zhong, X.-b. Zhang, J.-m. Yan, Q. Jiang, *Adv. Mater.* **2017**, *29*, 1603719.
- [31] F. Meng, H. Zhong, D. Bao, J. Yan, X. Zhang, *J. Am. Chem. Soc.* **2016**, *138*, 10226.
- [32] Y.-h. Zhu, Y.-b. Yin, X. Yang, T. Sun, S. Wang, Y.-s. Jiang, J.-m. Yan, X.-b. Zhang, *Angew. Chem. Int. Ed.* **2017**, *56*, 7881.
- [33] Y.-B. Yin, J.-J. Xu, Q.-C. Liu, X.-B. Zhang, *Adv. Mater.* **2016**, *28*, 7494.
- [34] Q. C. Liu, J. J. Xu, D. Xu, X. B. Zhang, *Nat. Commun.* **2015**, *6*, 7892.
- [35] J. Zhu, S. Tang, J. Wu, X. Shi, B. Zhu, X. Meng, *Adv. Energy Mater.* **2017**, *7*, 1601234.
- [36] J. F. Du, Y. R. Kim, H. T. Jeong, *Compos. Interfaces* **2017**, *24*, 99.
- [37] M. Kuang, L. Wang, Y. Song, *Adv. Mater.* **2014**, *26*, 6950.

** Chapter II is reproduced in part with permission of “Chihyun Hwang,[†] Woo-Jin Song,[†] Jung-Gu Han, Sohyun Bae, Gyujin Song, Nam-Soon Choi, Soojin Park,* Hyun-Kon Song*, Foldable Electrode Architectures Based on Silver-nanowire-wound or Carbon-nanotube-webbed Micrometer-scale fibers of Polyethylene Terephthalate Mats for Flexible Lithium Ion Batteries, 2017, 30, 1705445”. Copyright 2017 John Wiley & Sons, Inc.*

Chapter III. Jabuticaba-inspired Hybrid Carbon Filler/Polymer Electrode for Use in Highly Stretchable Aqueous Li-ion Batteries

3.1 Introduction

Stretchable electronics have recently attracted attention in new fields of application,^[1,2] such as strain sensors,^[3] wearable electronics,^[4] and artificial electronic skin.^[5] For highly reliable stretchable electronic devices to be developed, all of their components need to be able to stretch. A key challenge for developing such devices is the creation of deformable energy devices that could power them.^[6] A critical hurdle is how to fabricate such a stretchable electrode because the electrodes in these devices would need to have both high mechanical durability and high electrical conductivity during deformation.^[7,8] Many methods have been proposed for these electrodes, including those having buckled configurations,^[9] interconnected island structures,^[10] and porous frameworks.^[11] However, none of these methods has managed to simultaneously achieve high stretchability for the electrodes and have a scalable manufacturing process.

Conductive polymer composites composed of conductive fillers and elastic polymer matrices are considered promising for the production of stretchable electrodes due to their advantageous features such as being simple to produce, low cost, and a scalable manufacturing process.^[12] Carbon nanotubes (CNT), which have been widely used as conductive fillers, are exemplary polymer composite materials due to their excellent mechanical properties, high aspect ratios, and high electrical conductivities.^[13] However, their application to stretchable composites has been limited for two reasons: (i) the agglomeration of CNT during the preparation of composite results in low electrical conductivity,^[14] and (ii) the percolation network between the CNT is blocked when a composite containing them is stretched.^[15] Recently, Kyrylyuk et al. demonstrated that conductive polymer composites filled with various types of conductive fillers could be fabricated through solution processing.^[16] Meanwhile, Tang et al. reported a highly conductive polymer composite fabricated using self-assembled CNT and graphene fillers.^[17] Although several studies on conductive polymer composites containing carbon fillers have reported improved electrical conductivity in these composites, only a few have investigated the percolation behavior of conductive fillers in polymers when mechanical strain is applied. It is not easy to analyze the behavior of fillers during stretching processes, but a clear understanding of this phenomenon is critical for the design and evaluation of the electrical properties of stretchable electrodes.

Lithium-ion batteries (LIBs) are frequently used to power electronic devices due to their many advantages such as high energy density and long-term cycling life.^[18,19] The LIBs are predominantly based on flammable and toxic organic electrolytes. The risk of them exploding and catching fire due to the reactivity of their electrolytes and active materials during repeated mechanical deformation processes makes them undesirable propositions for stretchable electronic devices.^[20] Furthermore, organic electrolytes are expensive to manufacture and they exhibit low power densities due to their intrinsically low Li-ion transport capabilities.^[21] A promising alternative power source for stretchable electronics is an aqueous rechargeable lithium-ion battery (ARLB); these are based on highly safe aqueous electrolytes that have high Li-ionic conductivity (in relation to their power density).^[22]

In this article, we report on a bio-inspired Jabuticaba-like hybrid carbon/polymer (HCP) composite that was developed into a stretchable current collector using a simple and cost-effective solution process. The HCP composite was found to have greater electrical conductivity than composites containing single fillers, even at strain of 200%. We also found that it had exceptional stretching durability and mechanical robustness (which were determined using 1000 stretching/releasing cycles at 200% strain). In order to elucidate the in-depth electrical percolation mechanism of the HCP when it was subjected to strain, we used an in situ SAXS technique; SAXS is a highly useful technique for measuring the behavior of nanofillers in polymer matrices.^[23] Our results clearly demonstrated how the change in orientations and interconnected network of the fillers can affect to the electrical pathways under strain. In order to confirm the suitability of the polymer composite for use as a stretchable electrode in practical applications, we utilized them along with a stretchable ARLB in a deformable electronic device. The battery exhibited high electrochemical performance (a capacity loss of only 7% was found after 500 cycles at a rate of 20 C), and it delivered stable power to the device even at 100% strain. Our findings are expected to expand the number of stretchable nanocomposites with electrochemical and mechanical properties available for use in a wide variety of applications.

3.2 Experimental

Fabrication of stretchable electrode

Multiwalled carbon nanotubes (110 mg, MWCNTs, Sigma Aldrich) with diameter of 110~170 nm and length of 5~9 μm and super P carbon black (110 mg, Imerys S.A., France) with diameter of 50~60 nm was dispersed in hexane (5 mL, Sigma Aldrich) by ultra-sonication process for 2 h. And then, the dispersed composite solution was homogeneously mixed with ecoflex base (1g, Ecoflex 00-10, Smooth-On) using a vortex mixer for 10 min. Subsequently, the ecoflex curing agent (1:10 ratio for curing agent to base) was added to the composite solution. Simultaneously, it poured into a glass petri-dish (diameter 60 mm) and was transferred in a humidity chamber (from 60% to 100% humidity at room temperature) to construct porous structure onto the surface via breath figure process. The composite was thermally cured in an oven at 80 $^{\circ}\text{C}$ for 2 h. Finally, the fabricated composite has a thickness of 200 μm .

Synthesis of active materials

We synthesized polyimide coated activated carbon (PI@AC) as anode materials for aqueous lithium-ion battery. Firstly, 1,4,5,8-naphthalenetetracarboxylic dianhydride (1 mmol, Sigma Aldrich) and AC (0.2 g, product) were mixed with 4-chlorophenol (20 g, Sigma Aldrich) at 60 $^{\circ}\text{C}$. After then, ethylenediamine (0.15 mL, Sigma Aldrich) was added to the mixture and followed by refluxing at 220 $^{\circ}\text{C}$ for 10 h. The mixture was cooled to room temperature and the product was rinsed with ethanol and deionized water, and followed by vacuum filtration. The obtained powder was annealed at 320 $^{\circ}\text{C}$ under argon atmosphere for 4 h. To synthesize of LMO@CNT as cathode material, we firstly synthesized MnO_2 @CNT. In a typical synthetic process, 100 mg of CNT (Hanwha Nanotech Corp, Korea) and a certain amount of KMnO_4 (250 mg, Sigma Aldrich) were mixed together in an agate mortar. The mixed powder was poured into 100 mL of water and stirring for 10 min. 0.5 mL of concentrated H_2SO_4 (95%, Samchun) was added to the above solution with an additional stirring of 30 min. Then, the mixture was heated in an oil bath at 80 $^{\circ}\text{C}$ for 2 h. The precipitate was collected by filtration and washed repeatedly with deionized water after the mixture was cooled to room temperature. The product was dried in a vacuum oven at 60 $^{\circ}\text{C}$ for 12 h to obtain CNT@ MnO_2 composite. To make LiMn_2O_4 @CNT nanocomposites, 0.25 g of the MnO_2 @CNT nanocomposites and 0.26 g of $\text{LiOH}\cdot\text{H}_2\text{O}$ (Sigma Aldrich) were mixed with 60 mL of H_2O . And then, the mixture was uniformly mixed for 1 h before transferring into 80 mL autoclave. After the hydrothermal treatment at 160 $^{\circ}\text{C}$ for 12 h, the resulting precipitates were filtered and washed with distilled water. After the autoclave was cooled to room temperature, the

final product was dried in a ventilation oven at 60 °C for 12 h.

Characterization

Microstructure of LMO@CNT was investigated using X-ray diffractometer (XRD, Bruker D8-Advance), which was performed at 3 kW using Cu K α radiation. Transmission electron microscopy (TEM) images of conductive fillers and active materials were obtained using JEM 2100 (JEOL) operated at an accelerated voltage of 200 kV. The morphologies of nanocomposite and active materials were investigated using a field-emission scanning electron microscopy (FE-SEM, Hitachi S-4800). The FT-IR spectra of PI@AC was investigated using a Varian 670 IR spectrometer. The TGA analysis of LMO@CNT was investigated using TA-Q500 under air atmosphere. The mechanical properties were measured using a tensile strength measurement (DA-01, Petrol, Korea). The tensile strength samples were cut with the dog bone shape. The sheet resistance was conducted using a four-point probe machine (FPP-RS8, Dasol Eng., Korea). To measure electrical resistance of carbon/composite under strain using home-made strain equipment, it was attached to conductive fabric using silver paste to reduce contact resistance. The change of R value at stretching state was measured using multi meter in the strain ranging from 0 to 200%

In-situ SAXS analysis

SAXS measurements were performed at the 6D UNIST-PAL beamline of the Pohang Accelerator Laboratory in Korea. The energy of the X-rays was 11.6 keV (wavelength, $\lambda = 1.0688$ Å) and the sample-to-detector distance was 3510 mm. Scattering patterns were collected using a 2D CCD detector (MX225-HS, Rayonix L.L.C., USA). The samples were left perpendicular to the beam direction and elongated in the vertical direction at a constant stretching rate of 20 $\mu\text{m/s}$. The scattered intensity was obtained in the strain range from 0 to 200%.

Electrochemical test

The stretchable electrode, which was composed of active materials (LMO@CNT and PI@AC), conductive carbon (super P), and polymeric binder (PVDF) in a weight ratio of 8:1:1, was fabricated by spray coating method on hot plate at 150 °C. To remove residual solvent, the electrode was placed in vacuum oven at 150 °C for 10 h. And then it was pressed by rolling press machine at 20 MPa. The active loading density was 0.5 mg cm⁻². The electrodes were cut in the form rectangular shape (2 cm x 1 cm). The electrochemical properties of half and full cell were investigated using an electrochemical tester (Biologic science instrument, VSP) with a 1 M Li₂SO₄ aqueous electrolyte. Both three-electrode system and stretchable full cell were assembled in open environment. Pt electrode and Ag/AgCl electrode were used as the counter and reference electrode, respectively. The full cell was performed between 0.00 and 2.00 V at room temperature

and measured using two-electrode system with LMO@CNT and PI@AC as working electrode and counter electrode, respectively. The mass ratio of cathode and anode materials was designed as 1:1.3.

3.3 Results and discussion

One of the key challenges for stretchable power sources is for their energy densities to be improved; this parameter is strongly related to their surface areas, as upon these active materials can be loaded. Various studies have been conducted to solve this issue, and have resulted in structures such as porous frameworks being developed.^[24] Many of the proposed solutions, however, are not easy to produce at large scales due to the complicated multi-step procedures that their production processes require. In this study, we utilized a breath figure (BF) process to fabricate a porous structure and improve a power source's energy density.^[25] Figure 1a illustrates the process for the fabrication of the HCP composite that contained both CNT (10 wt% relative to the elastomer) and carbon black (CB, 10 wt% relative to the elastomer); for this fabrication process, a simple and cost-effective solution process was used. The morphologies of the CNT and CB were determined using transmission electron microscopy (TEM) (Figure S1, Supporting Information).

Initially, the hybrid carbon fillers were dispersed in hexane before being homogeneously mixed with an ecoflex matrix. An ecoflex curing agent was then added to the hybrid filler mixed solution, which was subsequently poured into a petri-dish. At the same time, the solution was transferred to humidity chamber so that a porous structure could be constructed on the surface of the device via the BF process. In the final step of the process, the obtained polymer composite was thermally cured in an oven. More details about the experimental process can be found in the Experimental Section. The surface morphology of the HCP composite fabricated by the BF method was observed using a scanning electron microscopy (SEM). As can be seen from the SEM images in Figure 1b, the porous structures appeared to form evenly on the surface of the HCP composite films. A high-magnification SEM image, meanwhile, revealed that the hybrid carbon had blended homogeneously with the polymer, which led to the high electrical percolation of the HCP composite (Figure 1c). We measured how the size of the pores on the surface varied as a function of the humidity (Figures 1d and S2), and we found that they increased gradually from 39 μm (at 60% humidity) to 130 μm (at 100% humidity); this occurred because many water droplets in the air condensed and were absorbed by the uncured polymer composite at higher humidity levels.^[26,27] Inset of Figure 1d shows the relative surface area of the HCP composite, which was calculated in terms of the size of its pores (Figure S3). The relative surface area of the composite increased approximately by a factor of four when the humidity was 100%. As a result, we believe that this increased surface area allowed for the amount of active loading to increase, which in turn improved the energy density of the device. To further investigate the morphologies of the hybrid

carbon in the polymer composite, we obtained TEM images of CB and the CNT. A mixture of 5 wt% CB and 10 wt% CNT fillers (based on their elastomer weights) was found to produce a self-assembled structure (Figure 1f) in which the CB nanoparticles adhered to the surface of the CNT (inset of Figure 1f). The shape of this structure resembled that of a Jabuticaba tree (Figure 1e). Composites in which the same amounts of the two conductive fillers were used (i.e., 10 wt% CNT and 10 wt% CB) were found to suffer from the additional CB nanoparticles aggregating and filling the empty space between the CNT (Figure 1g).

In order to demonstrate the robustness of the HCP composite, we carried out various physical deformation tests such as bending, twisting (Figure S4), and stretching (Figure 2a). Our results showed that the HCP composite was durable to extreme mechanical deformations due to the mixture of the conductive fillers with the highly elastic polymer matrix. Figures 2b–f show the electrical and mechanical characterizations of the HCP composite; crucially, it can be seen that the composite maintained its electrical conductivity even when highly deformed. Figure S5 shows the sheet resistance of the carbon/polymer composite as a function of the weight fractions of CB and CNT. This result shows that the sheet resistance of the polymer composite decreased as the amount of conductive fillers increased. However, it was found that when the total amount of filler exceeded 20 wt%, the polymer composite did not form properly, as indicated by the surface cracks that can be seen in Figure S6. To further demonstrate the elongation effect of polymer composite on the amount of filler, we conducted tensile strength test (Figure S7). As a result, we determined that the optimum amount of carbon filler was 20 wt%. We investigated the sheet resistance of the polymer composites when it contained the same total amount of filler but with different amounts of the constituents (i.e., one where it contained CNT 20 wt%, one where it contained CB 20 wt%, and a third that was a hybrid that contained 10 wt% of each) using a four-point probe measurement (Figure 2b). We found that the electrical conductivity of the polymer composite made purely out of CB was about 15 times higher than that of the polymer composite made purely out of CNT; this was because the loading volume of CB is much larger than that of CNT in the polymer matrix at the same weight percent (Figure S8).^[28] Interestingly, the sheet resistance of the HCP composite was similar to that of the CB/polymer composite. This was likely because the CB clusters improved the electrical conductivity of the hybrid material by reducing the tunneling distance and decreasing the contact resistance between the CNT junctions in the polymer matrix.^[29]

In order to further evaluate the electrical properties of the polymer composites under strain conditions, the normalized resistance, R/R_0 , of the composites was measured at various different strains; in this fraction, R_0 is the resistance of a composite when no strain is applied, and R is the resistance of a composite when measured under various strains (Figure 2c). Upon applying a strain of 200%, we found that the normalized resistances of the CNT/polymer, CB/polymer, and HCP

composites were 6.2, 4.2, and 1.4, respectively. The normalized resistances of both the CNT/polymer and CB/polymer composites rapidly increased up to a strain of 40% (Inset of Figure 2c); this was because the number of interconnections between the fillers decreased due to the average spacing between the interconnections increasing. The HCP composite, however, was able to effectively maintain its percolation network, even at strains of 200%; this was because the CNT were aligned along the stretching direction, and CB maintained the interconnections between the CNT. We investigated the structural evolution of HCP composite under various strain using SEM analysis. This result shows that CNT with high aspect ratio were oriented along the stretching direction (Figure S9). We also tested the durability of the electrical conductivity of the HCP composite; even after 1000 loading–unloading cycles at strains of up to 200%, highly stable percolation of the composite was found, as can be seen in Figure 2d. Using the knowledge we obtained about the electrical properties of the HCP composite discussed thus far, we proposed a model for the electrical conductive paths of the HCP for when the composite is stretched along the strain direction (Figure S10).

In order to evaluate the mechanical properties of the HCP composite, we produced strain–stress curves for it for 1000 loading–unloading cycles under a strain of 200% (Figure 2e). The hysteresis curve almost returned to its original point after unloading, which indicated that the HCP composite completely reverted to its original size without being permanently deformed. The inset of Figure 2e shows the change in the tensile strength of the composite as a function of the number of strain cycles. During 1000 cycles, the tensile strength decreased slightly before stabilizing. This mechanical stability demonstrated the outstanding mechanical robustness and durability of the HCP composite. The electrical performance of our stretchable conductor was compared to that of other stretchable conductors that have previously been reported upon^[30–36]; we found that the HCP composite exhibited significantly better resistance retention under the high strain conditions of 50%–200% (Figure 2f).

The detailed structural evolutions of the CB/polymer, CNT/polymer, and HCP composites during their elongation processes were determined using in situ SAXS measurements in the transmittance mode (Figures 3 and 4). The composites were placed perpendicular to the beam direction and stretched vertically at a constant elongation rate of $20 \mu\text{m s}^{-1}$. The X-ray scattered intensity of the composites were obtained for strains of 0%–200%. The quantitative changes in the structural orientations and interactions of the carbon frameworks were examined using Hermans orientation parameters and Porod analysis. Before the elongation, 2D scattering patterns of the conductive fillers (CB, CNT, and hybrid carbon) of the composites were found to have isotropic structural orientations (Figure S11). As the strain increased, the 2D scattering patterns of the CNT/polymer and HCP composite became more stretched, which indicated that the CNT

and hybrid carbon in the polymer matrices were aligned along the strain direction. However, the 2D scattering pattern of CB/polymer composite remained isotropic even at 200% strain, which implied that CB was dispersed in the matrices without orientation.

The anisotropies of the carbon frameworks were analyzed using an angle-dependent intensity profile; the one-dimensional scattering intensities of the frameworks were integrated (Figures 3a and 3b) at each angle (0° – 359°), where θ is the azimuthal angle. In Figure 3b, the scattered intensities at each angle were integrated from $q = 0.00565$ – 0.1 \AA^{-1} (q is a scattering vector). The intensity blocked because of beam stop at $\theta = 125^{\circ}$ – 155° was estimated through extrapolation, and each integrated $I(q)$ value was normalized with its minimum value. As the strain increased, the scattering intensities of both the CNT/polymer and HCP composites became highly anisotropic; the CB/polymer composite, however, exhibited a weak angle-dependent intensity. As a result, we concluded that the CNT fillers were oriented along the stretching direction due to their high aspect ratio, while the CB clusters were less sensitive to the strain.

The alignment quality of the internal structures of the composites was quantified using Hermans orientation factor^[37-40] (Figure 3c). Hermans orientation factor, S , was calculated from for a range of 0 – 90° , as shown in Figure 3b. S is defined as:^[37]

$$S = \frac{3 \langle \cos^2\theta \rangle - 1}{2}, \text{ where } \langle \cos^2\theta \rangle = \frac{\sum_{\theta=0^{\circ}}^{90^{\circ}} I(\theta) \sin\theta \cos^2\theta}{\sum_{\theta=0^{\circ}}^{90^{\circ}} I(\theta) \sin\theta} \quad (1)$$

When S had a value of 1, -0.5 , or 0, the alignments of the carbon fillers were considered to be perfectly perpendicular, perfectly parallel, or isotropic to the strain direction, respectively.^[38] At 200% strain, S approached -0.07 and -0.06 in the CNT/polymer and HCP composites, respectively, whereas it was found to be -0.02 in the CB/polymer composite. This result indicated that the fillers were denser in the direction of the strain, especially in the composites containing the CNT. Because the CNT concentration of the HCP composite was only half that of the CNT/polymer composite, it was expected that the orientation factor of the HCP composite would decrease due to the small contribution of CB to the alignment. However, we found that the orientation factor of the HCP composite did not decrease, but rather remained close to that of the CNT/polymer composite. This result implies that the CB clusters in the HCP composite formed along the long axis of the CNT, while the CNT guided the direction of the cluster; this is consistent with the TEM images in Figure 1f.

The internal structures of the composites were found to influence the physical properties of the materials. A well-interconnected filler structure is essential for the composites having good electrical percolation properties. The microstructures of the interconnections were analyzed using

calculations of surface area per volume of the filler clusters. We investigated the changes in surface-to-volume ratio of scatters from the scattering intensity, which could be directly related with the change of interconnections of the fillers. Figure 4a shows the azimuthally averaged 1D scattering data and the scattering intensity was found to decay with q^{-4} in the high q range (Porod region, $q > 0.06 \text{ \AA}^{-1}$) in Figure 4b, which enabled us to carry out a Porod analysis^[41] (See Supporting Information for the Porod analysis). Through the Porod analysis, we obtained the surface area per volume of the fillers^[42] for all samples (Table S1) and its changes under strain are plotted in Figure 4c.

As strain increased, the surface-to-volume ratio of fillers increased in CB/polymer and CNT/polymer composites. In CB/polymer or CNT/polymer composites, fillers can be deformed under the strain; CB clusters and CNT networks can be collapsed when stretched, resulting the decrease of possible interconnections and increase of surface area. However, the HCP composite showed the opposite result of decreasing surface-to-volume ratio of fillers, which is explained as follows. First, the CNT framework strongly supports CB clusters formed along CNTs against deformation; thus, the filler structures cannot be easily deformed. Second, when strain is applied, the non-clustered CBs in the polymer matrix (Figure 1g) can bridge the gaps between the hybrid carbon clusters; therefore, the hybrid carbon clusters are rather being interconnected each other upon stretching ensuring good electrical pathways. A comprehensive structural evolution for each composite before and after stretching is illustrated in Figure 4e.

Additionally, 2D Porod analysis is available for anisotropic systems^[39] where fillers are aligned along the stretching direction such as CNT/polymer and HCP composites at 100% and 200% strain. The equatorial scattering for an anisotropic system provides information related to the internal structures projected in the cross-sectional plane (See Supporting Information for the 2D Porod analysis and Figure S12). Using the 2D Porod analysis, we obtained Porod length, L_p for anisotropic systems, plotted in Figure 4d. L_p represents the characteristic lateral size of the carbon frameworks projected on the cross-sectional planes perpendicular to the strain direction (Figure 4e and Table S2). Upon stretching, the L_p values of the CNT/polymer composite was found to be slightly decreased, which implies the decrease of number of interconnections. However, a significant increase of the L_p value was found in the HCP composite on the cross-sectional plane, which indicated that the number of interconnections increased as the strain increased. We also noted that the value of L_p obtained was surprisingly close to the average diameters of the CNT and hybrid fillers in the TEM images.

Generally, when strain is applied to a film, the carbon frameworks collapse, resulting the decrease of interconnections. As a result, the resistance in the direction parallel to the strain increases and the electrical conductivity decreases, as shown in Figure 2c. In the HCP composite,

however, the strain increased the number of interconnections in between the hybrid carbon clusters, as confirmed by the Porod analysis (Figures 4c and 4d); it also improved the degree of orientation of the CNT, thereby better guiding the CB clusters in the HCP composites (Figure 3c). Therefore, the HCP composite was able to maintain good electrical conductivity with an improved orientation quality and increased interconnections upon stretching.

In order to demonstrate its use in a stretchable energy device, the HCP composite was used as a current collector in a stretchable ARLB. For this purpose, a LiMn^2O^4 -decorated CNT (LMO@CNT) and a polyimide-coated activated carbon (PI@AC) were synthesized as cathode and anode materials, respectively. The synthesis process and characterization of the active materials are described in Figure S13. The LMO@CNT and PI@AC electrodes were prepared by spray coating of the active materials onto the HCP composite.

A half-cell test of the LMO@CNT and PI@AC electrodes was first conducted with 1 M of a Li_2SO_4 electrolyte in three different electrode systems that were composed of a reference electrode (Pt) and counter electrode (Ag/AgCl). In Figure S14, it can be seen that the cyclic voltammetry profiles of the LMO@CNT and PI@AC electrodes showed typical redox peaks at a scan rate of 2 mV s^{-1} ; this indicated that the proposed current collector was suitable for use in this system. Figures 5a and S15a show the galvanostatic electrochemical performance of the PI@AC anodes, and they were found to be 97, 87, and 74 mA h g^{-1} at rates of 20, 45, and 100 C, respectively. In addition, the cathode was found to exhibit specific capacities of 121, 117, and 100 mA h g^{-1} for current densities of 15, 35, and 60 C, respectively (as shown in Figures 5b and S15b). Even at 100 C, the capacity retention of the LMO@CNT cathode was 83%. The cycling tests for both the cathode and anode were conducted at a rate of 30 C, and the specific capacities of the cathode and anode were found to be 97% and 99%, respectively, after 200 cycles (Figure 5c). This result demonstrates the highly reversible and outstanding cycling performance of both cathode and anode.

We then fabricated a stretchable ARLB to determine its feasibility for use in real-world scenarios. Figure 5d shows a schematic illustration of the configuration of a stretchable ARLB (4 cm (in length) x 3 cm (in width) x 1 cm (in thickness)) that was composed of an LMO@CNT cathode, a PI@AC anode, ecoflex packaging materials, and aqueous electrolytes. The total thickness of the stretchable cell was around 1 cm. The inset of Figure 5e shows the galvanostatic charge–discharge profiles of the stretchable full ARLB when a 1 M Li_2SO_4 electrolyte was used for 0–2 V (vs. Ag/AgCl). The rate capability of the full cell was evaluated for current densities of 20, 45, and 60 C, and specific capacities of 89, 76, and 65 mA h g^{-1} , respectively, were obtained. Figure S16 presents a constant current Ragone plot, plotted in Wh/kg and W/kg of total device weight. As a result, our batteries exhibit a maximum energy of about 30 Wh/kg and can deliver a

maximum power of 1260 W/kg. Figure 5f shows the cycling performance of the full ARLB at a rate of 20 C; the full cell exhibited a highly stable discharge capacity of 89 mA h g⁻¹, which meant that it had an excellent capacity retention of 93% after 500 cycles.

In order to further investigate the electrochemical performance of the full ALRB under strain, we conducted a cycling test at 20 C under strains of 0%–100% (Figure 5g). The stretchable full battery exhibited an excellent capacity retention of 80% at a strain of 100%. Notably, the normalized capacity returned to its original value after the strain was reduced to 0%. This indicated that the stretchable ARLB could accommodate the applied mechanical strain without having its electrochemical performance permanently impaired. To further investigate the stability of active materials on the HCP composite under mechanical stress, we measured SEM and the mass of electrodes as shown in Figure S18 and S19. Figure 5h shows that the stretchable ARLB was able to successfully operate a red light-emitting diode (LED) at various amounts of stretching; the battery continuously operated the LED under a ~100% strain, which indicated that it could deliver power even under extreme external stress (Movie S1).

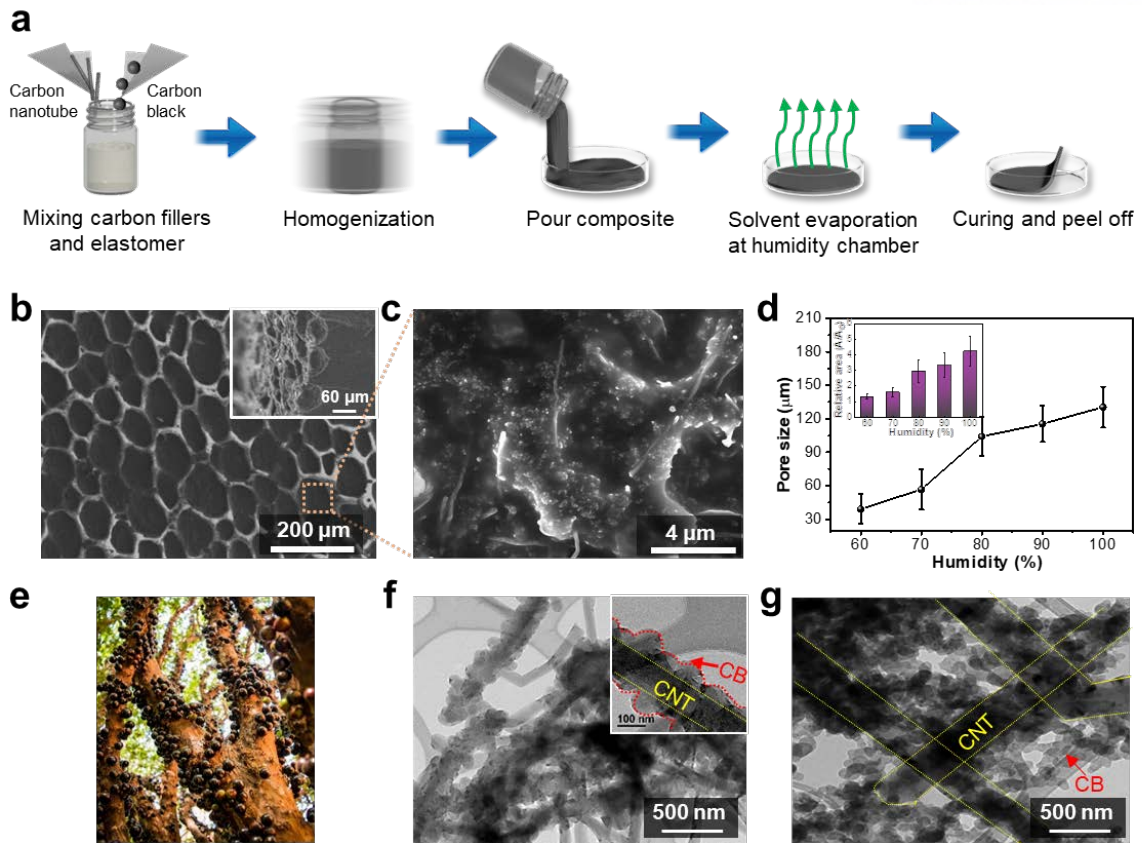


Figure 3-1. Steps for the fabrication and morphological characterization of the carbon/polymer composite. a) Schematic showing the sequences in the overall fabrication process. b) SEM image showing the surface morphology of the HCP composite. The inset shows a cross-sectional SEM image. c) High-magnification SEM image of the HCP composite showing hybrid carbon in the polymer matrix. d) Variation of the surface pore size of ecoflex as a function of humidity in the breath figure method. The inset shows the relative surface area as a function of humidity. e) Photograph of a Jabuticaba tree, which has a similar shape to that of the percolating network of the hybrid carbon. TEM images of the HCP composite with different weight ratios of f) CB:CNT = 1:2 and g) CB:CNT = 1:1.

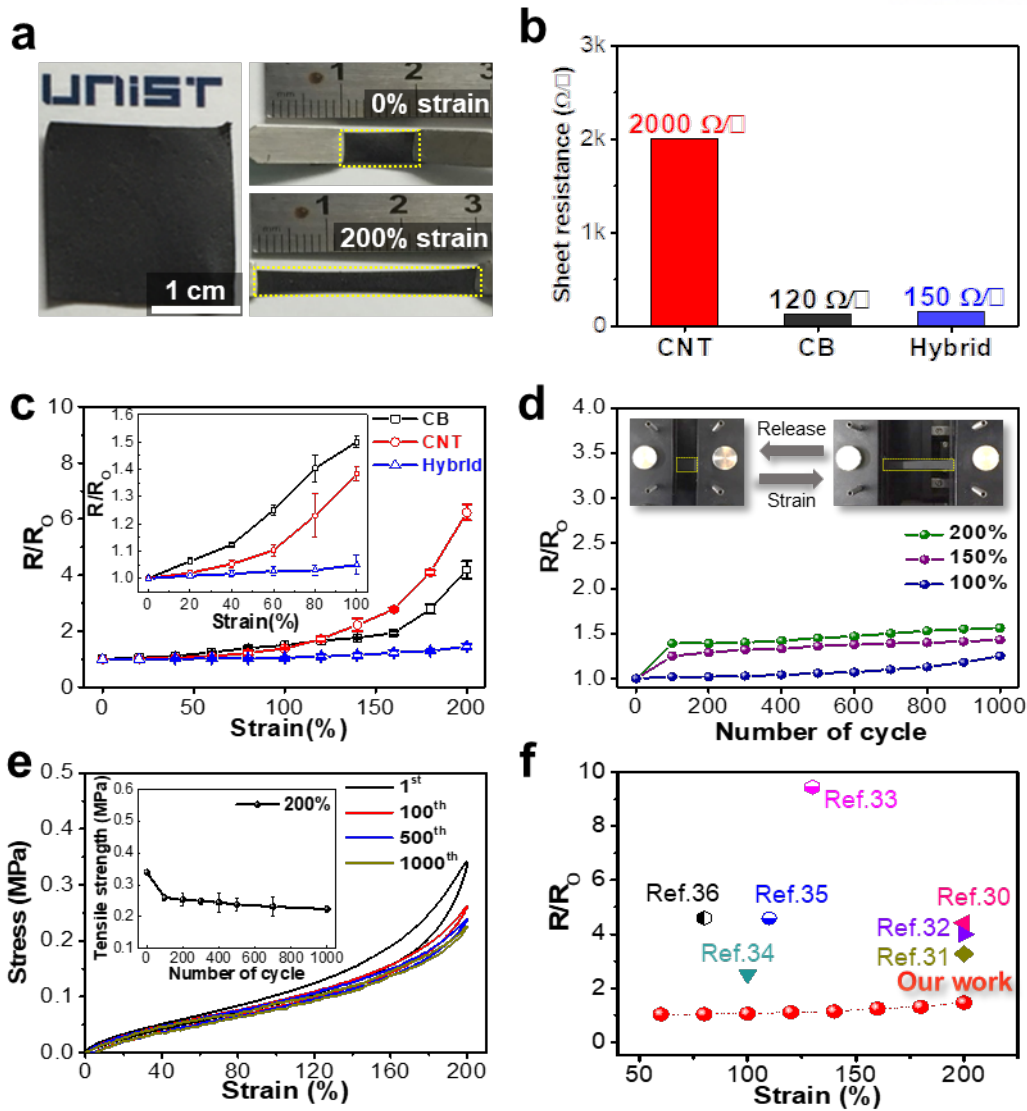


Figure 3-2. Characterization of the carbon/polymer composite. a) Photograph showing the three proposed composite films under stretching. b) Sheet resistance of the CNT/polymer, CB/polymer, and HCP composites, each of which has carbon contents of 20 wt% relative to polymer. c) Normalized sheet resistance (R/R_0) of each composite film for different amounts of strain. d) Normalized resistance of the HCP composite under strain of 100%, 150%, and 200% that were repeated for 1000 cycles. e) Fatigue test of the stretchable electrode containing the HCP composite under a strain of 200% that was repeated for 1000 cycles. The inset shows the tensile strength of the electrode as a function of the number of strain cycles, with the maximum value being 1000 cycles. f) Comparison of the normalized resistance (R/R_0) and strain performance of the HCP-containing stretchable conductor with other stretchable conductors.

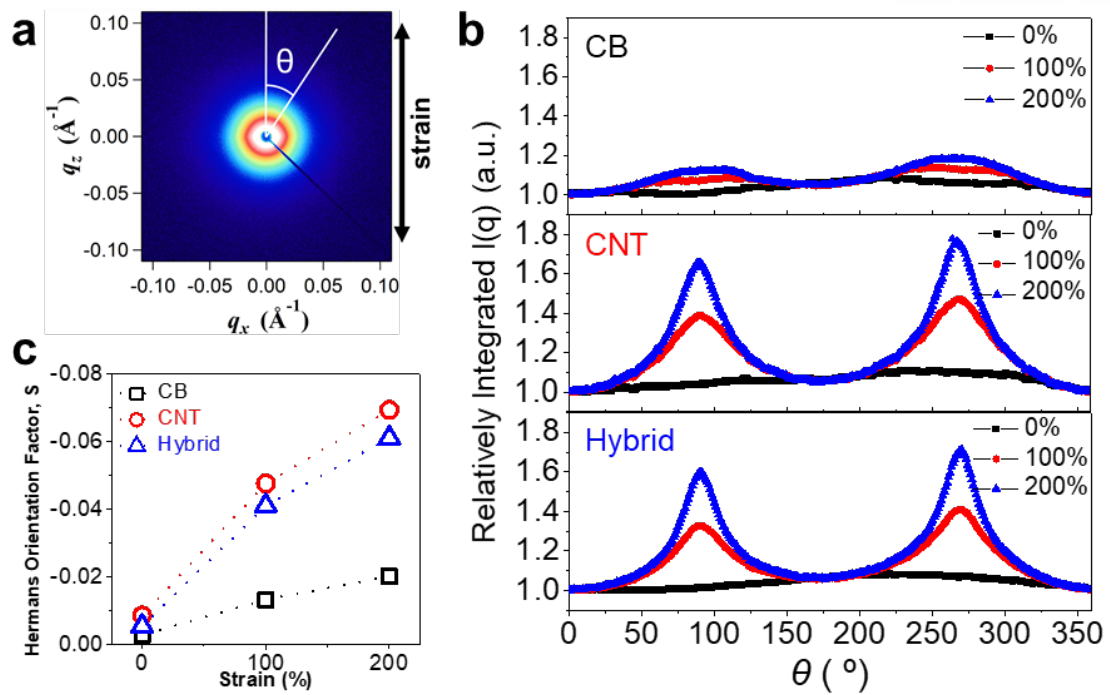


Figure 3-3. Structural orientation of carbon fillers. a) 2D SAXS data of the CNT/polymer composite at 200% strain. θ is the azimuthal angle from the strain direction. b) Integrated intensity from $q = 0.00565$ – 0.1 \AA^{-1} at each azimuthal angle. c) Calculated Hermans orientation factor, S .

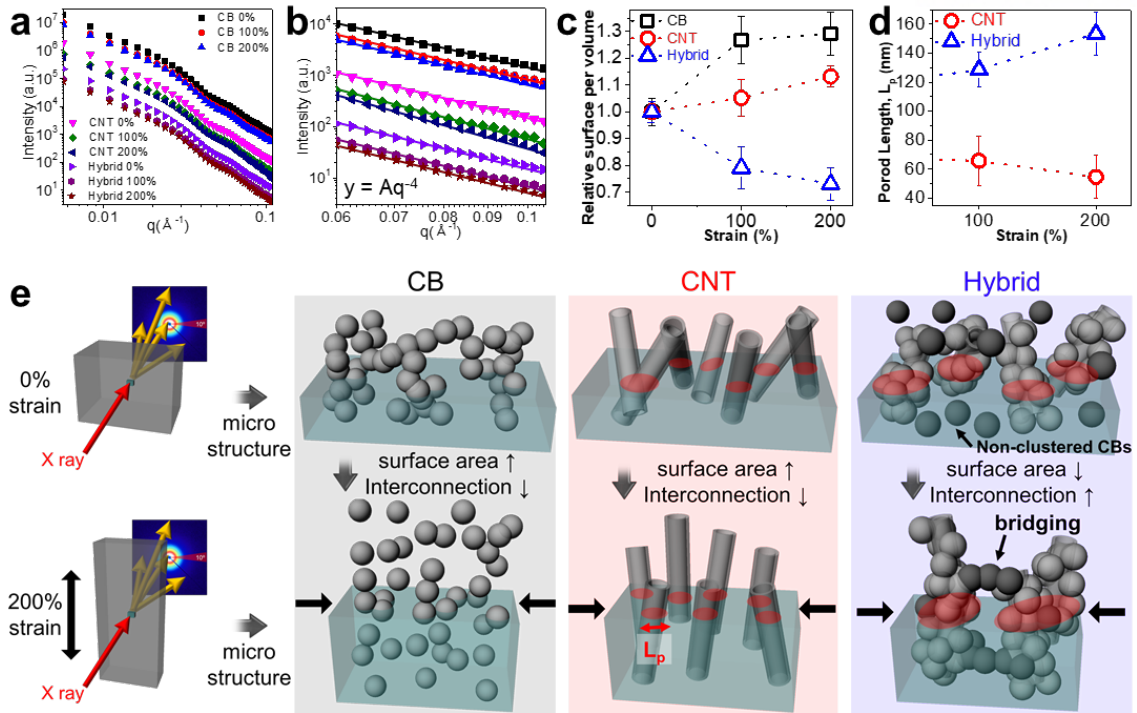


Figure 3-4. Interconnections within the carbon framework. a) 1D SAXS data and b) those fitted with q^{-4} from $q = 0.06\text{--}0.12 \text{ \AA}^{-1}$. The overlaid plots were distinguished by multiplying the plots of CB by 10 and the plots of the HCP by 0.1. c) Plot of relative changes in the surface area per volume, as determined by the Porod analysis. d) Plot of the calculated Porod length, L_p , for anisotropic systems, as determined by the 2D Porod analysis. e) Schematic showing the comprehensive structural development of the CB/polymer, CNT/polymer, and HCP composites under strain.

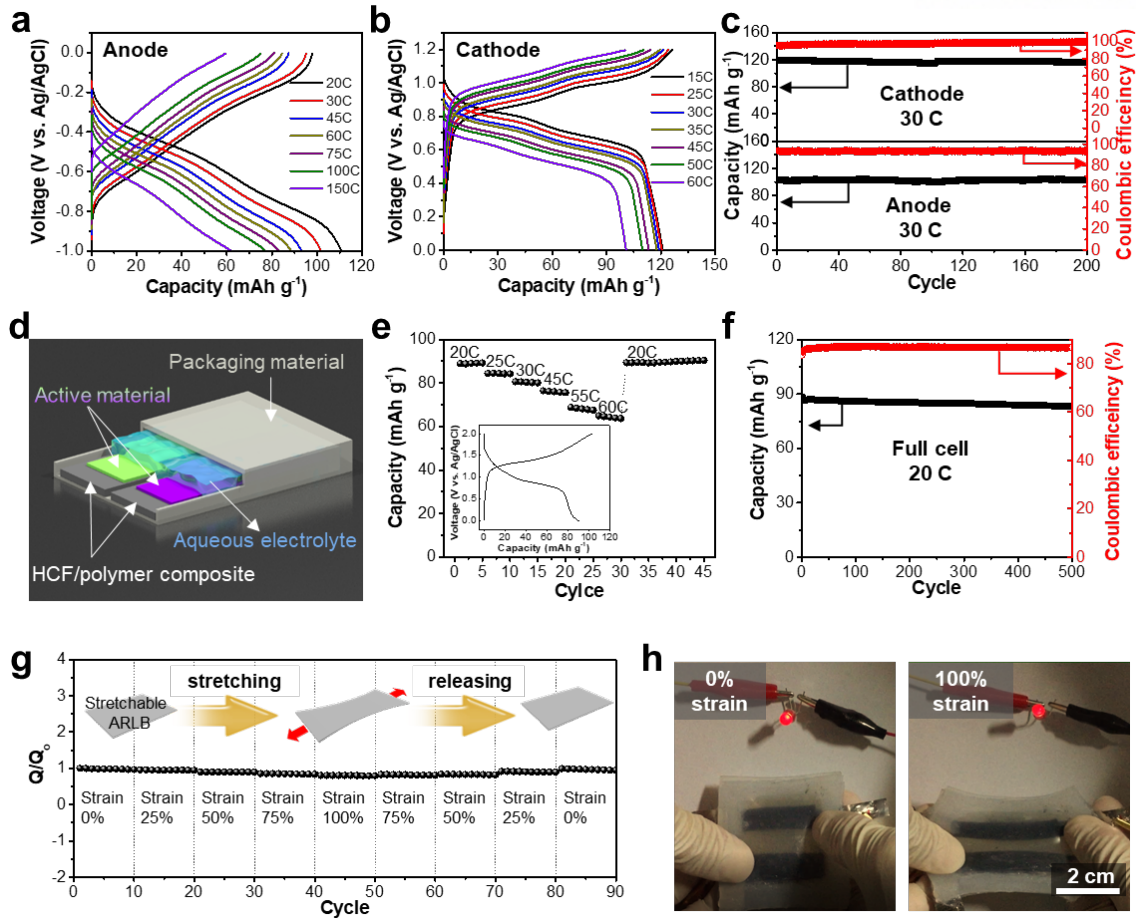


Figure 3-5. Stretchable aqueous batteries in which the HCP composite was used as a current collector. Galvanostatic charge–discharge curves at various C-rates for the a) PI@AC anode (–1.0–0 V) and b) LMO@CNT cathode (0–1.2 V). c) Cycling performance of the anode and cathode at a rate of 30 C over 200 cycles. d) Schematic showing a stretchable aqueous full cell configuration. e) Rate capability of the full cell (PI@AC//LMO@CNT) for 20–60 C. The inset shows the galvanostatic charge–discharge profiles of the full cell at a rate of 20 C. f) Long-term cycle performance and coulombic efficiency of the full cell at a rate of 20 C over 500 cycles. g) The relative discharge capacity of the stretchable ARLB under various amounts of strain. h) Photograph of a LED bulb operated by the stretchable ARLB in both its unstretched state and when 100% strain is applied.

3.4 Conclusion


We fabricated a bio-inspired Jaboticaba-like stretchable carbon filler/polymer composite via a simple solution process. The polymer/carbon composite exhibited excellent electrical properties and mechanical durability under strain. A detailed analysis of the percolation behaviors of the conductive filler within the composite was done using an in situ SAXS measurement under stretching, which revealed that the different types of carbon in the filler led to a formation of highly interconnected co-supporting networks. Using the polymer composite as a stretchable current collector, we have, for the first time, developed stretchable ARLB as a stretchable power source, and they delivered stable power to a LED even under 100% strain. This study is expected to facilitate the design of stretchable nanocomposites with optimized electrochemical and mechanical properties for use in energy storage devices and stretchable electronics.

3.5 Reference

- [1] J. A. Rogers, T. Someya, Y. G. Huang, *Science* **2010**, 327, 1603.
- [2] J. A. Rogers, Y. Huang, *Proc. Natl. Acad. Sci. USA* **2009**, 106, 10875.
- [3] D.-H. Kim, J. Song, W. M. Choi, H.-S. Kim, R.-H. Kim, Z. Liu, Y. Y. Huang, K.-C. Hwang, Y.-W. Zhang, J. A. Rogers, *Proc. Natl. Acad. Sci. USA* **2008**, 105, 18675.
- [4] D. H. Kim, J. A. Rogers, *Adv. Mater.* **2008**, 20, 4887.
- [5] N. Matsuhisa, M. Kaltenbrunner, T. Yokota, H. Jinno, K. Kuribara, T. Sekitani, T. Someya, *Nat. Commun.* **2015**, 6, 7461
- [6] K. Xie, B. Wei, *Adv. Mater.* **2014**, 26, 3592.
- [7] W. Liu, M. S. Song, B. Kong, Y. Cui, *Adv. Mater.* **2016**, 29, 1603436.
- [8] L. Hu, M. Pasta, F. La Mantia, L. Cui, S. Jeong, H. D. Deshazer, J. W. Choi, S. M. Han, Y. Cui, *Nano Lett.* **2010**, 10, 708.
- [9] C. Yu, C. Masarapu, J. Rong, B. Wei, H. Jiang, *Adv. Mater.* **2009**, 21, 4793.
- [10] S. Xu, Y. Zhang, J. Cho, J. Lee, X. Huang, L. Jia, J. A. Fan, Y. Su, J. Su, H. Zhang, *Nat. Commun.* **2013**, 4, 1543.
- [11] W. Liu, Z. Chen, G. Zhou, Y. Sun, H. R. Lee, C. Liu, H. Yao, Z. Bao, Y. Cui, *Adv. Mater.* **2016**, 28, 3578.
- [12] R. Sengupta, M. Bhattacharya, S. Bandyopadhyay, A. K. Bhowmick, *Prog. Polym. Sci.* **2011**, 36, 638.
- [13] W. Bauhofer, J. Z. Kovacs, *Compos. Sci. Technol.* **2009**, 69, 1486.
- [14] Z. Spitalsky, D. Tasis, K. Papagelis, C. Galiotis, *Prog. Polym. Sci.* **2010**, 35, 357.
- [15] K.-Y. Chun, Y. Oh, J. Rho, J.-H. Ahn, Y.-J. Kim, H. R. Choi, S. Baik, *Nat. Nanotechnol.* **2010**, 5, 853.
- [16] A. V. Kyrlyuk, M. C. Hermant, T. Schilling, B. Klumperman, C. E. Koning, P. Van der Schoot, *Nat. Nanotechnol.* **2011**, 6, 364.
- [17] C. Tang, G. Long, X. Hu, K.-w. Wong, W.-m. Lau, M. Fan, J. Mei, T. Xu, B. Wang, D. Hui, *Nanoscale* **2014**, 6, 7877.
- [18] S. Choi, J. Kim, D. Y. Hwang, H. Park, J. Ryu, S. K. Kwak, S. Park, *Nano Lett.* **2016**, 16, 1179.
- [19] W.-J. Song, S. H. Joo, D. H. Kim, C. Hwang, G. Y. Jung, S. Bae, Y. Son, J. Cho, H.-K. Song, S. K. Kwak, *Nano Energy* **2017**, 32, 255.
- [20] W. Li, J. R. Dahn, D. S. Wainwright, *Science* **1994**, 264, 1115.

- [21] H. Kim, J. Hong, K.-Y. Park, H. Kim, S.-W. Kim, K. Kang, *Chem. Rev.* **2014**, *114*, 11788.
- [22] C. Grey, J. Tarascon, *Nat. Mater.* **2017**, *16*, 45.
- [23] F. Du, J. E. Fischer, K. I. Winey, *Phys. Rev. B* **2005**, *72*, 121404.
- [24] Y. Sun, J. Lopez, H. W. Lee, N. Liu, G. Zheng, C. L. Wu, J. Sun, W. Liu, J. W. Chung, Z. Bao, *Adv. Mater.* **2016**, *28*, 2455.
- [25] A. Zhang, H. Bai, L. Li, *Chem. Rev.* **2015**, *115*, 9801.
- [26] A. Böker, Y. Lin, K. Chiapperini, R. Horowitz, M. Thompson, V. Carreon, T. Xu, C. Abetz, H. Skaff, A. Dinsmore, *Nat. Mater.* **2004**, *3*, 302.
- [27] E. M. Pérez, N. Martín, *Chem. Soc. Rev.* **2015**, *44*, 6425.
- [28] Irina Dubnikova, Evgeniya Kuvardina, Vadim Krasheninnikov, Sergey Lomakin, Igor Tchmutin, Sergey Kuznetsov, *J. Appl. Polym. Sci.* **2010**, *117*, 259-272.
- [29] J. Sumfleth, X. C. Adroher, K. Schulte, *J. Mater. Sci.* **2009**, *44*, 3241.
- [30] Y. Wang, C. Zhu, R. Pfattner, H. Yan, L. Jin, S. Chen, F. Molina-Lopez, F. Lissel, J. Liu, N. I. Rabiah, *Sci. Adv.* **2017**, *3*, e1602076.
- [31] C. Choi, J. H. Kim, H. J. Sim, J. Di, R. H. Baughman, S. J. Kim, *Adv. Energy Mater.* **2017**, *7*.
- [32] T. S. Hansen, K. West, O. Hassager, N. B. Larsen, *Adv. Funct. Mater.* **2007**, *17*, 3069.
- [33] T. Sekitani, Y. Noguchi, K. Hata, T. Fukushima, T. Aida, T. Someya, *Science* **2008**, *321*, 1468.
- [34] M. Park, J. Im, M. Shin, Y. Min, J. Park, H. Cho, S. Park, M.-B. Shim, S. Jeon, D.-Y. Chung, *Nat. Nanotechnol.* **2012**, *7*, 803.
- [35] Y. Kim, J. Zhu, B. Yeom, M. Di Prima, X. Su, J.-G. Kim, S. J. Yoo, C. Uher, N. A. Kotov, *Nature* **2013**, *500*, 59.
- [36] F. Xu, Y. Zhu, *Adv. Mater.* **2012**, *24*, 5117.
- [37] W.-S. Tung, R. J. Composto, N. Clarke, K. I. Winey, *ACS Macro Lett.* **2015**, *4*, 916.
- [38] J. Kevin, K. G. Yager, T. Hoare, E. D. Cranston, *Langmuir* **2016**, *32*, 7564.
- [39] W. Wang, W. Ruland, Y. Cohen, *Acta Polym.* **1993**, *44*, 273.
- [40] K. J. Choi, J. E. Spruiell, J. L. White, *J. Polym. Sci., Part B: Polym. Phys.* **1982**, *20*, 27.
- [41] O. Glatter, O. Kratky, *Small angle X-ray scattering*, Academic press, New York. **1982**.
- [42] D. Vollet, D. Donatti, A. I. Ruiz, *J. Non-Cryst. Solids* **2002**, *306*, 11.

** Chapter III is reproduced in part with permission of “Woo-Jin Song, Jeonghwan Park, Dong Hyup Kim, Sohyun Bae, Myung-Jun Kwak, Myoungsoo Shin, Sungho Kim, Sungho Choi, Ji-Hyun Jang, Tae Joo Shin, So Youn Kim^{*}, Kwanyong Seo^{*}, and Soojin Park^{*}, Jabuticaba-inspired Hybrid Carbon Filler/Polymer Electrode for Use in Highly Stretchable Aqueous Li-ion Batteries, Advanced Energy Materials, 2018, 8, 1702478”. Copyright 2018 John Wiley & Sons, Inc.*



Chapter IV. Design of Janus-Faced Electrode for Highly Stretchable Zinc-Silver Rechargeable Batteries

4.1 Introduction

The development of stretchable energy devices is indispensable for realizing the next-generation wearable devices such as sensors, health care, and electronic skin^[1-3]. While there has been tremendous progress in the advance of wearable electronics, the study on stretchable power sources that can retain a large physical strain without failing the battery's performance is still in an infant state^[4, 5]. Various energy devices such as lithium-ion batteries (LIBs) and metal-air batteries have been considered as wearable power accessories. Among them, LIBs are a candidate due to their high energy density, long-term cycling performance. Despite these advantages, its application in wearable devices has been limited because LIBs based on a flammable organic electrolyte have remained a safety concern under repeated deformation^[6].

Zinc-based batteries, that feature a water-based chemistry including zinc-air, zinc-manganese dioxide (MnO₂), zinc-nickel and zinc-silver, have received much attention^[7-10]. This battery chemistry is of importance because the aqueous electrolyte is naturally safer and has high ionic conductivity (that is, fast charge/discharge) compared to the organic electrolyte^[11]. Among the zinc-based batteries, the zinc-silver batteries are the most mature batteries, because which have already been used in small devices and large-scale applications^[12]. For these reasons, the zinc-silver batteries are a plausible answer to the deformable power source for the wearable devices. Several approaches have been proposed for designing stretchable zinc-silver batteries, particularly using concepts of tattoo-based batteries, all-printed batteries, and cable-type batteries so far^[13-18]. Although these innovative approaches dedicated to fabricating stretchable power sources with high energy density and high stretchability, they do not simultaneously provide a long-term cyclability because of zinc dendrite formation under repeated plating and stripping during the cycles, which leads to poor lifetime^[19].

Normally, conventional batteries consist of a current collector, active materials, separator, and electrolyte. As a core component, a stretchable current collector poses a formidable obstacle to progress of the stretchable batteries owing to their trade-off relation between electrical conductivity and stretchability^[20]. Strain-engineered structures such as buckling, island interconnection, and origami structure have been widely attempted to fabricate stretchable current collectors; however, the complex manufacturing process has limited their practical applications.

Polymer nanocomposite where a conductive filler is embedded into an insulating polymeric matrix is a fascinating alternative for the fabrication method of stretchable current collectors to overcome the above issues^[21]. However, because the initially built percolation network of conductive fillers collapses under physical deformation, the electrical conductivity of the composite is highly strain-sensitive.

Here, we propose stretchable zinc-silver rechargeable batteries based on a Janus-faced electrode, comprising a cathode and an anode on the one electrode, are presented. In the Janus-faced electrode based on Ag/poly(styrene-*b*-butadiene-*b*-styrene) (SBS) polymer nanocomposite, a metallic zinc serves anode materials whilst silver nanoparticles exhibit bifunctional roles as cathode materials and conducting fillers as a current collector. This unique configuration guarantees long-term cyclability of zinc-silver batteries due to the suppression of zinc dendrite. Moreover, the Janus-faced electrode exhibits a mechanical robustness, as well as a stable electrical conductivity under a large strain. To substantiate the percolation behavior of Ag NPs embedded in the elastomer, we examine *in-situ* small angle X-ray scattering (SAXS) and dynamic simulation. Furthermore, proposed stretchable energy-device can tolerate a large strain and can deliver a stable electrochemical performance even under 200% strain whilst keeping its functional performance.

4.2 Experimental

Materials

Polystyrene-*block*-polybutadiene-*block*-polystyrene (SBS) block-copolymer with 30% styrene and toluene was obtained from Sigma-Aldrich. Silver trifluoroacetate (AgCooH) powder and hydrazine solution (35wt% ~) was purchased by Sigma-Aldrich. Ethanol () and chloroform () was obtained by Samchun Inc. Poly (dimethyl siloxane) (PDMS) was obtained by Sylgard.

Fabrication of stretchable electrode

In a typical experiment, 5g of SBS pellets was added to 23g of chloroform. This SBS solution was stirred vigorously for 2 hours. The solution was then dispensed on top of a silicon wafer, followed by spin coating the rotating speed ranging X rpm for 30 second under ambient conditions. The wafer with the spin-coated SBS film was transferred to vacuum oven to remove vapor in the film for 2h at the room temperature. The obtained film size was 2 cm (vertical) x 2 cm (perpendicular) x 90 μm (thickness). To fabricate silver nanoparticles (AgNPs)/SBS polymer composite, the SBS film was dipped in the silver precursor solution (15wt% AgCooH in ethanol) for 30 min, and then transferred to hydrazine solution to reduce silver ion to silver nano particles. We repeated these processes of swelling and reduction 6 times. When the dipping was 6 times, diffusion of AgNPs was about 30 μm , it showed that the thickness of SBS polymer was lower than 60 μm , causing internal short. As a result, we choose the 90 μm of thickness of SBS film.

Characterization of stretchable electrode

The structure of electrode and active materials was measured by field-emission scanning electron microscopy (FE-SEM, Hitachi S-4800). Thermogravimetric analysis (TGA, TA instruments, Q50) was conducted at a heating rate of 10 $^{\circ}\text{C}/\text{min}$ from 30 $^{\circ}\text{C}$ to 600 $^{\circ}\text{C}$ under air atmosphere and used to calculate the mass content of silver particles in the polymer. Transmission electron microscopy (TEM) images were taken in the bright-field mode by using a JEM 2100 (JEOL). The mechanical properties of the as-prepared electrode were cut in the form dog-bon shape and then were performed using a tensile strength machine (DA-01, Petrol LAB, Korea) at a constant stress rate. The sheet resistance of the electrode was examined through a four-point probe equipment (FPP-RS8, Dasol Eng., Korea).

Fabrication of stretchable zinc-silver batteries

The Janus-faced electrode was cut out into 3 cm (vertical) by 1 cm (horizontal) size. To prevent the exfoliation of active materials, 3 ml of SBS solution (1 wt% in toluene) was spray coated

using an airbrush (Infinity CRplus, Harder & Steenbeck, Germany) on the both sides of the electrode. The tips and center area of the electrode which act as tab and electrolyte contact region each was masked and the rest was spray coated with 10ml of SBS solution (4 wt% in toluene). After the electrode was spray coated with 4wt% SBS solution, the surface was fully covered with SBS block copolymers and became easy to be functionalized with O₂ plasma treatment. PDMS film was used for a packaging material of the battery. The designed size was 2.4 cm (vertical) × 2.2 cm (horizontal) × 420 μm (height). Thicker PDMS film (2.4 cm × 2.2 cm × 720 μm) with empty space center was used for a spacer and provided sufficient room for electrolyte injection. Both outer and inner PDMS film was treated with O₂ plasma (CUTE, Femto Science, Korea) for a minute at 100 W. After O₂ plasma process is finished, spacer and packaging PDMS were bonded together. An electrode region which fully covered with SBS block copolymers was treated with O₂ plasma and affixed to spacer PDMS. To operate the battery, gel electrolyte was carefully injected using syringe.

4.3 Results and discussion

Schematic illustration of the fabrication procedures of the Janus-faced electrode is depicted in **Fig. 1a**. Briefly, SBS film fabricated by spin coating was soaked in a silver precursor solution (15 wt%) and then directly converted the precursor into Ag NPs using hydrazine solution as reducing agent. Finally, a metallic zinc was electrodeposited onto on the one side of the Ag/SBS composite (opposite side was protected with polyimide (PI) tape). This composite is referred to as a Janus-faced electrode. **Fig. 1c** shows that the Janus-faced electrode, unlike a typical battery configuration that consists of two electrodes, is composed of a cathode and an anode on the one electrode. In the Janus-faced electrode, a metallic zinc serves anode materials whilst Ag NPs exhibit bifunctional roles as cathode materials (located on the surface, s-Ag NPs) and conducting fillers as a current collector (embedded in SBS polymer, e-Ag NPs).

To investigate structural characterizations of the Janus-faced electrode, we conducted scanning electron microscopy analysis. In **Fig. 1b**, The SEM images indicate that the particle size of s-Ag NPs is about 50 nm. On the opposite side, in **Fig. 1d**, metallic zinc micro-particles were deposited on the s-Ag NPs. A cross-sectional SEM and EDS mapping images demonstrate that the Janus-faced electrode was approximately 90 μm in thickness and clearly divided between cathode and anode from an SBS polymer layer (30 μm), verifying that there is no electrical flow between the electrodes (**Fig. 1e and f**). An enlarged view of the cross-SEM image in **Fig. 1g** exhibits that e-Ag NPs with diameters ranging from 20 to 70 nm was densely embedded within the SBS polymer matrix and forms into the self-assembled structure. Those e-Ag NPs guarantees effective electrical percolation network inside the polymer under strain, as discussed later in the next sections.

The electrical conductivity of Ag/SBS composite increases with the number of dipping cycles because this repetitive process increases the population of Ag NPs of the SBS film. From the thermogravimetric analysis (TGA) of the Ag/SBS composite, the amount of loading e-AgNPs in the SBS polymer was about 77 wt%. **Figure 2c** shows that no obvious differences are observed in electrical resistance during stretching from the initial strain of 0% to 240%. A thickness 30 μm gives rise to adequate connections in the absence of the external strain. The relation between the resistance and the strain also depends on the thickness of the Janus electrode. For thickness 90 μm , the changes in the relative resistance were not observed under strain. Inset of **Figure 2c** indicated that upon applying a strain of 200%, we found that the resistance value was 0.7 ohm. The electrode effectively retains its percolation network even under 200%. It demonstrates that the Janus electrode maintained the percolation network even at a strain of 200%.

We investigated in-depth the dynamics of Ag NPs in the polymer matrix using *in-situ* small

angle X-ray scattering (SAXS) analysis that is powerful tools for the understanding of percolation behavior of conductive filler under applied strain. **Fig. 3a** presents the evolution of change in two-dimensional (2D) SAXS patterns for bare SBS film and the Ag/SBS composite during stretching and releasing under a strain of 200%. The SBS film

At a strain of 0%, the patterns of Ag/SBS composite are isotropic scattering structure, indicating that the Ag NPs are randomly distributed in the polymer matrix. By stretching the sample to the strain of 200%, the pattern gradually changes the anisotropic scattering structure along perpendicular stretching direction during strain. This change in scattering patterns comes from e-Ag NPs because they have larger electron density than the SBS polymer, and reflects the alignment of these filler clusters along strain direction. As a result, upon stretching, aligned e-Ag NPs effectively preserve the electrical pathway. When releasing the strain of 0%, the SAXS patterns perfectly change to their original patterns.

Electrochemical property of the stretchable zinc-silver batteries was tested in aqueous electrolyte using a beaker cell with 1M KOH. The cyclic voltammetry (CV) test of the Janus-faced electrode exhibits as shown in **Fig. 4a**. The electrochemical performance of the zinc-silver full batteries operated at a voltage window between 1.2V and 1.8V and the corresponding charge-discharge profiles at different current densities of 0.5, 1, and 2 mA cm⁻² was presented in **Fig. 4b**. The full batteries had discharge and charge plateau at around 1.58V and 1.7V, respectively, which indicated typical zinc//silver reaction. In **Fig.4x**, cycling performance of the batteries showed a highly stable capacity of 1.1 mA h cm⁻², corresponding to an outstanding capacity retention of 88% for 200 cycles, suggesting that a unique architecture of the Janus-faced electrode (i.e., backslide-plating configuration) contributes to suppress internal short circuits. To gain additional insights into this concept, we conducted electrochemical plating-stripping cycles and performed SEM analysis of the surface of cathode side after cycling (**supporting information Fig. SX**).

To further evaluate electrochemical performance under strain, we designed stretchable zinc-silver batteries in which Janus-faced electrode was dip-coated in the gel polymer electrolyte and wrapped with poly(dimethylsiloxane) (PDMS) as packaging materials (**Fig. 4d**). Under various strain of 0%, 100%, and 200%, the cycling performance of the stretchable batteries was evaluated at a current density of 1 mA cm⁻² between 1.2 and 1.8V for 30 cycles (**Fig. 4e and f**). This increased areal capacity under strain is due to a new surface of the electrode exposed on electrolyte by stretching. The charge-discharge curves of stretchable batteries obviously indicated no change of voltage plateau even under 200%. The capacity was completely recovered to initial capacity value after releasing to 0% strain. Thus, these results clearly show that the stretchable batteries based on Janus-faced electrode exhibited stable electrical performance even at a strain of 200%.

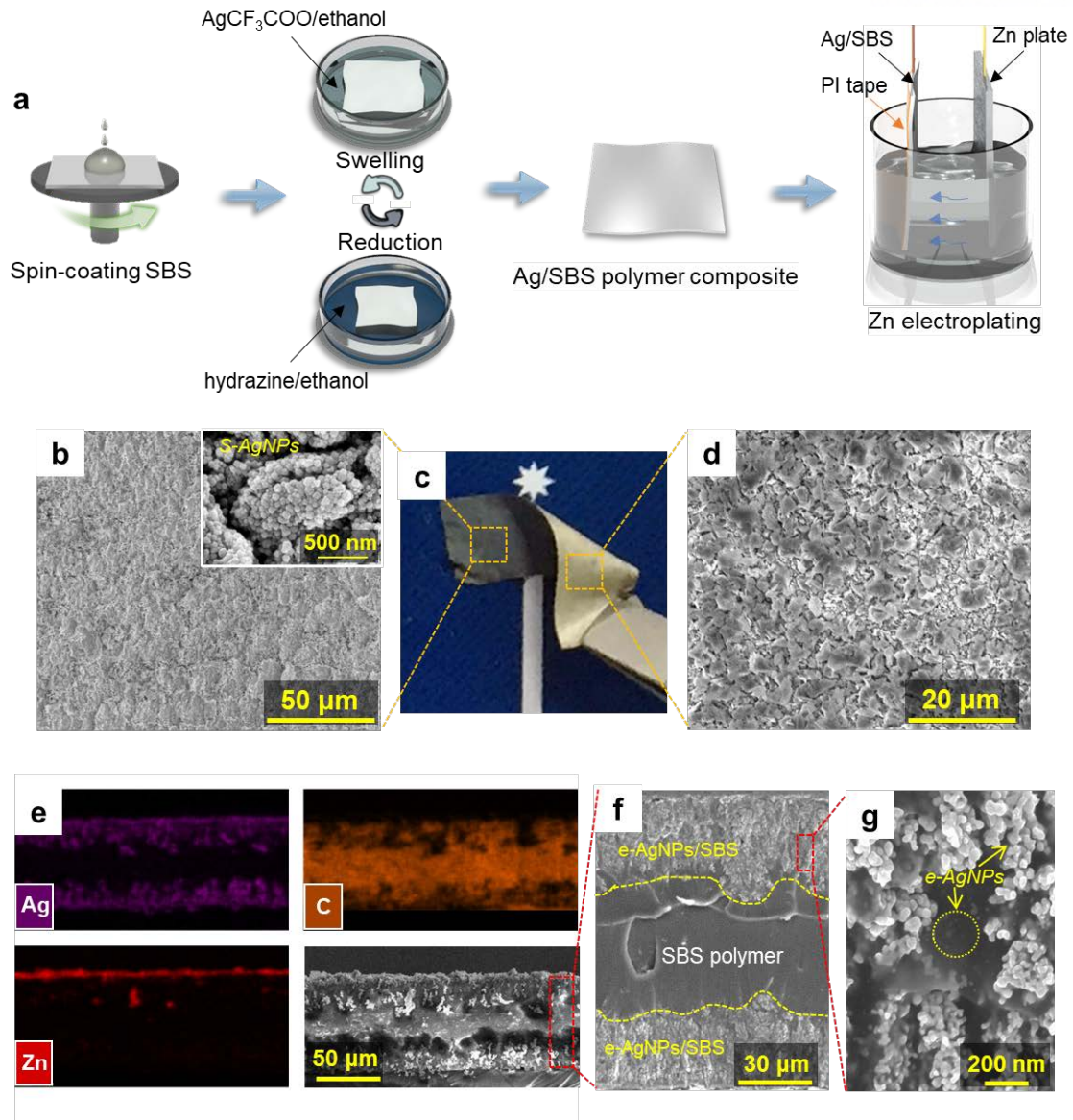


Figure 4-1 | Fabrication and characterization. **a**, Schematic illustration showing the fabrication process of Janus-faced electrode. **b**, Optical image of Janus-faced electrode. SEM images of **(c)** Ag/SBS composite electrodeposited with zinc (Zn, as anode) and **(d)** silver nanoparticles on surface of Ag/SBS composite (Ag, as cathode). **e-g**, EDS mapping and SEM images of cross-sectional SEM images showing Ag, C, and Zn element. **f**, cross-sectional SEM of Janus electrode. **g**, enlarged SEM view of Ag/SBS composite showing e-AgNPs and SBS polymer matrices

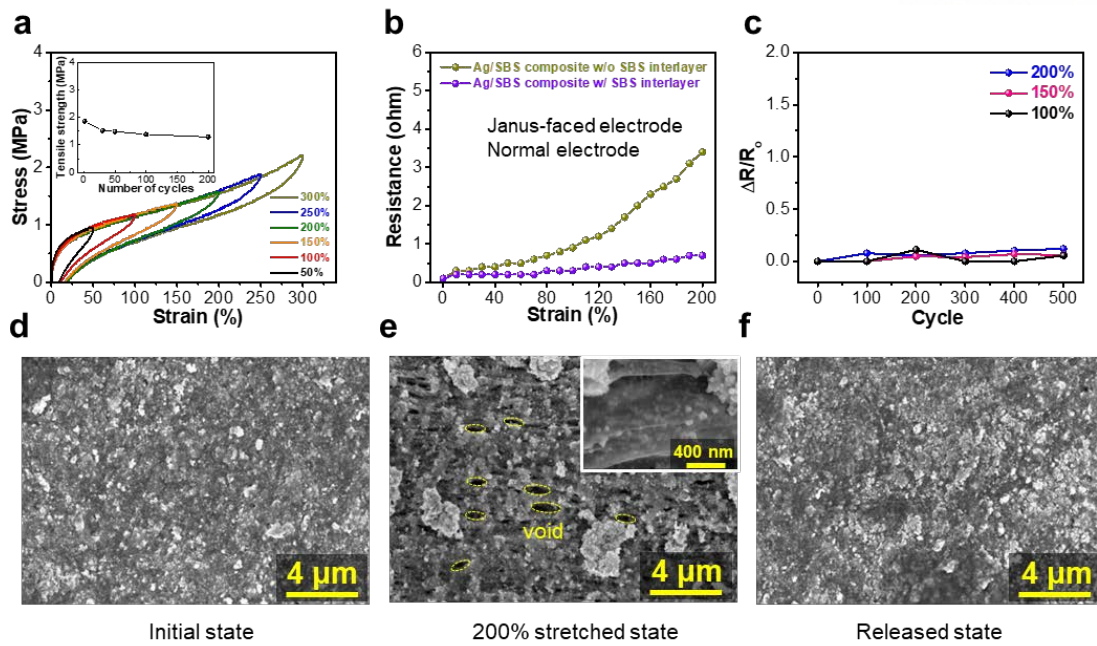


Figure 4-2 | Characterization of electrical conductivity and mechanical properties. a, Tensile strength measurement of the Janus electrode under various strain states. (inset) tensile strength at 200% strain as a function of stretching cycles. b, Change in resistance under strain of normal electrode and the Janus electrode. c, Recorded relative resistance of the Janus electrode during 500 cycles at a strain of 100%, 150% and 200%, respectively.

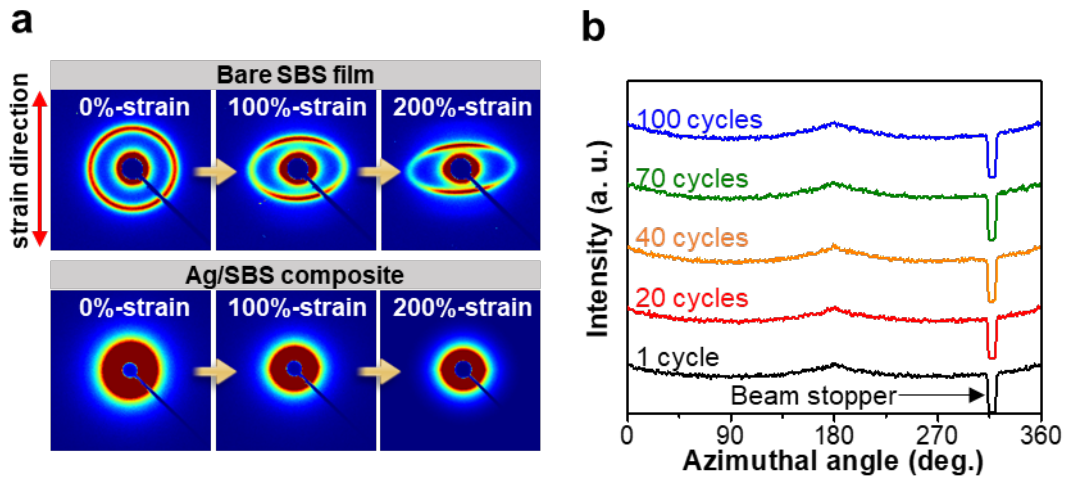


Figure 4-3 | Measurement of in-situ SAXS and dynamic simulation. a, 2D SAXS patterns of bare SBS film and Ag/SBS composite under 200% strain. Surface AgNP of Ag/SBS composite was removed by pressing type. b, Azimuthal angle of the Ag/SBS composite at 200% strain during 100 cycles.

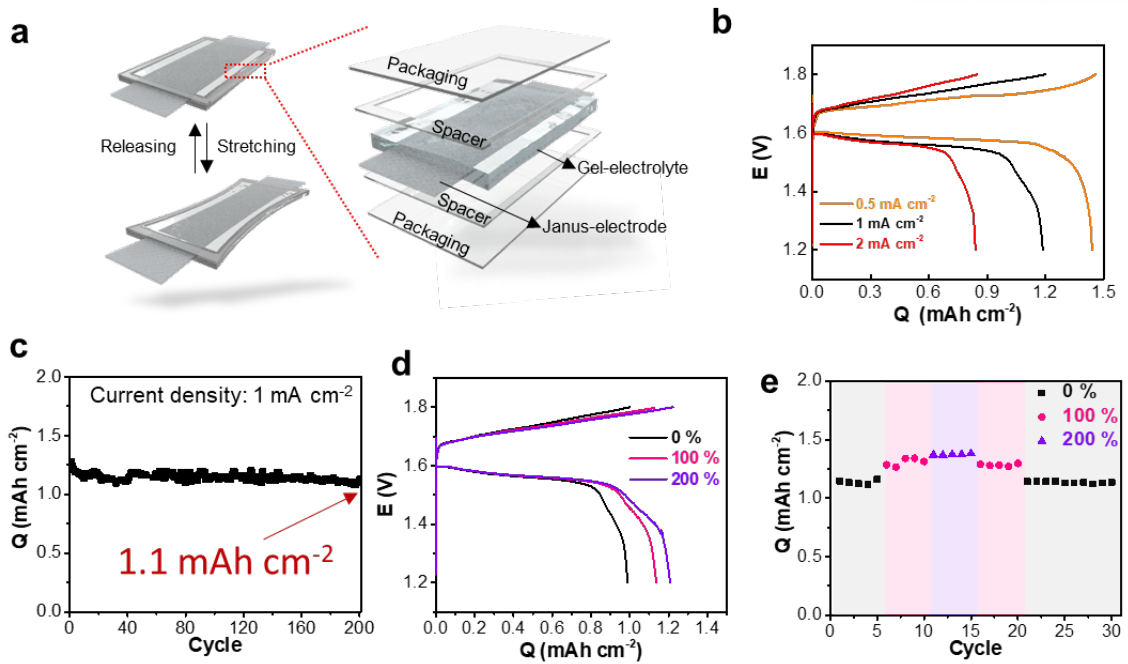


Figure 4-4 | Electrochemical performance of stretchable zinc-silver batteries. a) schematic of configuration of stretchable zinc-silver batteries. b) voltage profile of the full batteries under various current density. c) Cycle performance of the full batteries at a 1 mA h cm^{-2} for 200 cycles. (d) Voltage profiles of the batteries under strain of 0%, 100% and 200% . (e) Cycle performance of the batteries as a function of strain.

4.4 Conclusion

In summary, we demonstrate a Janus-faced electrode to fabricate stretchable silver-zinc rechargeable batteries, which are water-based chemistry, with high energy/power density and natural safety. This electrode shows excellent mechanical durability (strain of 300%) and high electrical properties under strain (0.7 ohm at 200% strain). The electrochemical performance of the batteries demonstrates excellent long-term cyclability and a highly stable capacity even at a strain of 200%. We believe that this innovative stretchable silver-zinc rechargeable batteries can be conformably utilized in diverse wearable electronics.

4.5 Reference

- [1] Y. Sun, J. A. Rogers, *Adv. Mater.* **2007**, *19*, 1897.
- [2] D.-H. Kim, N. Lu, R. Ghaffari, J. A. Rogers, *Npg Asia Mater* **2012**, *4*, e15.
- [3] J. A. Rogers, Y. Huang, *Proc. Natl. Acad. Sci. USA* **2009**, *106*, 10875.
- [4] M. C. LeMieux, Z. Bao, *Nat. Nanotechnol.* **2008**, *3*, 585.
- [5] Y. Hu, X. Sun, *J. Mater. Chem. A* **2014**, *2*, 10712.
- [6] S.-J. Cho, K.-H. Choi, J.-T. Yoo, J.-H. Kim, Y.-H. Lee, S.-J. Chun, S.-B. Park, D.-H. Choi, Q. Wu, S.-Y. Lee, S.-Y. Lee, *Adv. Funct. Mater.* **2015**, *25*, 6029.
- [7] X. Jia, Y. Kan, X. Zhu, G. Ning, Y. Lu, F. Wei, *Nano Energy* **2014**, *10*, 344.
- [8] G. Yu, L. Hu, M. Vosgueritchian, H. Wang, X. Xie, J. R. McDonough, X. Cui, Y. Cui, Z. Bao, *Nano Lett.* **2011**, *11*, 2905.
- [9] C. Yu, C. Masarapu, J. Rong, B. Wei, H. Jiang, *Adv. Mater.* **2009**, *21*, 4793.
- [10] S. Xu, Y. Zhang, J. Cho, J. Lee, X. Huang, L. Jia, J. A. Fan, Y. Su, J. Su, H. Zhang, *Nat. Commun.* **2013**, *4*, 1543.
- [11] W. Liu, Z. Chen, G. Zhou, Y. Sun, H. R. Lee, C. Liu, H. Yao, Z. Bao, Y. Cui, *Adv. Mater.* **2016**, *28*, 3578.
- [12] R. Sengupta, M. Bhattacharya, S. Bandyopadhyay, A. K. Bhowmick, *Prog. Polym. Sci.* **2011**, *36*, 638.
- [13] W. Bauhofer, J. Z. Kovacs, *Compos. Sci. Technol.* **2009**, *69*, 1486.
- [14] Z. Spitalsky, D. Tasis, K. Papagelis, C. Galiotis, *Prog. Polym. Sci.* **2010**, *35*, 357.
- [15] K.-Y. Chun, Y. Oh, J. Rho, J.-H. Ahn, Y.-J. Kim, H. R. Choi, S. Baik, *Nat. Nanotechnol.* **2010**, *5*, 853.
- [16] A. V. Kyrlyuk, M. C. Hermant, T. Schilling, B. Klumperman, C. E. Koning, P. Van der Schoot, *Nat. Nanotechnol.* **2011**, *6*, 364.
- [17] S. Choi, J. Kim, D. Y. Hwang, H. Park, J. Ryu, S. K. Kwak, S. Park, *Nano Lett.* **2016**, *16*, 1179.
- [18] W.-J. Song, S. H. Joo, D. H. Kim, C. Hwang, G. Y. Jung, S. Bae, Y. Son, J. Cho, H.-K. Song, S. K. Kwak, *Nano Energy* **2017**, *32*, 255.
- [19] W. Li, J. R. Dahn, D. S. Wainwright, *Science* **1994**, *264*, 1115.
- [20] H. Kim, J. Hong, K.-Y. Park, H. Kim, S.-W. Kim, K. Kang, *Chem. Rev.* **2014**, *114*, 11788.
- [21] C. Grey, J. Tarascon, *Nat. Mater.* **2017**, *16*, 45.

- [22] C. Grey, J. Tarascon, *Nat. Mater.* **2017**, *16*, 45.
- [23] F. Du, J. E. Fischer, K. I. Winey, *Phys. Rev. B* **2005**, *72*, 121404.
- [24] Y. Sun, J. Lopez, H. W. Lee, N. Liu, G. Zheng, C. L. Wu, J. Sun, W. Liu, J. W. Chung, Z. Bao, *Adv. Mater.* **2016**, *28*, 2455.
- [25] A. Zhang, H. Bai, L. Li, *Chem. Rev.* **2015**, *115*, 9801.
- [26] A. Böker, Y. Lin, K. Chiapperini, R. Horowitz, M. Thompson, V. Carreon, T. Xu, C. Abetz, H. Skaff, A. Dinsmore, *Nat. Mater.* **2004**, *3*, 302.
- [27] E. M. Pérez, N. Martín, *Chem. Soc. Rev.* **2015**, *44*, 6425.

Chapter V. Gradient Assembled Polyurethane-based Stretchable Multilayer Conductors

5.1 Introduction

Stretchable electronics are forefront technologies with the growing demand toward future deformable and wearable devices^[1-3]. The rapidly evolving devices are strongly pushing to develop stretchable conductors as an essential component that possesses high electrical conductivity under significant mechanical strain. Therefore, there have been intensive researches for the development of stretchable conductors based on metal nanomaterials and carbon nanotubes^[4]. However, highly desirable development of suitable stretchable conductors with comparable electrical conductivity during stretching is still required, because the required conductivity is different as degree of stretching in some case where one need to apply^[5,6].

In general, two main approaches have been proposed to make stretchable conductors including geometrical structure-controlled design and ratio-controlled nanocomposite^[7-9]. In the first approach, coating or depositing conductive materials on the surface of an elastomeric substrate have been widely used to achieve stretchable conductors, including buckled, wrinkled, waved, crumpled and island structures. Although these methods afford stable electrical conductivity retention at high strain condition, there are still some limitations that are not only unscalable and complex manufacturing process, but also low volumetric packing density into the practically feasible devices^[10,11].

Alternatively, polymer nanocomposites of in-plane structure possessed conductive pathway owing to conductive fillers homogeneously dispersed in elastomeric polymers^[12,13]. They are considered as the most promising candidate because of their advantages of scalable and high-throughput fabrication process. Such elastic nanocomposites are an entirely full conductor from top to bottom surface, compared to only top-surface conductive structure assembled onto elastomeric substrate^[14-16]. However, the electrical conductivity of the nanocomposite is highly strain-sensitive, which displays the trade-off relationship between stretchability and conductivity in nanocomposites. For example, high content of elastomeric polymer shows superior strains albeit with its low intrinsic conductivity, limiting its practical applications. On the other hand, high loading of the stiff conductive component often demonstrates extremely low strains under 5% because the stress failure of rigid nanocomposites depends on the randomly distributed stress-concentrated hard segments, which can promote propagation of nano- and micro-cracks in

nanocomposites^[17].

Therefore, it has been critical issues to balance this trade-off relationship by revealing a tensile behavior of interdependent components in nanocomposites. Accordingly, a strain-induced self-alignment restructuring property of the conductive filler such as metal nanoparticles was demonstrated within the elastic polymer matrix during deformation owing to the greater matrix mobility of nanoparticles. In addition, it is also important to develop new geometrical design achieving both stretchability and conductivity in the nanocomposites by utilizing such self-reorganization of conductive fillers under strain^[18].

In this regard, in order to develop a universally applicable method for fabricating the geometrically designed nanocomposite conductor, herein we report a gradient assembled polyurethane (GAP)-based stretchable conductor with fine controlled internal architecture assembled with gold nanoparticles (Au NPs) as a conductive filler (**Figure 1**). In present study, we demonstrate a novel assembly protocol, composite-by-composite (CbC) assembly, which integrates the advantages of both conventional vacuum-assisted filtration and layer-by-layer assembly process. Typically, the filtration is advantageous to the rapid and scale-up fabrication of layered thin films and membranes. Conversely, LbL assembly can manufacture the highly ordered architectures, allowing the fine nanoscale control over the thickness and composition of hybrid multi-components through the sequential assembly.

Taken together the advantages of each assembly, the CbC assembled multilayer gradient conductor is constructed by the alternative physical trapping of the electrostatically complexed composite suspensions under vacuum using the positively charged water-dispersible polyurethane and the negatively charged Au NPs in varying ratio. Most uniquely, this GAP stretchable multilayer conductor demonstrates not only top-surface conductive structure with superior mechanical stretchability even above 300% strain in case of high gradient architecture, but also whole through-plane conductor from top to bottom surface of the conductor as increasing the number of interlayers in case of low gradient architecture. Using the GAP stretchable conductor, we demonstrate the highly stretchable energy storage device such as lithium-ion battery retaining stable electrochemical performance under strain. This novel approach for stretchable conductors developed in this study will offer new perceptions in the fabrication of the stretchable conductors for future energy conversion and storage devices as well as advanced wearable electronics.

5.2 Experimental

Materials

30 vol.% cationic polyurethane aqueous dispersion of molecular mass approximately 92,000 (Hepce Chem, Korea). Multiwalled CNT of diameter of 10-15 nm and length of ~200 μm (Hanwha Nanotech Corp, Korea)

Synthesis of Au nanoparticles

Gold(III)chloride trihydrate (360.0 mg) was added to deionized water (500 ml). This gold precursor solution was heated at 95 °C under vigorous stirring for 20 min. Subsequently, 34 mM sodium citrate solution (100 ml) was added to the mixture. The aqueous solution was heated for 20 min followed by cooling to room temperature.

Fabrication of CbC assembled GAP stretchable multilayer electrode

The desired amount of 1.0 vol.% aqueous polyurethane was slowly added to as-prepared Au NPs dispersion of 250 mL under stirring followed by additional stirring for 5 min. The mixture was filtered with vacuum force by using filter papers of 0.8 μm pore size with 47 mm diameter. The resultant film was peeled off from the filter paper after drying the film completely for 1 day at room temperature.

Electrochemical measurements

The electrode was fabricated by spray coating method onto hot plate at 60 °C consisting of active materials (LMO/CNT or PI/CNT), conductive material (super P), and the binder (nafion) in a weight ratio of 8:1:1 onto prepared electrode. The electrodes were cut in the form rectangular shape (20 x 10 mm). The electrochemical properties of half and full cell were measured using a (Biologic science instrument, VSP) with a 1M Li_2SO_4 aqueous electrolyte. The Pt electrode and saturated calomel electrode (SCE) were used as the counter and reference electrode, respectively.

To fabricate stretchable full batteries, we produce an aqueous Li_2SO_4 gel electrolyte. Firstly, 1g of sodium carboxymethylcellulose (CMC) was dissolved in 10 mL deionized water. In order to form a gel, the solution was heated at 75 °C for 2 h under vigorous stirring. And then, the 1M Li_2SO_4 solution was added to the CMC gel at 40 °C for 1 h under stirring. Packaging material (35 x 40 x 10 mm) and a spacer of stretchable full batteries was used as PDMS. The thin spacer (500 μm) accommodated sufficient space to fill the gel electrolyte. The stretchable cathode and anode were attached parallel to the bottom layer using un-cured PDMS solution. And then, a top layer, spacer, and the bottom layer was assembled using O_2 plasma (CUTE, Femto Science, Korea)

treatment. Finally, as-prepared gel electrolyte was prudently injected using syringe.

5.3 Results and discussion

To fabricate polymer nanocomposites-based stretchable conductor, a negatively charged Au NPs suspension stabilized by citrate was initially prepared as a conductive filler. The resulting citrate-stabilized Au NPs had an average diameter of 21.5 ± 5.3 nm (Figure S1). Although one-dimensional (1D) nanomaterials are typically known to be a suitable candidate in a stretchable conductor due to its high aspect ratio, 0D NPs could potentially exhibit greater degree of freedom within the polymer matrix under strain besides their facile and scalable synthetic nature. As an elastomeric component, a highly stable and positively charged water-dispersible polyurethane (PU) suspension was used for fabricating stretchable conductors based on complementary electrostatic interactions with Au NPs.

Initially, we prepared each Au NP-PU nanocomposite suspension (AuPU hereafter with a fraction of Au NPs) via simple mixing of Au NPs and PU suspension in a controlled ratio from 50 to 90 wt% of Au NP through electrostatic complexation (Figure S2). The pure PU film (without Au NPs) displayed a superior stretchability as high as 615%. However, as increasing the content of Au NPs within PU matrix from 50, 85, and 90 wt%, the stretchability of AuPU composite films decreased sharply to 380, 140, and 2%, respectively. In contrast, the resistance was decreased significantly; for example, the 90 wt% AuPU composite film demonstrated the resistance below 1Ω , which was even comparable to the metal conductor (Figure S3). This film also indicated a successful durability over 100 cycles without any changes in resistance, highlighting the preservation of conductive pathway under deformation along with flexible PU backbone (Figure S2). However, one could not achieve high stretchability over 100% using a single polymer nanocomposite film with reasonable electrical conductivity.

Therefore, to augment the weakness of each single-layered AuPU nanocomposite film in either conductivity or stretchability, we suggest a novel geometric design of AuPU film through CbC assembled multilayers of respective single AuPU nanocomposite films to take advantages of both conventional vacuum-assisted filtration and layer-by-layer assembly. In specific, 90 wt% AuPU film was selected as a conductive layer at the outermost sides of both top and bottom, which is spaced by either with 50 wt% or 85 wt% AuPU film as a stretchable layer to afford a high gradient (i.e., combination of 95 and 50 wt% AuPU) or a low gradient (i.e., 95 and 85 wt% AuPU) multilayer structure of distributed Au NPs in whole conductor, respectively. This multilayered structure was referred to as a GAP conductor of 3-layer (3 L). Furthermore, to investigate the effect of the multilayers at a fixed content of Au NPs, the interlayer of multilayer conductor was further segmented evenly with different number of layers by adding additional

conductive layer into stretchable layer, while fixing the contents of the multilayer conductor from 5 L to 9 L with total of three-conductive layers and one-stretchable layer.

The successful fabrication of these GAP multilayer conductors was confirmed by cross-sectional scanning electron microscopy (SEM) (**Figure 2**). The multilayered architectures were clearly observed in the relative contrast between Au NPs and PU in each nanocomposite layer. Furthermore, the corresponding energy dispersive X-ray spectroscopy (EDS) images also revealed the gradient distribution of Au and carbon, respectively, indicating each Au NPs and PU was distributed in the entire conductor with the concentration gradient throughout the conductor. Thermogravimetric analysis (TGA) was performed to classify the specific content of Au NPs of all conductors used in this study (Figure S4). High gradient multilayer conductors from 5 L to 9 L displayed nearly identical Au content of 75 wt. Similarly, the low gradient multilayer conductor showed the Au content of 88 wt% near to the average of 95 and 85 wt% of each AuPU composite suspension. These results clearly suggest the precise control over the number of layers and gradient distribution in internal structure without altering the compositional ratio of each conductive filler and elastic polymer, demonstrating the versatile nature of CbC assembly in building the architecture-controlled nanocomposite conductors.

We then examined the mechanical and electrical characterization of the stretchable GAP conductor (**Figure 3**). The high GAP conductors showed the superior stretchability as above 300%, comparing to that of the low GAP conductors as below 100% strain (Figure 3a). However, the rupture point of both high and low GAP conductors gradually decreased as increasing the number of interlayer, while the obtained Young's modulus increased as shown in Figure 3b and c. It is of note that the Young's modulus of high GAP conductors is lower than that of low gradient, indicating the high ratio of Au NPs to PU of low gradient conductor induced stiff and rigid nanocomposites, resulting in inferior stretchability.

We further investigated the change of internal structure under strain by surface morphology analysis using SEM. The top-surface view images showed 3D interconnected microporous networks of Au NPs-anchored PU chains (Figure S6). Although the porosity was increased with enlarged voids and cracks under strain, the robust PU backbone-induced good recovery was observed with reconstruction of AuPU nanocomposites. The stress failure of GAP multilayer conductors by nano- and micro-cracks in nanocomposites was also confirmed by cross-sectional SEM images of high-gradient multilayer conductor of 9 L under strain (Figure S7). Interestingly, the partially broken interlayer was observed at exactly middle layer among the whole interlayers. These results benefit from maintaining the electrical conductive surface as well as the outstanding recovery because of preventing the rupture of the conductive layer at the outermost sides of both top and bottom without severe cracks. In addition, there was no

delamination of interlayers from the underneath layer due to the high affinity and compatibility of employing the identical components in each nanocomposite layer homogeneously. It should be again highlighted that the highly tunable CbC assembly can fabricate the mechanically powerful stretchable conductor with a simple and scalable solution process.

In order to further verify this rupture point by propagation of cracks starting at the middle layer of GAP multilayer, mechanical simulation in GAP multilayer conductors of 5 L and 9 L was conducted by using program. The higher stress was concentrated on the middle and center layer rather than outer layers, while the stress is more evenly distributed as increasing the number of interlayers.

The electrical conductivity of all GAP multilayer conductors showed a similar change in resistance regardless of the number of interlayers and gradient assembly because the composed top-conductive layer is identical with 90 wt% in AuPU nanocomposite (Figure 3d). However, it is also important to consider the electrical connection of interlayers under strains toward entirely full conductor. We also performed the durability test of electrical conductivity of the GAP multilayer conductors under strain of 20%, 30%, and 40% (Figure 3e). It showed highly stable performance retention even after 1000 cycles. These outstanding mechanical and electrical properties demonstrate the uniqueness of high gradient architecture with in-plane structure to achieve both metallic top-surface conductivity as well as superior mechanical stretchability.

However, the high GAP multilayer conductor still has a limitation, which is only top-surface conductive like a conventional geometrically designed conductor. In contrast, the low GAP multilayer conductor is fully conductive from top to bottom surface with the low vertically directional resistance of $\sim 50 \Omega$ measured in low GAP conductor of 3 L, although its tensile strength is much lower than that of high GAP conductors. Therefore, the vertically directional conductivity in low GAP conductors was theoretically calculated to prove conductive pathway through stretchable layer as a function of the number of interlayers (Figure S9). We considered the contact layer between conductive layer and stretchable layer, resulting in the slightly decreased thickness of stretchable layer (i.e. resistance) with increasing the number of interlayers shown in SEM images (Figure 2), because the number of the mixed contact layers was increased. As a result, the vertical conductivity was increased with increasing the number of interlayers, enabling more facile through-plane electrical conduction from top to bottom surfaces.

Electrical conductivity is strongly related to connectivity between conductive fillers. Specially, to retain stable electrical conductivity of a stretchable conductor, the behavior of conductive filler is important under strain. In this regard, in situ small angle X-ray scattering (SAXS) is a fascinating method to better understand behavior of conductive filler in elastomer matrix (**Figure 4a**). The SAXS analysis of samples was conducted at a constant stretching rate of

80 $\mu\text{m sec}^{-1}$ under strain range of 0 and 100 %. Figure 4b shows 2D SAXS patterns of pure PU and 50 wt% AuPU nanocomposite films at applied uniaxial strains of 0%, 50%, and 100%. In the initial unstrained state, 2D patterns of pure PU and AuPU nanocomposite films exhibited an isotropic scattering geometry, indicating random dispersion of hard segment of PU and Au NPs in the pure PU and AuPU nanocomposite films, respectively. However, the two samples began to develop different scattering patterns upon stretching. The patterns of pure PU evolved from circular to elliptical shape during strain, indicating that the hard segment of PU was aligned along stretching direction (Figure 4b). In contrast, AuPU nanocomposite film showed a butterfly-like pattern upon stretching, resulting from the non-affine relative displacements of the Au NPs in the polymer matrix under strain. As the strain increased, the Au NPs were gradually forming clusters of raft-like structure in the direction perpendicular to the strain axis due to the Poisson contraction, leading to the banded Au NP clusters lying at the stretching direction. These phenomena may lead to a significant alignment and increased interconnection of Au NPs under uniaxial strain, resulting in effective maintenance of its electrical conductivity under strain. Moreover, in order to quantitatively investigate the alignment quality of AuPU nanocomposite films along a stretching direction, we calculated the Hermans orientation factor (f),

$$f = \frac{3(\cos^2 \varphi) - 1}{2}$$

where f is the orientation factor, varying from 0 to 1 for isotropic and perfectly perpendicular to strain direction, respectively and φ is the azimuthal angle. In Figure 4c, the orientation factor, f , indicated that percolation network in the stretching direction began to collapse at a strain of 80%; this result is consistent with the rapidly increasing point of resistance shown in Figure 3d.

To confirm the utilization of the stretchable GAP multilayer conductor as a current collector electrode for practical applications, the electrochemical performance of an aqueous rechargeable lithium-ion battery (ARLB) as a promising power source was examined. The ARLB has superior rate capability by fast transport of Li ions owing to the usage of aqueous electrolytes instead of conventional organic electrolytes, resulting in extremely safe from the risk of explosion. Initially, we synthesized active materials on the surface of carbon nanotubes for the anode and cathode which are polyimides (PI/CNT) and lithium manganese oxide, LiMn_2O_4 (LMO/CNT), respectively (see Figure S10 and S11 in the Supporting Information). To fabricate stretchable electrode, as-prepared cathode and anode materials were deposited onto the GAP multilayer conductors by spray coating method (denoted as GAP cathode and GAP anode, respectively) (see **Figure SX** and **SX** (SEM image of electrode) in the Supporting Information)

The electrochemical performance of the GAP electrode was conducted by cyclic voltammetry (CV) using a three-electrode system in 1 M Li_2SO_4 electrolyte with a Pt electrode and an Ag/AgCl electrode as the counter and the reference electrode, respectively. In **Figure 5a**,

CV curves of the GAP anode and the GAP cathode with increasing scan rate from 2 to 20 mV s⁻¹ showed typical redox peaks of PI and LMO; thus the GAP multilayer conductor clearly indicated the electrochemical stability in the range of working voltage, demonstrating that the GAP multilayer conductor can be used as a current collector for the ARLB system. **Figure 5b** displays voltage profiles of the GAP cathode between 0.0 V and 1.2 V at various C-rates. They delivered specific capacities of 132, 126, 115, and 102 mA h g⁻¹ at 10, 15, 30, and 100 C, respectively. On the other hand, rate performance of the GAP anode at various current rate range from 20 C and 800 C under voltage window of 0 V and -1.0 V was presented in **Figure 4c**. Interestingly, the GAP anode can deliver 95 mA h g⁻¹ even at a high rate of 200 C, corresponding to 78% of the capacity at 20 C. Moreover, both GAP anode and GAP cathode showed outstanding cycling performance at a rate of 100 C after 200 cycles (see **Figure S12** in the Supporting Information)

The electrochemical performance of a full cell was evaluated between the voltage range of 0.0 V and 2.0 V without any strain applied. The full cell was tested in beaker cell containing 1 M Li₂SO₄ with continuous bubbling nitrogen to remove oxygen. The discharge capacities of the full cell were 100 and 77 mA h g⁻¹ at 15 C and 100 C rates, respectively. The long-term cycle performance of the full cell showed outstanding cycle retention of 96 % at a rate of 15 C after 1000 cycles, as shown in **Figure 5d**.

To further demonstrate the electrochemical performance under strain, we designed the stretchable ARLB to establish its practical feasibility for use in deformable electronic devices (**Figure 5e**). The recovery property of the proposed battery could be also introduced by packaging materials of polydimethylsiloxane (PDMS) (**Figure S14** in the Supporting Information). This stretchable ARLB was cycled at a rate of 15 C between 0% and 30% strain (**Figure 5f**). At 30% strain, the stretchable ARLB showed an outstanding capacity retention of 72 % for 10 cycles, compared to un-strained condition. After releasing the strain, the specific capacity of the stretchable ARLB was observed to completely recover to its initial values. **Figure 5g** shows that the proposed stretchable battery could light up red light-emitting diodes (LEDs) during the stretching under 30% strain. These results demonstrated that stretchable full battery-based GAP stretchable conductor is appropriate for a power source to various stretchable electronic devices.

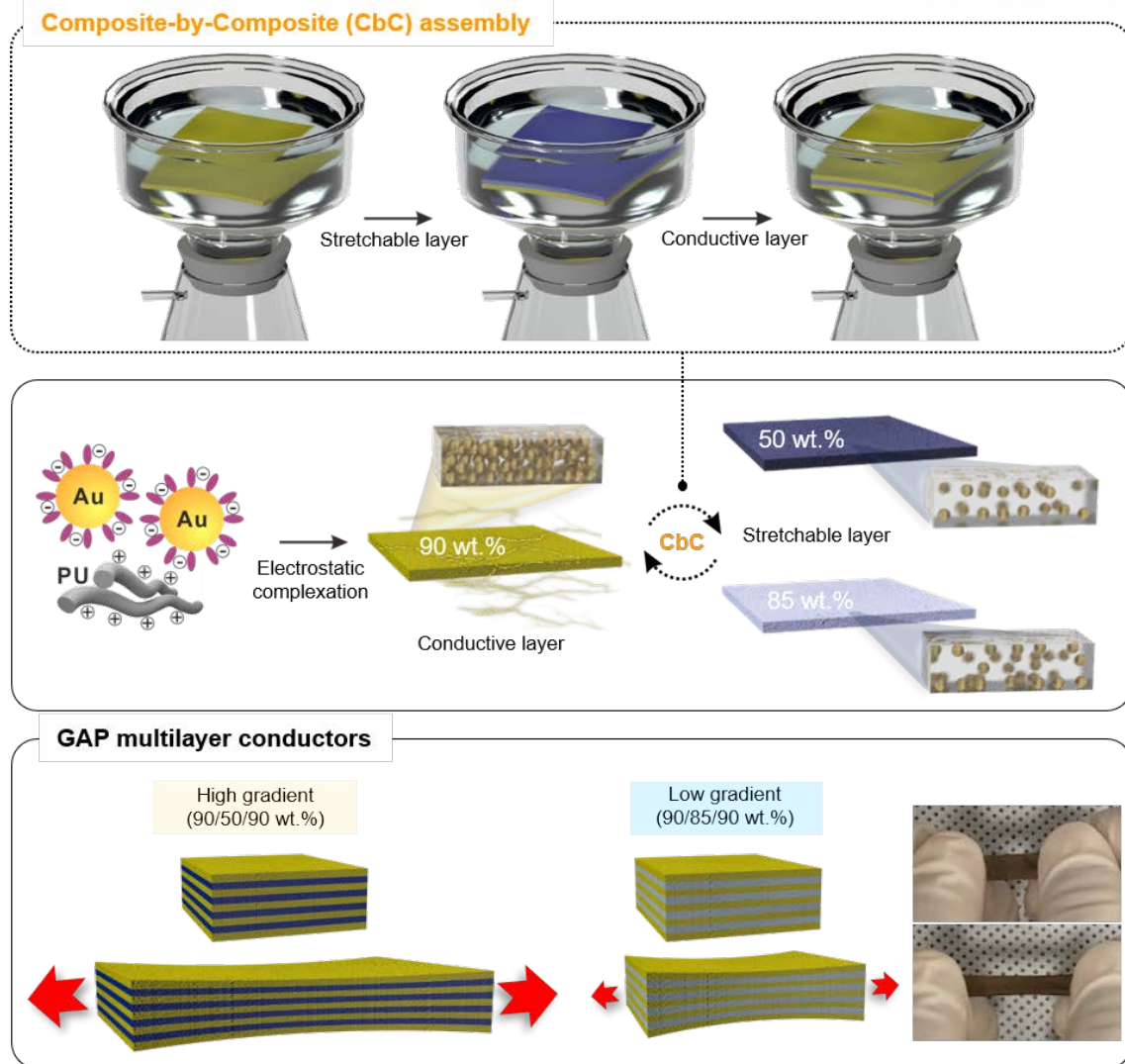


Figure 5-1 | Schematic illustration of GAP multilayer conductors. Composite-by-composite (CbC) assembly of polyurethane (PU)-based stretchable multilayer of high and low gradient conductors with different concentration of Au NPs in stretchable layer. Photograph showing the resulting GAP multilayer conductor under 100% strain.

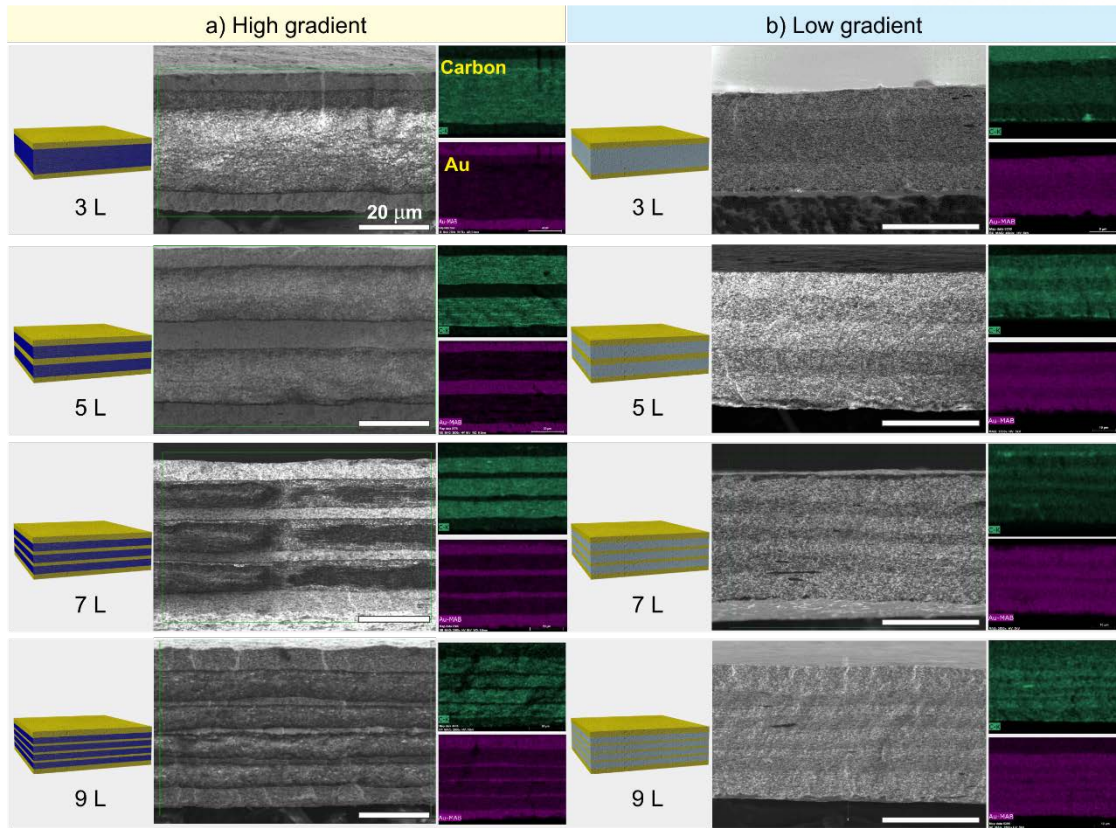


Figure 5-2 | Architecture controlled GAP multilayer conductors. Schematic illustrations and representative cross-sectional SEM images with composed elemental mapping images of carbon and Au of **a**, high and **b**, low gradient multilayer conductors as increasing the number of layers. The scale bar in all SEM images is 20 μm .

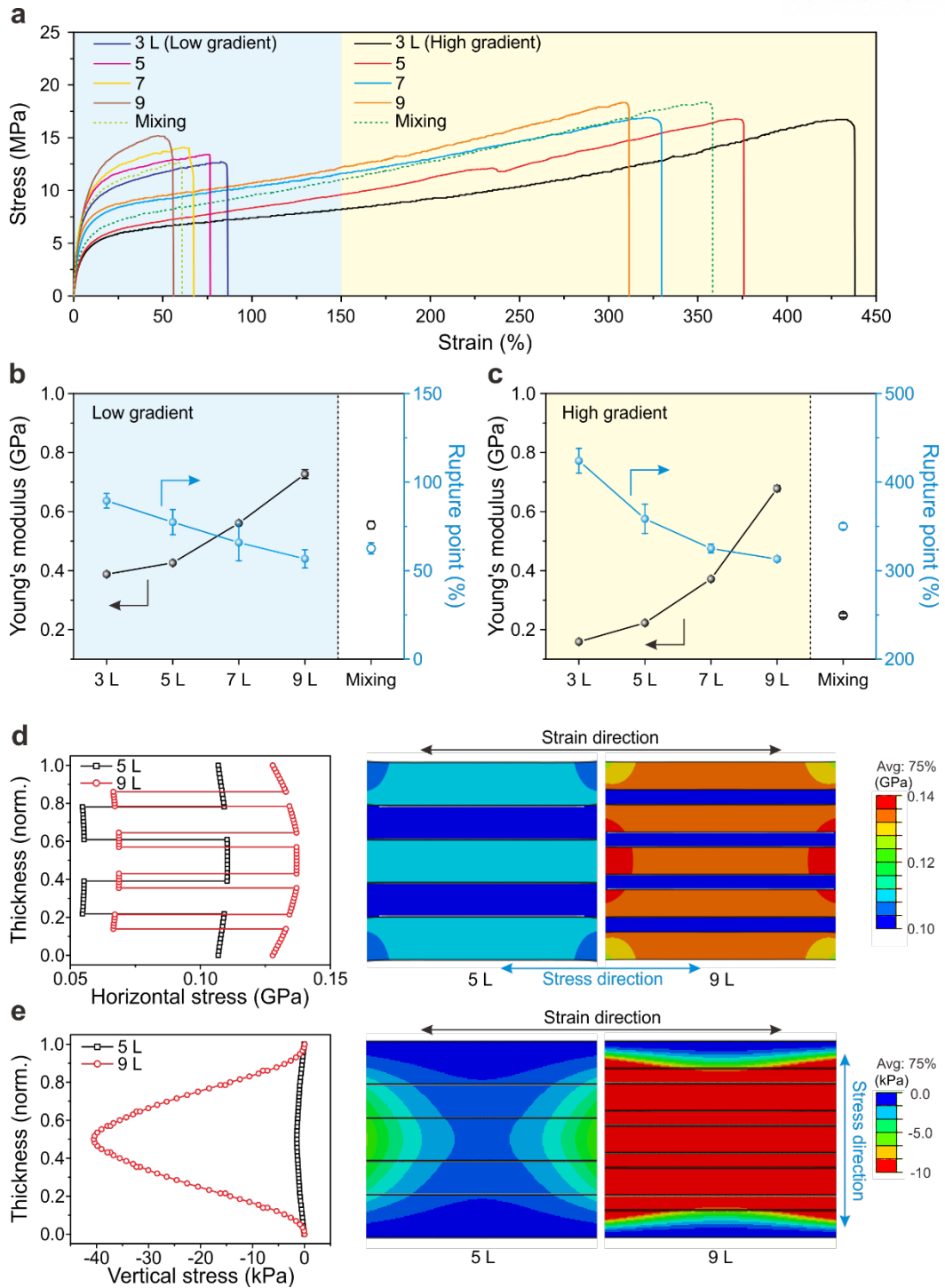


Figure 5-3 | Mechanical and electrical properties of GAP multilayer conductors. a, Stress-strain curves for all GAP multilayer conductors. **b, c**, Young's modulus and rupture point of low and high GAP multilayer conductors. Finite element analysis (FEA) representing von Mises stress distribution in the **d**, horizontal and **e**, vertical direction in 5 L and 9 L low GAP conductors under 50% strain.

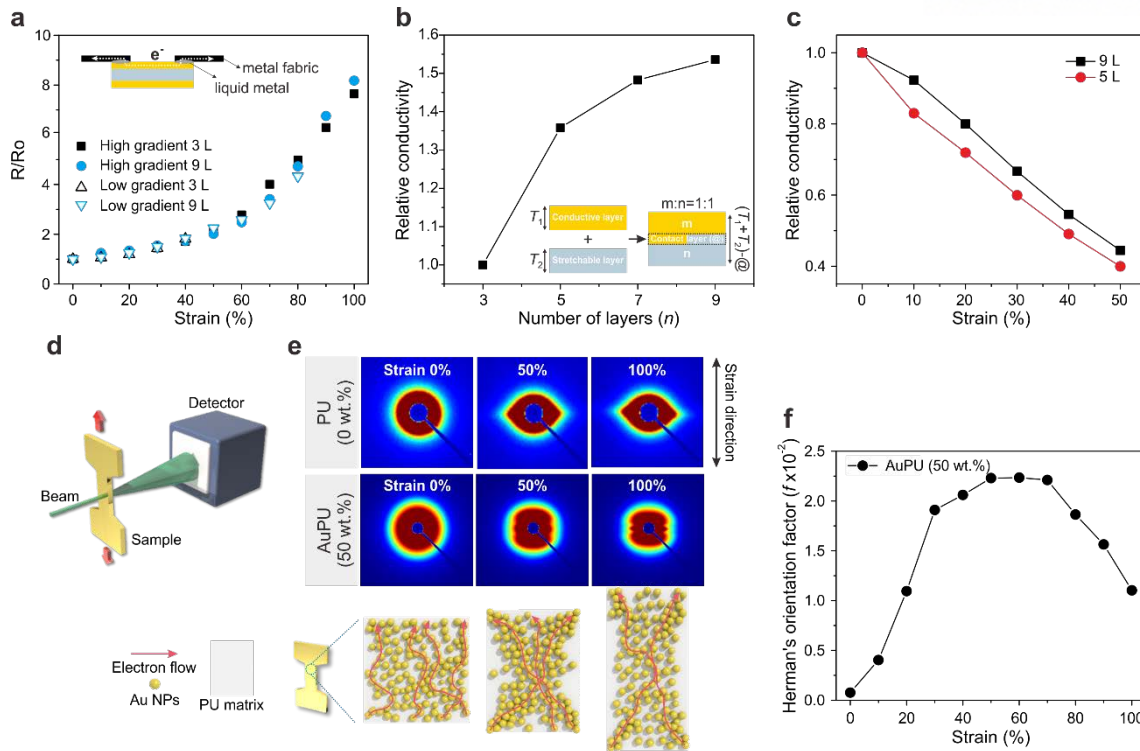


Figure 5-4 | SAXS and simulation analysis for percolation network of Au NPs in PU matrix under strain. **a**, Normalized resistance on the top-surface of high and low GAP multilayer conductors of 3 L and 9 L under different strain conditions. **b**, Calculation of vertical conductivity for low GAP conductors with an increasing number of layers. **c**, Change of vertical conductivity in 5 L and 9 L low GAP conductors under strain. **d**, Schematic illustration of the experimental setup of in-situ SAXS measurement. **e**, 2D SAXS patterns at selected uniaxial strains of 0%, 50%, and 100% for pure PU and 50 wt.% AuPU nanocomposite films, and schematic illustrations summarizing the behavior of Au NPs (yellow spheres) in the matrix and changes in the electrical pathway (red lines) under strain determined by SAXS analysis. **f**, Calculated Hermans orientation factor, f , under strain for a single layer of 50 wt.% AuPU.

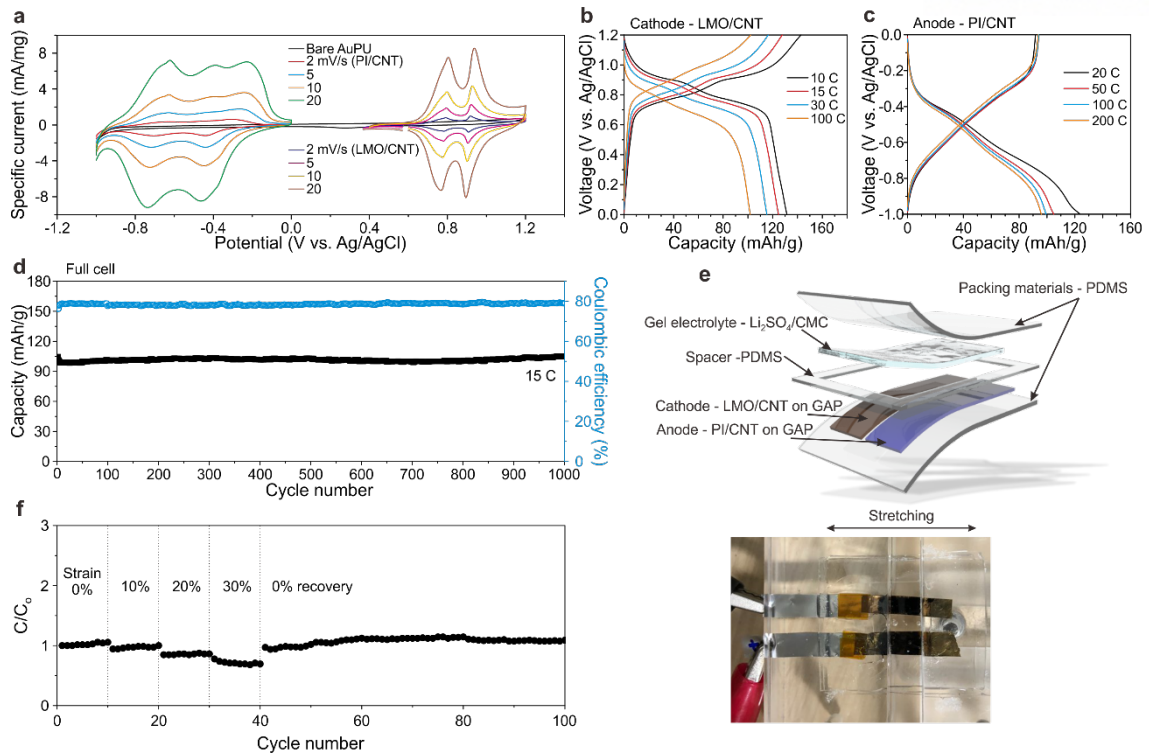


Figure 5-5 | Electrochemical performance of stretchable aqueous rechargeable lithium-ion battery based on GAP multilayer conductor as a current collector. a, Cyclic voltammograms of GAP anode (PI/CNT) and GAP cathode (LMO/CNT) at various C-rates in three electrode systems with 1 M Li_2SO_4 electrolyte. **b,c,** Galvanostatic charge-discharge curves of GAP cathode and GAP anode, respectively. **d,** Cycling performance of full battery at a rate of 15 C between 0.0 and 2.0 V in 1 M Li_2SO_4 for 1000 cycles. **e,** Schematic illustration of the stretchable aqueous rechargeable lithium-ion battery that was fabricated by using the GAP anode and cathode with coplanar layout. **f,** Cycle performance of the stretchable full cell at a rate of 15 C under various strains from 0% to 30% for 100 cycles.

5.4 Conclusion

In summary, we developed internal architecture-controlled GAP stretchable conductors using simple and scalable CbC assembly. This GAP stretchable multilayer conductor offers precise control not only for superior mechanical stretchability by adjusting the gradient concentration of each component, but also for vertically directional conductivity by changing the number of interlayers. As a result, high GAP conductors exhibited in-plane structured stretchable metal conduction over 300% strain, and low GAP conductors exhibited excellent electrical conductivity in the vertical direction as well as parallel to the surface over 50% strain. An in-depth study on the percolation network of Au NPs within the PU matrix was further performed by in-situ SAXS analysis and mechanical simulation to understand the stress-distribution behavior by crack propagation in multilayer architecture. We also demonstrated a stretchable aqueous rechargeable lithium-ion battery, which delivered stable power with high rate capability under strain due to using GAP conductors. This novel approach for developing stretchable conductors is expected to encourage the design of stretchable conductors with both high mechanical and electrical performance. These will have important applications for future energy conversion and storage devices as well as advanced flexible and wearable electronics.

5.5 Reference

- [1] J. A. Rogers, Y. Huang, *Proc. Natl. Acad. Sci. USA* **2009**, *106*, 10875.
- [2] M. C. LeMieux, Z. Bao, *Nat. Nanotechnol.* **2008**, *3*, 585.
- [3] S. Hong, S. Myung, *Nat. Nanotechnol.* **2007**, *2*, 207.
- [4] H. Jinno, K. Kuribara, M. Kaltenbrunner, N. Matsuhisa, T. Someya, T. Yokota, T. Sekitani, *Nat. Commun.* **2015**, *6*, 7461.
- [5] A. Manekkathodi, M. Y. Lu, C. W. Wang, L. J. Chen, *Adv. Mater.* **2010**, *22*, 4059.
- [6] T. Sekitani, T. Someya, *Adv. Mater.* **2010**, *22*, 2228.
- [7] J. A. Rogers, T. Someya, Y. G. Huang, *Science* **2010**, *327*, 1603.
- [8] M. Ramuz, B. C. K. Tee, J. B. H. Tok, Z. Bao, *Adv. Mater.* **2012**, *24*, 3223.
- [9] D. J. Lipomi, B. C. K. Tee, M. Vosgueritchian, Z. Bao, *Adv. Mater.* **2011**, *23*, 1771.
- [10] M. Amjadi, K. U. Kyung, I. Park, M. Sitti, *Adv. Funct. Mater.* **2016**, *26*, 1678.
- [11] W. Liu, M. S. Song, B. Kong, Y. Cui, *Adv. Mater.* **2017**, *29*, 1603436
- [12] H. Li, Y. Ding, H. Ha, Y. Shi, L. Peng, X. Zhang, C. J. Ellison, G. Yu, *Adv. Mater.* **2017**, *29*, 23.
- [13] W. J. Song, J. Park, D. H. Kim, S. Bae, M. J. Kwak, M. Shin, S. Kim, S. Choi, J. H. Jang, T. J. Shin, S.Y Kim, K. Seo, S. Park, *Adv. Energy Mater.* **2018**, *8*, 1702478
- [14] D. H. Kim, J. A. Rogers, *Adv. Mater.* **2008**, *20*, 4887.
- [15] C. Wang, W. Zheng, Z. Yue, C. O. Too, G. G. Wallace, *Adv. Mater.* **2011**, *23*, 3580.
- [16] Y. Zhang, Y. Huang, J. A. Rogers, *Curr. Opin. Solid State Mater. Sci.* **2015**, *19*, 190.
- [17] K. Xie, B. Wei, *Adv. Mater.* **2014**, *26*, 3592.
- [18] C. Yan, X. Wang, M. Cui, J. Wang, W. Kang, C. Y. Foo, P. S. Lee, *Adv. Energy Mater.* **2014**, *4*, 5
- [19] R. Kumar, J. Shin, L. Yin, J. M. You, Y. S. Meng, J. Wang, *Adv. Energy Mater.* **2017**, *7*.
- [20] W. J. Song, J. Park, D. H. Kim, S. Bae, M. J. Kwak, M. Shin, S. Kim, S. Choi, J. H. Jang, T. J. Shin, S.Y Kim, K. Seo, S. Park, *Adv. Energy Mater.* **2018**, *8*, 1702478
- [21] H. Li, Y. Ding, H. Ha, Y. Shi, L. Peng, X. Zhang, C. J. Ellison, G. Yu, *Adv. Mater.* **2017**, *29*, 23.
- [22] Y. Sun, J. Lopez, H. W. Lee, N. Liu, G. Zheng, C. L. Wu, J. Sun, W. Liu, J. W. Chung, Z. Bao, *Adv. Mater.* **2016**, *28*, 2455.
- [23] Y. Ma, X. Feng, J. A. Rogers, Y. Huang, Y. Zhang, *Lab on a Chip* **2017**, *17*, 1689.
- [24] X. Ning, X. Wang, Y. Zhang, X. Yu, D. Choi, N. Zheng, D. S. Kim, Y. Huang, Y. Zhang, J. A. Rogers, *Adv. Mater. Interfaces* **2018**, 1800284.

- [25] D. H. Kim, J. A. Rogers, *Adv. Mater.* **2008**, 20, 4887.
- [26] K. Abraham, *Electrochim. Acta* **1993**, 38, 1233.

Acknowledgement

2013년 1월 6일, 대학원에 대한 기대감과 두려움을 안고 유니스트에 왔습니다. 5년 반이라는 길다면 길고 짧다면 짧은 시간동안 학위를 받을 수 있던 것은 저 혼자만의 힘이 아니라 수많은 사람의 호의와 함께 엮기 때문이라고 생각합니다. 먼저 망양지탄 속에서도 언제나 정도를 향해 올바르게 이끌어 주신 박수진 지도교수님께 깊은 감사의 말씀을 전하고 싶습니다. 무량하신 교수님의 은혜를 언제나 기억하고 낮은 자세로 진리를 탐구하며 세상을 이롭게 하는 연구자가 되도록 노력하겠습니다.

또한, 귀한 시간을 내주셔서 제 논문을 심사해주신 유니스트 에너지 공학과 이상영 교수님 감사 드립니다. 그리고, 송현곤 교수님, 서관용 교수님께도 진심으로 감사합니다. 바쁜 시간 와중에도 디펜스 끝나고 저녁에 같이 식사를 할 수 있어서 영광이었습니다. 그리고 두 분다 축의금 주신다고 하신 말씀 깊이 새기도록 하겠습니다. 꼭 연락 드리도록 하겠습니다. 특히, 저희 논문 심사를 흔쾌하게 허락해주고, 먼 걸음 해 주신 정운룡 교수님께서서는 다시 한번 깊은 감사의 말씀을 전하고 싶습니다. 앞으로 심사위원님께 누가 되지 않도록 낮은 자세로 진리를 탐구하는 자세로 세상을 이롭게 하는 연구자가 되도록 하겠습니다.

긴 공부를 지지하고 응원 해주시고 항상 자랑스럽게 저를 생각해주신 하늘에 계신 아버지가 굉장히 보고 싶습니다. 그리고 저를 믿고 기다려주신 어머니에게도 정말 감사드립니다. 앞으로 받은 은혜 잊지 않고 효도하며 살아가도록 하겠습니다. 저를 키워주신 할아버지 할머니에게도 정말 감사 드립니다. 자주 연락 드리도록 하겠습니다.

5년이 넘는 기간동안 같이 생활했던 우리 연구실 (Spark Lab) 인원들에게 감사에 말씀 전합니다. 동갑이었지만 랩실 선배였던 최신호 박사, 연구에 대한 많은 조언 정말 고맙고 결혼 할 때 꼭 연락해줘. 그리고 연구와 더불어 인생에 대해 많은 가르침을 주신 승민이형 (교수님), 바쁜 와중에서도 시간을 내주셔서 저의 고민을 들어주시고 용기를 주셔서 감사 합니다. 형과 제대로 된 연구를 못한 것이 정말 많아 아쉽습니다. 그럼 정말 멋진 일을 할 수 있었을 텐데요. 귀찮으시겠지만 앞으로도 제가 자주 연락 드리도록 하겠습니다. 입학 동기인 태수, 명수, 지은아, 짧게는 2년 길게는 5년을 같이 생활 할 수 있어서 정말 행복했어. 태수는 같이 게임이랑 운동도 같이 많이 했는데, 다만 연구 분야가 겹치지 않아서 같이 일을 못해서 많이 아쉽다. 너랑 일했으면 많이 배울 수 있었을 텐데. 시간내서 내 디펜스에 참석해줘서 고맙고 앞으로도 계속 연락하면서 지내도록 하자. 명수야, 앞으로 남은 시간 열심히 준비해서 멋진 박사님으로 졸업했으면 좋겠다. 나보다 결혼을 먼저 할 줄을 정말 꿈에도 몰랐다. 좋은 여자친구를 만났으니, 좋은 일만 있을 거야! 항상 힘내고, 의기소침 하지 않았으면 좋겠다. 지은아! 결혼하면 꼭 연락해라! 나랑 같이 생활하면서 고생했을 우리 랩실 후배들에게도 고맙습니다. 재건아 2년 동안 랩장 하면서 고생 많았다. 이름이 나랑 비슷한 규진아, 정말 후배로서 같이 생활 (게임, 축구, 술)을 하면서 즐거운 시간 많이 보낸 것 같다. 좋은 결과들이 많이 나와서 너무 축하한다. 마음 고생했던 것에 대한 보상을 받는 거라고 생각 한다. 앞으로도 좋은 결과들 많이 내고, 같이 하는 연구도 좋은 결실을 맺어 보자. 동기야, 앞으로 마무리 잘하도록 하고 졸업을 잘 했으면 좋겠다. 첫 부사수 소연아, 나한테 혼도 많이 나고 내가 자주 놀려서 힘들었을 텐데 잘 견디고 항상 웃어줘서 고맙다.

너가 꼭 결혼을 할 수 있었으면 좋겠다. 꼭 연락해라! 우영아, 남은 기간 잘 준비해서 좋은 곳에 취업 했으면 좋겠다. 그리고 김성호, 최성호도 남은 기간 열심히 하고 랩의 미래를 쥐고 있는 만큼 교수님의 기대에 부응하도록 열심히 했으면 좋겠다. 인천 논현동 석근아, 항상 열심히 하는 너에 모습을 보며 나 역시도 더 열심히 해야겠다는 생각이 가끔 들었다. 개인적인 생각에는 너가 박사를 하면 성공 할 것 같다. 너 자신을 믿고 지금 같이 한다면 꼭 그렇게 될 거다. 마지막으로, 머리가 똑똑한 코나 차주 상엽아, 부탁하는 일들 잘해줘서 정말 고맙다. 나에게는 정말 중요한 시기인데 너가 도와줘서 좋은 결과들이 나올 것 같다. 똑똑한 머리를 잘 써서, 좋은 연구자가 되었으면 한다. 졸업을 하고 나서도 계속 연락하면서 지내도록 하자.

같이 일을 했던 황치현 박사, 김동협, 박정환에게 고맙다는 말을 전합니다. 부족한 저를 믿고 따라줘서 고맙고 앞으로도 좋은 연구를 같이 했으면 좋겠습니다. 특히 치현아, 너가 술을 못 마셔서 아쉬웠지만 연구에 대해서 많이 배웠다. 같이 축구도 많이 정말 좋았다. 이제 몸 관리 잘해서 꼭 원하는 결과를 얻었으면 좋겠다! 고마워. 그리고 조성환, 송준혁에게도 감사 합니다. 내가 포항 가서 한잔 사도록 할께. 이제 형 동생으로 지내도록 하자!

유니스트에서 지내면서 또 하나의 기쁨 이었던 경로당 축구 동아리 친구들에게 정말 감사 합니다. 특히, 축구도 잘하고 같이 술도 많이 마셨던 민수, 치주, 승진, 용훈, 대우에게 고맙다는 말을 전하고 싶고, 앞으로도 각자의 길을 가겠지만 꼭 연락을 하고 지냈으면 좋겠다. 많은 추억을 만들어줘서 고맙다.

마지막으로 부족한 내 옆에서 묵묵히 응원해준 여자친구 손혜빈에게 이 모든 영광을 돌리고 싶습니다. 속상한 일이 생겼을 때 내 이야기를 공감하며 들어주고, 논문이 되거나 상 받았을 때 자기 일 처럼 기뻐해줘서 고마워. 그런 것 들이 내가 열심히 할 수 있는 동기 부여가 되었던 것 같아. 앞으로 더욱더 최선을 다해서 원하는 것을 꼭 이룰께. 회사 휴가까지 써서 내 디펜스와 어색한 회식자리에 참석해줘서 정말 고마워. 앞으로 힘들 때나 어려운 시기에도 서로를 믿고 의지해서 잘 헤쳐 나가자.